Alma Mater Studiorum – Università di Bologna

DOTTORATO DI RICERCA IN

NANOSCIENZE PER LA MEDICINA E PER L'AMBIENTE

Ciclo 35

Settore Concorsuale: 03/B1 - FONDAMENTI DELLE SCIENZE CHIMICHE E SISTEMI INORGANICI

Settore Scientifico Disciplinare: CHIM/03 - CHIMICA GENERALE E INORGANICA

FUNCTIONAL ENGINEERING OF HYBRID HETEROSTRUCTURES FOR APPLICATION IN ELECTRONIC, OPTICAL AND OPTOELECTRONIC NANOSTRUCTURED DEVICES

Presentata da: Salvatore Moschetto

Coordinatore Dottorato

Prof. Dario Braga

Supervisore

Dr. Stefano Toffanin

Co-supervisori

Dr. Mario Prosa

Prof. Matteo Calvaresi

Esame finale anno 2023

Abstract

Interfacing materials with different intrinsic chemical-physical characteristics allows for the generation of a new system with multifunctional features. Here, this original concept is implemented for tailoring the functional properties of bi-dimensional black phosphorus (2D bP or phosphorene) and organic light-emitting transistors (OLETs).

Phosphorene is highly reactive under atmospheric conditions and its small-area/lab-scale deposition techniques have hampered the introduction of this material in real-world applications so far. The protection of 2D bP against the oxygen by means of functionalization with alkane molecules and pyrene derivatives, showed long-term stability with respect to the bare 2D bP by avoiding remarkable oxidation up to 6 months, paving the way towards ultra-sensitive oxygen chemo-sensors. A new approach of deposition-precipitation heterogeneous reaction was developed to decorate 2D bP with Au nanoparticles (NP)s, obtaining a "stabilizer-free" that may broaden the possible applications of the 2D bP/Au NPs interface in catalysis and biodiagnostics. Finally, 2D bP was deposited by electrospray technique, obtaining oxidized-phosphorous flakes as wide as hundreds of μm2 and providing for the first time a phosphorous-based bidimensional system responsive to electromechanical stimuli.

The second part of the thesis focuses on the study of organic heterostructures in ambipolar OLET devices, intriguing optoelectronic devices that couple the micro-scaled light-emission with electrical switching. Initially, an ambipolar single-layer OLET based on a multifunctional organic semiconductor, is presented. The bias-depending light-emission shifted within the transistor channel, as expected in well-balanced ambipolar OLETs. However, the emitted optical power of the single layer-based device was unsatisfactory. To improve optoelectronic performance of the device, a multilayer organic architecture based on hole-transporting semiconductor, emissive donor-acceptor blend and electron-transporting semiconductor was optimized. We showed that the introduction of a suitable electron-injecting layer at the interface between the electron-transporting and light-emission layers may enable a $\approx 2\times$ improvement of efficiency at reduced applied bias.

Table of Contents

List of Abbreviations

$[(CH_3)_2S]AuCl$	Chloro(dimethylsulfide)gold(I)
2D	Bidimensional materials
2D bP	Bidimensional black phosphorus
2D PO_x	Phosphorene oxides
4CzIPN	2,4,5,6-tetra(9H-carbazol-9-yl) isophthalonitrile
AFM	Atomic force microscopy
Alq_3	Tris(8-hydroxyquinoline)aluminum
AO	Atomic orbital theory
bphen	Bathophenanthroline
C24	Tetracosane
C8-BTBT	2,7-dioctyl[1]benzothieno[3,2-b][1] benzothiophene
CMOS	Complementary metal-oxide semiconductor
COF	Covalent−organic framework
DFH-4T	α,ω-diperfluorohexyl-quaterthiophene
DFT	Density functional theory calculations
DH4T	a,o-dihexyl-quaterthiophene
DHCO4T	dicarbonyl ended quaterthiophene
DMF	N,N-dimethylformamide
DMSO	Dimethyl sulfoxide
DPP	Diketopyrrolopyrrole
DPP-DTT	Poly[2,5-(2-octyldodecyl)-3,6-diketopyrrolopyrrole-alt-5,5-(2,5-di(thien-2-yl)thieno[3,2-b]thiophene)]
EDX	Energy-dispersive X-ray analysis
EFM	Electrostatic force microscopy
EIL	Electron-injection layer
EML	Emission layer
EQE	External quantum efficiency
ES	Electrospray tool
F8BT	Poly(9,9-di-n-octylfluorene-alt-benzothiadiazole)
FET	Field-effect transistors
FFT	Fast Fourier transform
FWHM	Full width at half-maximum
h-BN	Hexagonal boron nitrite
HMDS	Hexamethyldisilazane
HOMO	Highest occupied molecular orbital
HR-AFM	High resolution atomic force microscopy

HREM	High-resolution electron microscopy
Ir(MDQ)$_2$(acac)	Bis(2-methyldibenzo[f,h]quinoxaline)(acetylacetonate) iridium(III)
Ir(ppy)$_3$	Tris(2-phenylpyridine)iridium(III)
ISC	Intersystem crossing process
ITO	Indium Tin Oxide
LDHs	Layered double hydroxides
LSPR	Localized surface plasmonic resonance
LUMO	Lowest unoccupied molecular orbital
MD	Molecular dynamic calculations
MEH-PPV	Poly[2-methoxy-5-(2′-ethyhexyloxy-1,4- phenylene-vinylene)]
MIS	Metal-insulator-semiconductor devices
MO	Molecular orbital theory
MOF	Metal−organic framework
MOSFET	Metal-oxide-semiconductor field-effect transistor
NDI	Naphthalene diimide
N-F2-6	2,5-bis(4-(perfluorooctyl)phenyl)thieno-[3,2-b]thiophene
NIR	Near infrared
NMP	N-Methyl-2-pyrrolidone
n-OSC	N-type semiconductor
NPs	Nanoparticles
NT4N	2,20-([2,20-bithiophene]-5,50-diyl)bis(5-octyl-4-phenyl-4H-thieno[2,3-c]pyrrol-6(5H)-one
OFET	Organic field-effect transistor
OLED	Organic Light Emitting Diode
OLET	Organic Light Emitting Transistor
OSC	Organic semiconductor
P13	Ditridecylperylene-3,4,9,10-tetracarboxylic diimide
PBA	Pyrenboronic acid
PBE	Pyrenboronic ester
PBTTT-C14	Poly(thiophene-thienothiophene)
PCAN	9-(9-phenylcarba- zole-3-yl)-10-(naphthalene-1-yl)anthracene
PFM	Piezoresponse force microscopy
PFO	Poly[9,9-di(ethylhexyl) fluorene]
PMMA	Poly(methyl methacrylate)
PO$_x$	Oxidized phosphorus
Pt(tpbp)	Pt(II)–tetraphenyltetra-benzoporphyrin
Py	Pyrene
RISC	Reverse intersystem crossing
SAM	Self-assembled monolayer
SEM	Scanning electron microscopy

ss-NMR	Multinuclear solid-state NMR
SY	Super yellow
TADF	Thermally activated delayed fluorescence
TCSPC	Time-correlated single-photon counting
TEM	Transmission electron microscopy
THF	Tetrahydrofuran
TI	2,3-thieno-imide ended oligothiophenes
TMD	Transition metal dichalcogenide
vdW	Van der Waals
WF_m	Metal work function
XPS	X-ray photoelectron spectroscopy

Chapter 1

Introduction

The functional and structural properties of a material are related to its own intrinsic physical and chemical characteristics. The knowledge of these features allows us to choose the more suitable material depending on the specific application.
In most cases, in view of increasingly sophisticated applications or highly performing devices, the intrinsic properties of the materials need to be enhanced or coupled with new functionalities. By combining heterogeneous regions, namely region with different chemical and physical properties in the material, it is possible to improve or add new functionalities, resulting in ad-hoc material for the selected application.
The materials thus created, where the interactive coupling between heterogeneous regions produces different integrated properties, takes the name of heterostructured materials or, more simply, heterostructures.[1]
Even in nature, heterostructures are present in numerous botanical and biological systems,[2,3] as a result of millions of years of natural evolution.
The molluscs shells are an example of natural heterostructure. In particular, the abalone shells are composed of an outer layer of Ca_2CO_3 (calcite) which is hard but brittle. The outer layer is supported by the inner layer of tough nacre, in order to maintain integrity in case of external impact.[4]
Another example of natural heterostructure is the stems of bamboo, where the strong fibrils embedded in a softer matrix make it so strong, lightweight and tough that is still used for scaffolding in the construction and renovation of buildings in Hong Kong.[5]
Over the mechanical context, in nature exist also heterostructures with very interesting optical features.
Lengenbachite is a layered material composed of alternated stacks of PbS-like and M_2S_3-like layers whose highly anisotropic optical response suggests its use for photonic integrated circuits and optical information processing.[6] Franckeite, is another natural heterostructure, a complex layered crystal composed of sulfur, iron, lead, tin and

antimony. In this material, a wide-band and fast photoresponse has been observed highlighting the possible use in optoelectronic devices.

In general, depending on the constituent materials, it is possible to distinguish different kinds of heterostructures.

Van der Waals (vdW) systems are surely the most well-known heterostructures after the discovery of graphene in 2004,[7] resulted in the Nobel Prize in Physics 2010. In fact, bidimensional materials (2D) offer the ideal platform that allows the formation of this kind of layered heterostructures. Held together by van der Waals forces, the bidimensional crystals with atomic thickness form one vertical stack with properties often different from the 3D counterpart. Due to electron confinement in two dimensions,[8] graphene and the 2D materials class in general, show unprecedented chemical, physical, and electronic features as excellent electrical[7] and thermal[9] conductivity, ultrahigh carrier mobility[7] at room temperature, ultrahigh specific surface area,[10] excellent optical transparency[11] and other interesting properties.

The discovery of graphene has opened the way to the exploration of other materials with similar properties. Since then, the library of graphene-like materials is exponentially increased, shielding in light new 2D nanomaterials such as graphitic carbon nitride (g-C3N4),[12–14] hexagonal boron nitrite (h-BN),[15–17] transition metal dichalcogenides (TMDs),[18–21] layered metal oxides,[22] layered double hydroxides (LDHs),[23] MXenes,[24] covalent−organic frameworks (COFs),[25] metal−organic frameworks (MOFs),[26–28] noble metals,[29–32] polymers,[33–36] perovskites,[37,38] and organic−inorganic hybrid perovskites.[39,40]

Over the before-mentioned classes of materials, a 2D mono-elemental class of materials, Xenes, i.e., silicene, boronene, phosphorene[41] has come to the stage.

Among Xenes, phosphorene (2D black phosphorus, 2D bP) has been issued for the several unexpected properties in microelectronics, environmental monitoring, energy and healthcare. In addition, the biocompatibility of 2D bP makes it a promising material for biomedical applications.[42]

Because of all the above-described excellent properties, the first part of this thesis work is focused on the realization of heterostructures based on 2D bP in order to realize and characterize new systems with multiple functional and structural properties that can be straightforwardly exploited in real-setting applications.

Inorganic heterostructures have been essential in the huge development of the electronic and communications fields. The SiGe heterostructure at present dominates the silicon heterostructure world, since it is at the basis of the well-known MOSFET (metal-oxide-semiconductor field-effect transistor) and CMOS (complementary metal-oxide semiconductor) devices.[43] Since the first experimental transistor in 1947, the MOSFET is the dominant solid-state device[44] thanks to its higher performance and lower cost. Also, high-performing optoelectronic devices based on SiGe heterostructures have been reported. In particular, SiGe/Si heterodiodes were realized as photodetectors with fast response, low noise currents, and high responsivity,[45–48] reaching approximately 1 A/W at 1.3 micrometer wavelength and 0.1 A/W at 1.55 micrometer wavelength for a 240-micrometer long device.[49]

During the last 40 years, the scaling of the vertical and horizontal transistor dimensions has led to remarkable and nearly unprecedented progress. In 2019, two of the largest foundries in the world, Samsung and TSMC, announced their 5 nm manufacturing process,[50] getting closer to the end of the Moore law.[51] A large part of the success of the inorganic heterostructures is due to the possibility of dimension scaling, however another intrinsic structural characteristic of inorganic heterostructure such as *epitaxy* has played a fundamental role in the assessment of the application-driven versatility of inorganic materials.

The word epitaxy derives from the Greek prefix *epi* (upon) and *taxis* (arrangement) and indicates the process of growing a crystal of a particular orientation on top of another crystal, where the orientation is determined by the underlying crystal.[52] More specifically, if the growing layers are made up of the same material as the substrate the process is called *homoepitaxy*, otherwise it is called *heteroepitaxy*. Hence, the achievement of high-performance device based on Si heterostructures is due to *epitaxy* process, which permits to obtain crystalline thin film with selected orientations.[43]

Not only inorganic materials can be implemented for realizing heterostructures, but also the organic counterparts. Indeed, stacks of layers of multifunctional organic semiconducting materials are present in the electronic appliances market since their implementation in flexible, wearable, and cost-effective devices.[53–55]

Thanks to the massive use in optoelectronic devices such as smartphones, televisions, and in general in displays, one of the most popular optoelectronic device based on organic heterostructures is surely Organic Light Emitting Diode (OLED).[56,57] This class of devices is characterized by a multi-layered stack of organic materials with specific

functionalities which may mime the general architecture of inorganic heterostructures. The average thickness of an OLED organic stack is ≈ 250 nm.[58] This dimensional parameter is quite different if compared with that of the vdW or with the inorganic SiGe-based heterostructures, where the average thickness is on the order of the tens of nanometers.[59,60] The higher thickness of the organic heterostructures corresponds to the presence of non-epitaxially ordered amorphous layers within the stack.

In this context, we performed a systematic experimental activity on the development of organic heterostructures as reported in the second part of the thesis which aims to be the active region in optoelectronic devices. The device platform used for testing and optimizing the as-developed organic multilayer stacks is the Organic Light Emitting Transistor (OLET) which is a real multifunctional device where the combines the OLED's light emission characteristic typical of OLED is coupled with the electrical switching functionality of the field-effect transistors (FETs). In particular, the fabrication process, the optimization of the optoelectronic performance, and a thorough study of the basic work principles of this innovative device platform have been reported.

Here below, a short synopsis of the thesis is reported:

Chapter 2 introduces hybrid heterostructures based on a bi-dimensional semiconductor, the 2D black phosphorus. The general properties of 2D bP, including the major drawbacks related to the high chemical reactivity with oxygen and the issue with the scalability of the fabrication process, are discussed. Several hybrid heterostructure approaches are described in order to passivate the 2D bP and add new properties for real-setting applications.

Chapter 3 introduces fully-organic heterostructures for light-emitting device realization. An innovative device platform is used to optimize the performance of the optoelectronic properties of the as-realized organic stack, i.e. OLET device. Firstly, single-layer ambipolar light-emitting transistors are realized by using a thiophene-derived semiconductor, capable to transport both holes and electrons, and emitting light. Then, multilayer ambipolar light-emitting transistors are realized and optimized to increase optical performance of the devices.

In Chapter 4 the overall major relevant results about the realization of new hybrid 2D and fully organic heterostructures are resumed and, in addition, highlights on the possible applications in real setting and future development of the technology based on heterostructures are reported.

Chapter 5 reports the experimental setups used in the PhD internship. In particular, the deposition techniques such as spin-coating, used for some in liquid depositions in 2D bP-based heterostructures, and thermal sublimation, used for all the OLET devices realization are described. Moreover, surface and optical characterization techniques (scanning probe microscope techniques) are described. Finally, optoelectronic characterization techniques used to determine the figures of merit of OLET devices are reported.

Appendix A reports some theoretical notions about charge transport in organic semiconductors.

Chapter 2

Hybrid heterostructures based on bi-dimensional materials: the 2D Black Phosphorus case

Introduction

As mentioned in the introduction, the discovery of the unique properties concerning the bidimensional semiconducting and conducting materials, led to the exploration of almost the entire periodic table, searching for other materials having interesting properties.

Among them, bidimensional black phosphorous (2D bP), whose single layer is called phosphorene,[61] is the object of extensive studies in the plethora of semiconducting 2D materials due to its appealing properties.

In general, the sp^3 hybridization of the phosphorus atoms in the phosphorene layers led to a unique puckered honeycomb structure, which result in strong anisotropic optical,[62] thermal,[63] and electronic[64] properties along two axes named armchair and zig-zag direction (Figure 2.1).

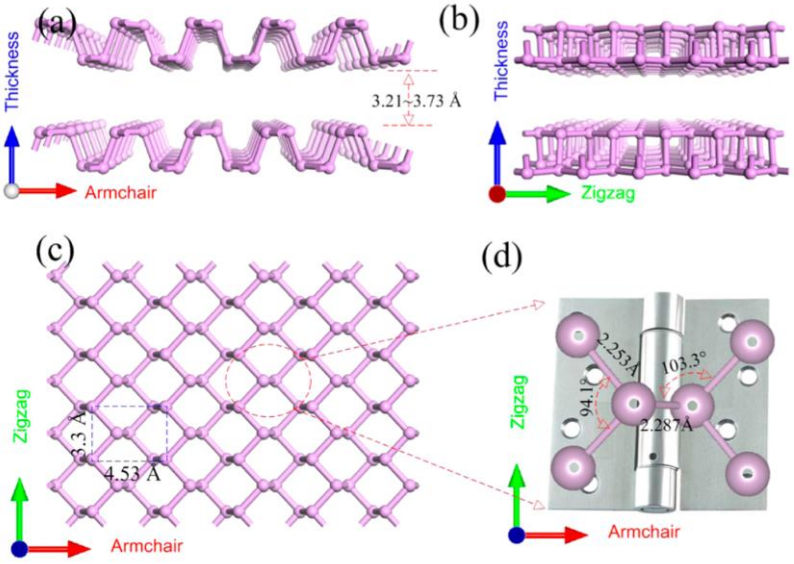

Figure 2.1. Phosphorene structure. a) and b) side views respectively of armchair and zig-zag directions; c) top view of puckered phosphorene structure; d) zoomed-in local atomic structure of the P-P bonding configuration. Reprinted with permission from J. Phys. Chem. Lett. 2015, 6, 14, 2794–2805. Copyright 2015 American Chemical Society.

One of the most appealing properties is the direct and tunable band gap that range from 0.3 eV for the bulk to 2.2 eV for the monolayer.[65] Considering the electrical characteristics as semiconductor, 2D bP shows outstanding properties such as a high charge mobility in the order of $\approx 10^5$ $cm^2 V^{-1} s^{-1}$ [66]and an on/off current ratio of 10^5 [67] measured in field-effect transistor (FET) devices. In addition, the feature of showing emissive excitons with a large binding energy (0.9 ± 0.12 eV),[68] makes it an extremely suitable material for optoelectronic applications.[69]

2D bP can be obtained from the exfoliation of the layered bulk black phosphorus, the most stable elemental phosphorus allotrope at room temperature,[70] by either liquid[71–76] or mechanical[66,67] cleavage.

The exfoliation of black phosphorus is a complex challenge because the P—P bond is stronger than C—C one, thus the interaction between the black phosphorus layers can be higher with respect to the other 2D materials.[77,78]

Liquid exfoliation is usually performed starting from the black phosphorus crystal sonicating it in anhydrous organic solvents such as dimethyl sulfoxide (DMSO)[72] or N,N-dimethylformamide (DMF). Both the solvents have high dielectric constant and surface tension, this guarantees high adhesion between the solvent molecules and the black phosphorus layers, resulting in a high-stable dispersion, as confirmed by molecular dynamic.[79] The lateral dimensions and thickness of the flakes are modified acting on the solvents and, on both time, and sonication speed. This exfoliation process leads to highly dispersed flakes in terms of lateral dimensions and thickness. In addition, the solvents typically used for liquid exfoliation have low volatility, resulting in low-grade purity of 2D bP flakes.

Alternatively, is possible to exfoliate black phosphorus by mechanical exfoliation.[80] This process is made by scotch tape, as with graphene exfoliation, but is performed in an inert atmosphere (glovebox). The exfoliation takes place by repeating folding, in different directions, of the scotch tape containing a black phosphorus crystal. Then, 2D bP is deposited on the substrates by simple adhesion of the adhesive tape containing the exfoliated bP with the substrates. The advantages of mechanical cleavage with respect to liquid exfoliation are the easiness of the process and the absence of solvents, which permits to obtain of highly clean 2D bP flakes. Nevertheless, despite the lateral dimensions of the obtained flakes being higher with respect to the liquid exfoliation, they remain out of control.

Summarizing the deposition techniques, it is possible to assert that both mechanical and liquid exfoliation are without control over the shape, size, and thickness. While

mechanical exfoliation is not appropriate for mass production, liquid phase exfoliation approach can be effectively utilized to enhance the quantities of 2D bP produced[81,82] in view of optoelectronic device development.

Together with limited large-scale production of phosphorene, the device development and the implementation of 2D black phosphorus in real settings applications is still limited because of its extremely high reactivity with water and oxygen.[83,84] In fact, air exposure leads to a deep structure modification and consequently to a strong degradation of 2D bP properties.

To date, most of the works concerning the optoelectronic properties of 2D bP, take into account how to effectively prevents 2D bP flakes from oxidation when they are exposed to air, by using for example chemical passivation or a physical barrier. In some of these works, the phosphorene flakes have been embedded into a polymeric matrix[85,86] or covered with a thick layer of poly(methyl methacrylate) (PMMA). In other cases, the flakes have been covered with a thick inorganic layer such as Al_2O_3[87] or have been covalently modified[88] to remain stable in air and to maintain their properties.

On the basis of all these considerations, the aim of my scientific activity concerning the topic of 2D bP is to properly develop/engineer heterostructures 2D bP-based in order to (i) improve the stability of the material, (ii) add multifunctionality, and (iii) develop new routes towards large-area deposition for expanding the usability in real-life applications of this promising 2D material.

In the following paragraphs are described (2.1) the chemical passivation of 2D bP by linear alkane, resulting in a sub-component of a complete metal-insulator-semiconductor devices (MIS) structure; (2.2) the non-covalent functionalization of 2D bP with fluorescent pyrene-boronic derivatives, as a passivating layer and molecular oxygen probe; (2.3) the in-situ deposition of Au NPs “stabilizer free” with catalytic properties; (2.4) the electrospray deposition on large-scale of oxidized 2D bP with piezoelectric properties.

The experimental activity presented in this thesis was framed within the European project PHOSFUN, an ERC Advanced Grant assigned to M.P. as PI (grant agreement no. 670173).

2.1 Insulator-semiconductor heterostructure of linear alkane on 2D bP

Part of this paragraph is adapted from:

M. Bolognesi, M. Brucale, A. Lorenzoni, F. Prescimone, S. Moschetto, V. V. Korolkov, M. Baldoni, M. Serrano-Ruiz, M. Caporali, F. Mercuri, E. Besley, M. Muccini, M. Peruzzini, P. H. Beton and S. Toffanin

Nanoscale, **2019**, 11, 17252, reproduced from Ref. [89] with permission from the Royal Society of Chemistry.

The formation of covalent bonds on the 2D bP surface strongly modifies the structure and the electronic configuration of the material, often extensively changing its properties.
The realization of a heterostructure where all starting features are preserved requires a softer approach. The weak interactions between organic molecules and 2D bP, for example through vdW forces, may preserve and permit the addition of new functionalities or the improvement of the intrinsic ones.
Under this light, it was select inert linear alkanes to improve the chemical stability of 2D bP flakes, adding at the same time, a functional layer for the development of micro and nano metal-insulator-semiconductor devices (MIS).[90–93]
Because of several advantages, such as high lateral mobility on the 2D bP surface which permits a self-ordering upon mild thermal treatments, easy solubility in organic solvents and low melting point and vapor pressure, easy visualization at the atomic scale by atomic force microscopy (AFM), linear alkane C24 (tetracosane) was selected.
In order to determine the molecular orientation and the ordering of the deposited C24 layer, a crystal of bulk black phosphorus was considered as the first system of study. After the deposition of a monolayer of C24 by dip coating, the surface coverage of the bulk black phosphorus was investigated by high resolution atomic force microscopy (HR-AFM).

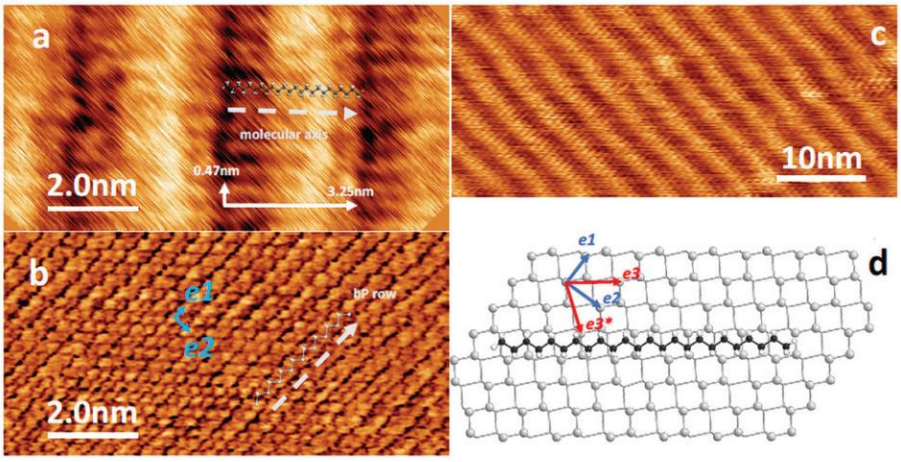

Figure 2.1.1. (a) Lamellar rows of C24 alkane arranged on the bulk bP surfaces; (b) AFM tapping mode scan of the bP surface after C24 molecules were removed in the same area as imaged in (a); (c) larger area image showing the lamellar

rows; (d) schematic crystalline structure of the bP surface with an overlaid C24 molecule. Reproduced from Ref. [89] with permission from the Royal Society of Chemistry.

The AFM images have revealed a lamellar arrangement of C24 molecules on the surface of the C24 crystal, as shown in Figures 2.1.1a and c. In particular, a row spacing of 3.25 ± 0.06 nm and a periodicity of 0.47 ± 0.02 nm were measured. These values are in excellent agreement with single crystal X-ray diffraction data of linear C24 (a = 3.254 nm, b = 0.482 nm).[94]

By increasing the tip-sample force the layer of alkane was removed, in order to determinate the orientation of the underlying bulk bP surface (Figure 2.1.1b). The surface of the crystal appears as zigzag row with a separation of 0.44 ± 0.02 nm and a spacing of 0.33 ± 0.02 nm, which perfectly matches the lattice vectors of the bP surface.[95–98] In Figure 2.1.1d the lattice vectors e1 and e2 are shown, and the unit cell diagonal is denoted as e3; this direction is at an angle of 53.1° to the e1 lattice vector. There is an equivalent symmetry direction denoted e3*, at an angle of 73.6° to the e3 direction, which is expected to result in a symmetry-equivalent ordering leading to a second domain rotated by this angle. Since both the images 2.1.1a and b have the same orientations, it is reasonable to assert that the C24 molecules lie in the e3 direction (Figure 2.1.1d).

In order to confirm the orientation of the molecules, the system was simulated by molecular dynamic (MD) calculations, which revealed the presence of three favorable directions e1, e3/e3*. The latter are considered isoenergetic directions, separated by an angle of 73.6°. The MD calculations have proven that, after the thermal equilibration, the alkane molecules order epitaxially along these two directions.

Once found the organization and the orientation of the alkane molecules on the surface of bulk bP, which represents the model system, the attention was focused on the heterostructure of interest based on 2D bP. The monolayer deposition on the bi-dimensional material may be affected by the boundary effects, reduced planarity, and can suffer from a large amount of defects present in 2D bP with respect to the correspondent bulk material.

To reproduce the surface coverage of a monolayer of C24 on 2D bP it was used the same dip coating technique, starting from a C24 ethanolic solution.

To obtain 2D bP micrometric flakes, a bulk bP crystal was mechanically exfoliated with the scotch tape method (35 times folding). 2D bP flakes were then transferred onto either quartz or conductive silicon substrates. The distribution and size of 2D bP flakes on the

substrates was analyzed by optical microscopy, revealing a coverage of around 4%, while the mean lateral size of the flakes is around 1 micron (see paragraph 5.1).

The AFM images performed on the C24 monolayer (Figure 2.1.2 a-c) deposited on top of 2D bP, have shown continuous domains in the range of 100-200 nm of C24 arranged in parallel lamellae (Figure 2.1.2b). The relatively large area of the domains has permitted the visualization of lamellae oriented in two different epitaxial directions, forming an angle of 75 ± 5°. The observed angle corresponds to the e3/e3* directions and is in perfect agreement with the AFM images performed on bulk bP and with MD simulation.

The different domains were separated by zones at higher average heights of C24, without lamellar arrangement, and then classified as amorphous material.

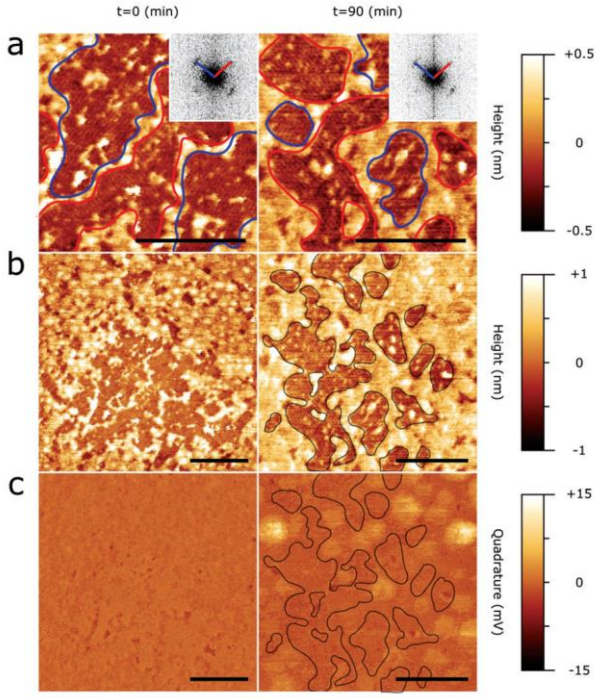

Figure 2.1.2. Epitaxial ordering and oxidation inhibition characteristics of a C24 monolayer on 2D bP flakes. (a, b, c): representative morphology (a, b) and PeakForce Tapping quadrature (c) micrographs of a 2D BP flake with a C24 monolayer on top deposited by dip coating (see Materials and methods) immediately after functionalization (left column) or after 90 minutes (right column) of exposition to humid air. All scale bars are 100 nm. (a): Details of the ordered domains with corresponding 2D FFT plots (insets). Solid blue and red lines outline domains showing features aligned in the same general direction, with the corresponding 2D FFT peaks highlighted in the same color. (b): Zoomed-out view of the same zones showing a typical distribution of ordered and disordered domains immediately after deposition (left) or after 90 minutes of air exposure (right; ordered domains are outlined with a solid black line). (c): Quadrature signal of the same areas depicted in panel (b), evidencing the first signs of oxidation damage. The solid black outlines in the right panel correspond to ordered domains identified from the image directly above; these zones appear considerably less subject to oxidation. Reproduced from Ref. [89] with permission from the Royal Society of Chemistry.

From the stability point of view, the protective effect of the C24 monolayer was effective if compared with the pristine bulk bP. In fact, while the exposition in air of the pristine black phosphorus causes in it the typical protrusions for the oxidated flakes after a few minutes and dominates after 1 hour, for 2D bP covered with C24 the same process became significant after 90 minutes (Figure 2.1.2, right column) and reach a qualitatively similar level of bulk bP after 4 hours (see Figure S5, SI). The majority of the oxidated zones appear in the corresponding of areas covered by amorphous C24, suggesting that the ordered C24 layers are more effective against oxidation with respect to the amorphous one.

To improve the protecting properties of epitaxial C24 layers on 2D bP flakes it was next used nanometer size multilayers of C24. To this aim, 2D bP flakes on quartz substrates were spun coated with C24 molecules from chloroform solution at varying concentrations and with different post-deposition thermal treatments to optimize coverage and epitaxial ordering.

In this context, the most relevant parameter within the process was revealed the post-annealing process. By increasing the annealing temperature from 85° C to 120°C and finally to 150°C, a gradual order of the C24 chains was obtained. In particular, the AFM images have revealed that the coverage with ordered lamellae pass, respectively with the increasing temperature, from 0% to 72-89% and to 97% of scanned areas.
In this case, the observed reciprocal orientations of the C24 alkane chains form an angle of 69 ± 5°, suggesting that the same order of the layers lying on the 2D bP surface, corresponding to the e3/e3* directions, was propagated to the successive deposited layers.

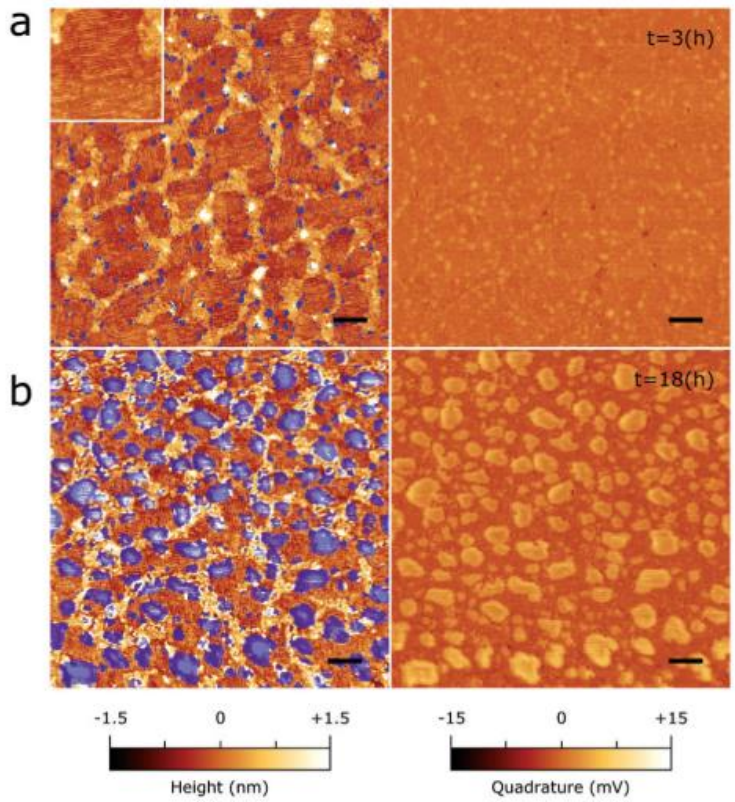

Figure 2.1.3. Inhibition of the 2D bP oxidation by epitaxial C24 multilayers. Topography (left) and peakforce quadrature signal (right) of a 1 μm^2 area of a 2D bP flake functionalized with multilayered C24 exposed to humid air for 3 h (a) or 18 h (b). Scale bar is 100 nm. Inset of panel (a) is 150 × 150 nm. Reproduced from Ref. [89] with permission from the Royal Society of Chemistry.

The protective effects of the multilayers on 2D bP were investigated by AFM, acquiring the images of a sample left in air over 18 hours. During the first 3 hours of exposure, the topographic image does not reveal significant changes of the usual features associated to the 2D bP oxidation (Figure 2.1.3, left). Focusing on the peakforce quadrature micrograph image (Figure 2.1.3, right), an appreciable signal contrast starts to emerge, signaling the first stage of the oxidation process. Marking in purple the corresponding zones in the topography image on the left, it is the evident that the oxidation process starts at the boundaries between epitaxially ordered C24 domains. Hence, the start of the oxidation process could be due to a depletion of C24 in these zones, probably caused by the molecular rearrangements of the alkane chains.

After 18 hours of air exposure, the AFM images performed on the same area of the same sample showed considerable progress of the oxidation process (Figure 2.1.3b). Despite the enhanced growth of the oxidation protrusions, it is to be noted that the areas covered by ordered lamellae were unperturbed by oxidation.

Therefore, it is possible to resume that the epitaxial multilayers coverage is more effective with respect to the monolayers, delaying the oxidation process from 1 hour to 18 hours, in comparison with the bare bP. Moreover, the unperturbed areas under the epitaxially ordered domains suggest that the minimizing of deposition defects at boundaries could give 2D bP significant long-term stability.

Finally, the system was investigated by electrostatic force microscopy (EFM) in order to acquire electrical information on the 2D bP/C24 heterostructure. The electrical characteristics of the as- realized system were investigated in order to assess if the heterostructure might behave as a semiconductor/insulator sub- component in a complete MIS stack. All the images were acquired at a constant height of 100 nm above the topography profile, to prevent tip-sample contact, and keeping a constant voltage of +2 V bias between tip and sample.

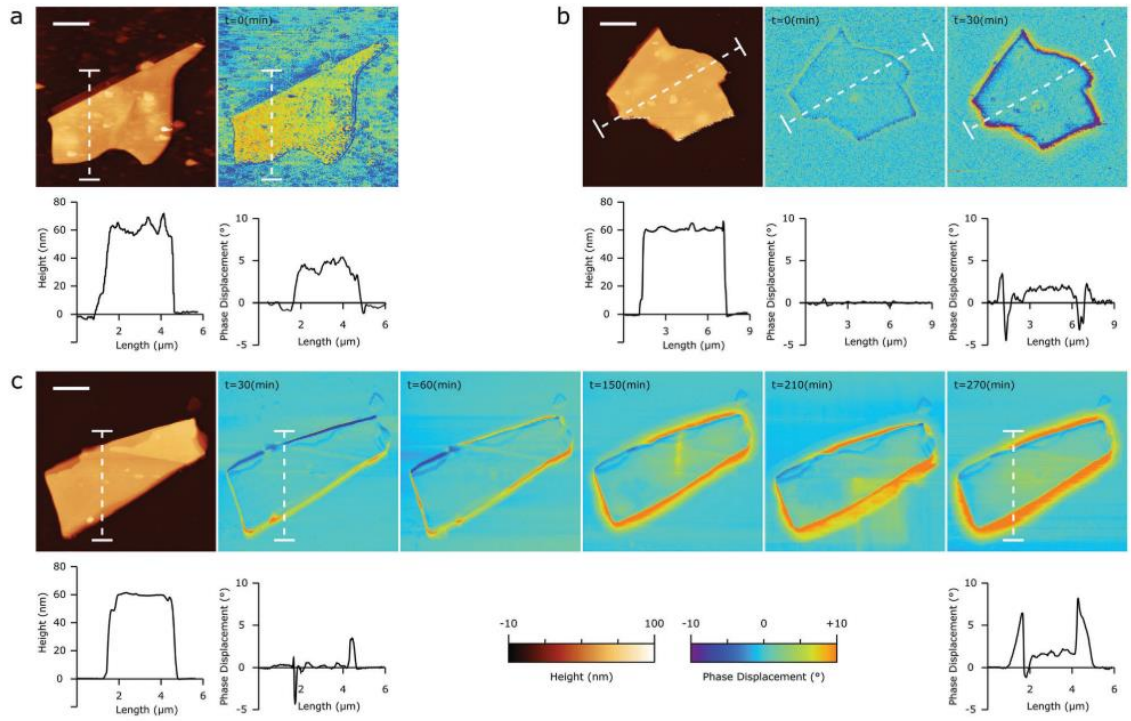

Figure 2.1.4. AFM and EFM micrographs performed at increasing time exposure in air of (a) pristine 2D bP, (b) 2D bP covered with a C24 monolayer and (c) 2D bP covered with C24 multilayer. Scale bars are 2 μm. Reproduced from Ref. [89] with permission from the Royal Society of Chemistry.

Firstly, as reference signal was acquired the EFM image of pristine 2D bP on a conductive doped Si substrate (Figure 2.1.4a, right). By comparing the same plotted phase displacement signal of pristine 2D bP with the 2D bP covered with a monolayer of C24 (Figure 2.1.4b, center), it is possible to note that the signal here is totally suppressed, confirming the insulator properties of C24.

After 30 minutes of air exposure, the phase signal of 2D bP coated with a C24 monolayer is already shifted with respect to the substrate (Figure 2.1.4b, right).

The EFM mapping on a 2D bP flake coated with C24 multilayers, showed instead an unperturbed signal after 30 minutes (Figure 2.1.4c), starting the modulation of the phase signal after 150 minutes.

It is to be noted that the phase signal is not appreciably changed on the 2D bP surface even after 270 minutes, localizing most of the signal change at the sidewall of the 2D bP flake, most probably not covered by C24 alkane.

Once again, it is possible to deduce that the improvement in the C24 film homogeneity could enhance the 2D bP protection against oxidation.

From the qualitative analysis of EFM maps is possible to conclude that: i) C24 coating acts as insulator material; ii) the oxidation process modifies the electrical properties of 2D bP; iii) C24 multilayers coating is very effective against oxidation.

In summary, the examined C24/2D bP system demonstrated a new example of multifunctional heterostructure. On one hand, the C24 layer was revealed as a very effective material to prevent 2D bP oxidation, able to resist more than 18h when epitaxially grown, as confirmed by AFM. On the other hand, together with the protective properties, EFM characterization has confirmed the insulator nature of C24 coating. Overall, this vdW heterostructure corresponds to an insulator-semiconductor (C24-2D bP) stack, which can consider a building block of the well-known MIS structure, increasingly relevant in micro- and nanoelectronics, photonics and optoelectronics applications.

2.2 Heterostructure of 2D bP/fluorescent boronic derivatives for molecular oxygen probe

Part of this paragraph is adapted from:

M. Bolognesi, S. Moschetto, M. Trapani, A. F. Prescimone, C. Ferroni, G. Manca, A, Ienco, S. Borsacchi, M. Caporali, M. Muccini, M. Peruzzini, M. Serrano-Ruiz, L. Calucci, M. A. Castriciano and S. Toffanin

ACS Applied Materials and Interfaces, **2019**, 11(25), 22637, reproduced from Ref. [99]
(https://pubs.acs.org/doi/10.1021/acsami.9b04344#)
Further permissions related to the material excerpted should be directed to the ACS.

The high oxygen reactivity of bi-dimensional black phosphorus, appropriately exploited, has been transformed into an opportunity to realize a heterostructure 2D bP-based with new functionality and usable for real-setting applications.

Considering the well-known chemical affinity between phosphorus and boron atoms, such as the phosphine that react with boron precursor to give phosphinoboranes or borylphosphines (respectively containing double and single P—B bonds), a strong chemical affinity between the phosphorus atoms of the phosphorene and compounds containing boron atoms, was expected. Because of these considerations, boronic derivatives, acid, and ester, endowed with pyrene moieties were selected. Pyrene is a solvatochromic, conjugated, planar fluorophore largely investigated for wide use in optoelectronic and sensing applications.[100,101] Pyrenes are characterized by long excited-state lifetimes, which depend on the chemical environmental conditions, i.e., the nature of the solvent or the presence of some molecules in solution such as oxygen.[102–104] On the basis of these premises, pyrene has been selected as oxygen probe in this heterostructure.

2D bP was then functionalized in solution using pyrene (Py), pyrenboronic acid (PBA), and pyrenboronic ester (PBE) reported in Figure 2.2.1.

The suspension of 2D bP was obtained from the liquid exfoliation by sonication in dimethylsulfoxide (DMSO).[71] Successively, the 2D bP suspension was dried and then dispersed again in anhydrous tetrahydrofuran (THF) with either Py, PBA and PBE to obtain the adducts in suspension.

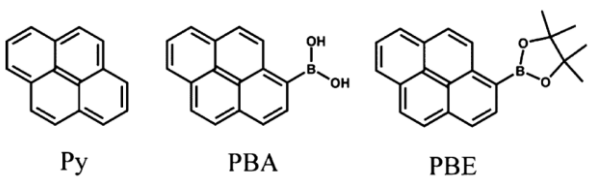

Figure 2.2.1. Chemical structure of Py, PBA and PBE. Reproduced from Ref. [99]. Further permissions related to the material excerpted should be directed to the ACS.

The interaction between 2D bP and pyrenboronic derivatives was predicted by density functional theory (DFT) calculations. In particular, calculations have revealed the noncovalent nature of the interactions between pyrene derivatives and phosphorene flakes. The formation of stable adducts was also estimated, with stabilization energy that increases from Py/2D bP, to PBA/2D bP and to PBE/2D bP (respectively, Figure 2.2.2 a, b and c).

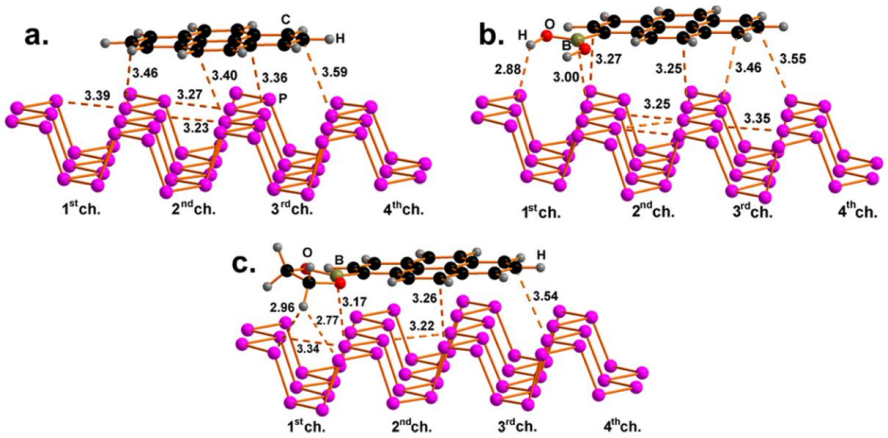

Figure 2.2.2. Optimized structure of the adducts of phosphorene with Py (a), PBA (b), and PBE (c). Reproduced from Ref. [99]. Further permissions related to the material excerpted should be directed to the ACS.

Moreover, a bandgap lowering of 2D bP was noticed in the PBA and PBE adducts as the effect of the partial mixing between the free lone pairs of 2D bP and the π* orbital of the pyrene-based moiety.

The confirmation of the predicted interactions was carried out by multinuclear solid-state NMR (ss-NMR), which was performed, for the first time ever, on a 2D bP suspension. The signals of carbon, boron, and hydrogen atoms of the measurements performed on suspensions of bi-dimensional black phosphorus and pyrene derivatives, revealed and confirmed the noncovalent nature of the interactions also in the case of PBA and PBE adducts.

Thanks to the presence of fluorescent probes, the fluorescence decay lifetimes of the adducts were investigated by time-correlated single-photon counting (TCSPC), in order to understand the behavior of the adducts in the presence or in absence of oxygen. The fluorescence decay lifetimes were elongated for all three adducts with respect to the pyrene derivatives alone, passing from 1.2 to 3.1 ns for Py, from 53.3 to 61.3 ns for PBA, from 40.1 to 60.2 ns for PBE, respectively without and with 2D bP. Once again, this trend confirms that the stabilization energy became stronger with the order Py < PBA < PBE, and can arise from the different energetic displacement and geometry of the vibronic levels of Py, PBA, and PBE or to a different coupling of these vibronic states with those of 2D bP. In fact, while in Py/ 2D bP the coupling occurs just through the pyrene core, in PBA and PBE the boron functionality adds further interactions with the phosphorus atoms of 2D bP, which are stronger for the ester than for the acid group.

Since the decrease of the fluorescence lifetime in the pyrenboronic systems is ascribable to the presence of oxygen,[105] it was performed time-resolved fluorescence spectroscopy

on the adducts without and with exposition to air. By comparing the weighted average lifetimes of the pyrene compounds alone and the 2D bP-based adducts exposed to air, the signal variation due to the flux of oxygen results increased by 1.5 times in the 2D bP/PBA adduct, passing from a ratio of 1.7 to 2.6.

Analyzing the signals relative to 2D bP/PBE adduct, the signal increase with respect to the PBE alone is 2.6, even higher than 2D bP/PBA adduct.

The fluorescence decays of the adducts prepared with 2D bP previously oxidized, showed the same behaviour of adducts prepared with pristine 2D bP. In addition, by degassing the suspension of the adducts, the fluorescence decays values are not restored. Hence, it is possible to assume that the observed fluorescence-lifetime variations in the adducts with and without oxygen, are due to the interactions of PBA and PBE directly with the oxidized sites of 2D bP (PO_x).

Considering the possible degradation in time of the as-prepared heterostructures, the position and the intensity of signals in Raman spectra for freshly prepared and 6-month aged adducts exposed to air remain constant. On the other hand, the spectrum of 3-month aged bare 2D bP in air is featureless and flat. Thus, while pristine 2D bP undergoes severe degradation in air, its crystalline structure in the adducts is preserved from oxidation in air for over 6 months.[106]

In conclusion, the favorable coupling between 2D bP and pyrene derivatives had a two-fold impact on the phosphorene properties, enhancing its chemical stability on the one hand, and adding the possibility of a future implementation as an oxygen probe on the other hand. In particular, the DFT simulation predicted noncovalent coupling between the core of pyrene and the phosphorus atoms of 2D bP, successively confirmed by NMR spectra in suspension. From a stability point of view, Raman spectroscopy has confirmed that 2D bP/pyrene-derivatives heterostructures are stable in air for more than 6 months. Finally, thanks to the presence of a luminescent probe such as pyrene, the time-resolved fluorescence data evidenced that, in the adducts, the pyrene derivatives are stabilized in their excited state by 2D bP. Together with this, the systems showed relevant modulation of their fluorescence decay time constants with respect to the pyrenic derivatives alone, thus indicating a high propensity of these heterostructures toward a possible implementation as active materials in a fluorescent chemosensor for oxygen detection.

2.3 2D bP/Au nanoparticles "stabilizer-free" heterostructure through in-situ deposition

Part of this paragraph is adapted from:

S. Moschetto, A. Ienco, G. Manca, M. Serrano-Ruiz, M. Peruzzini, A. Mezzi, M. Brucale, M. Bolognesi and S. Toffanin
Dalton Transaction, **2021**, 50, 11610, reproduced from Ref. [107] with permission from the Royal Society of Chemistry.

The superficial deposition of metal in the form of metal atoms, molecular fragments, or nanoparticles (NPs), adds intriguing properties to the 2D bP as a result of structural and electronic variations,[108] leading to a variety of applications including sensing,[109] energy generation[110] and conversion,[111] catalysis.[112]

In particular, thanks to the capability to produce singlet oxygen coupled with the localized surface plasmonic resonance (LSPR) effect, 2D bP/Au NPs heterostructures are studied for sensing and diagnostic/therapeutic applications.[113–115]

On another side, the catalytic activity of either 2D bP[116] and Au NPs coupled with the anti-aggregation effect of 2D bP onto the nanoparticles results in a very efficient heterostructure for catalytic applications.[117]

Despite the numerous systems and the variety of studied applications, a deeper insight into the electronic and structural properties at the 2D bP/Au NPs interface is still lacking. Usually, once synthesized, AuNPs need to be stabilized to prevent aggregation or agglomeration. Therefore, are used several molecules which induce stability through several types of interactions, such as electrostatic, steric, and electrosteric interactions.[118]

Aimed to fill this gap, an *in-situ* Au NPs deposition was developed to obtain a strong intimacy of contact between Au NPs and 2D bP, removing the stabilizer presence and obtaining well-distributed and homogeneous morphology at the nanoscale.

As the first step to realize the 2D bP/Au NPs heterostructure, 2D bP was mechanically exfoliated by blue tape from bulk bP onto Si/SiO2 substrates or quartz, obtaining flakes with an average lateral size of around 1μm and thickness from 50 nm to a few nm,[89] which cover the 4% of the substrates total area (see paragraph 5.1).

To obtain the in-situ reaction between 2D bP and the Au precursor, the substrates of quartz and Si/SiO2 with exfoliated 2D bP were functionalized by dipping them in a 10^{-3} M solution of gold precursor, Chloro(dimethylsulfide)gold(I), $[(CH_3)_2S]AuCl$, in anhydrous $CHCl_3$. The samples were obtained under inert atmosphere of N_2 (glove box),

in the dark and at room temperature. Different immersion times of 3, 18, and 72 hours were tested in order to obtain different sizes of Au NPs onto 2D bP.

Through this deposition–precipitation solid–liquid heterogeneous reaction starting directly from a metalloorganic Au(I) pre-cursor, it was specifically avoided the use of a surfactant that can modulate the interaction with the 2D bP, as happens in the case of graphene.[119,120] The mechanism is due to the presence of a labile dimethylsulfide ligand and a Cl- ligand in the precursor, which is easily reduced when in contact with the 2D bP surface.

Raman spectroscopy was performed on both pristine and Au functionalized 2D bP, revealing for all samples the three typical Raman peaks of bP at 360, 435 and 460 cm^{-1}, attributed to the A^1_g, B^2_g, and A^2_g vibrational modes, respectively (Figure 2.3.1a).[121–123] This confirms that the orthorhombic crystalline structure of 2D bP is maintained after Au-functionalization, at least in the atomic-thin layers of 2D bP under the functionalized surface. In fact, as reported in the literature, covalent surface functionalization of 2D bP causes only a slight weakening of all bP Raman features (in particular of the A^1_g mode) due to the partial disruption of intra-layer phosphorus bonding.[88]

UV-vis spectroscopy on pristine 2D bP and Au-functionalized samples on quartz (incubation time 3h, Figure 2.3.1b) resulted in broad and featureless absorption spectra for both samples, typical of bP. The expected peak showing plasmonic effects, (at about 520 nm, typical of Au NPs with size <10 nm as described in the following morphological characterization),[111] is not present. This may be either ascribed to: i) a low coverage of Au nanoclusters ii) quenching by 2D bP, or, iii) a combination of both factors. These assumptions are supported by literature, where it is supposed that the realization of 2D bP-anchored Au nanoclusters follows a kinetically controlled process,[124] and quenching effects occur also for graphene and other 2D materials.[125,126] Forming Au nanoclusters on the surface of 2D bP under experimental conditions featuring a low ratio between the Au precursor and the 2D bP (down to 2.5%) might enhance the collision probability between Au(I) atoms from the precursor and P centers from 2D bP, enabling an easier study of the heterostructure due to the large fraction of Au-P binding sites. However, we cannot exclude a-priori that the increase of the absorption spectrum of the 2D bP/Au-functionalized sample in the 400-475 nm spectral range is due to scattering effects.

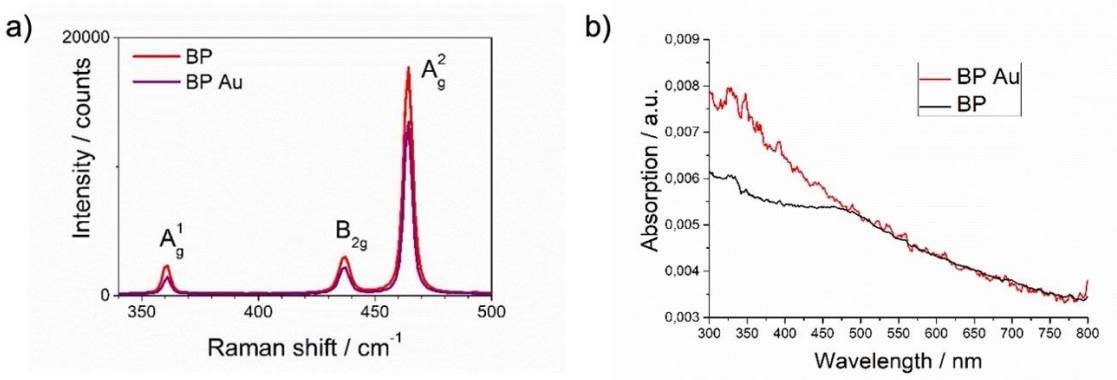

Figure 2.3.1. a) Raman spectra of pristine 2D bP (red) and Au-functionalized 2D bP (purple) on Si/SiO2 substrates. b) Absorption spectra of mechanically exfoliated pristine bP (black) and bP functionalized with gold NPs (red) on quartz substrates. Reproduced from Ref. [107] with permission from the Royal Society of Chemistry.

The AFM image of the bare 2D bP mechanically exfoliated (Figure 2.3.2a) has confirmed the good quality of the deposited material, highlighting the expected planarity and featureless of the surface, with occasional sharp steps of several Å (the smallest measuring 6.6 ± 1.0 Å, see Figure 2.3.2e).

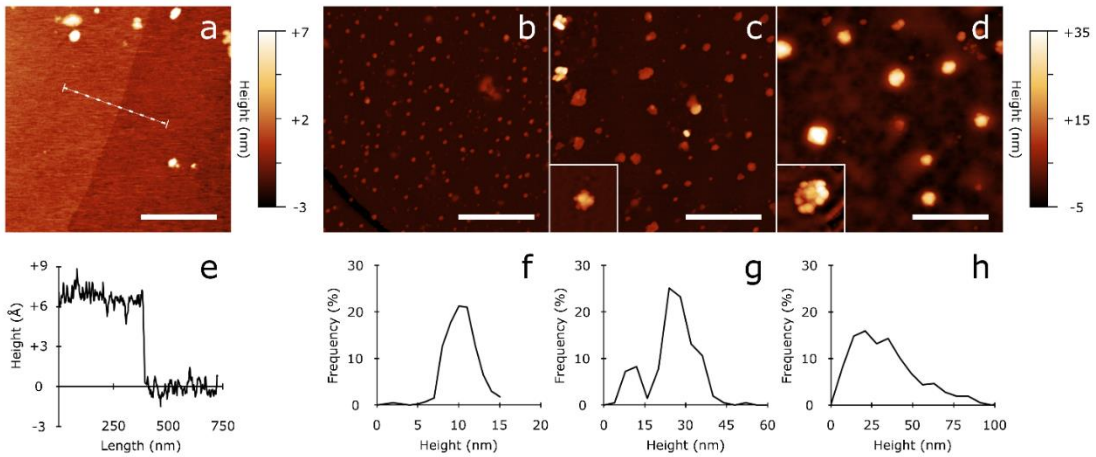

Figure 2.3.2. (a, b, c, d): representative AFM micrographs of bP flakes immediately after mechanical cleavage (a) and after incubation with [(Me_2S)AuCl] for 3h (b), 18h (c) and 72h (d). All scale bars are 500 nm. Insets of panel (c) and (d) show 4x magnifications of the larger Au clusters found on the corresponding sample. (e): height profile of a typical step found on pristine bP measured along the dashed line shown in panel (a). (f,g,h): maximum vertical size distributions of Au NPs and clusters with respect to the BP plane in samples incubated for 3h (f), 18h (g) and 72h (h). Reproduced from Ref. [107] with permission from the Royal Society of Chemistry.

The comprehensive analysis of the samples revealed that longer incubation times with [$(CH_3)_2S$]AuCl led to the formation of larger Au NPs clusters: the sample incubated for 3h is largely decorated by isolated spherical Au NPs with an average size of = 10.2 ± 3.5 nm (Figure 2.3.2f). At 18h, the average diameter of these larger aggregates is 27.0 ± 10.4

nm (Figure 2.3.2g), while at 72h the distribution further broadens to include aggregates up to ~100 nm in diameter (Figure 2.3.2h).

On account of these results, it is possible to assert that the in-situ process is effective in the production of nm-sized nanoparticles with high affinity towards the 2D bP surface.

In order to get deep insight into the intimate interactions at the interface between 2D bP and Au NPs, X-ray photoelectron spectroscopy (XPS) was performed. Since the lateral resolution of the utilized equipment was around 20 μm and the lateral average size of 2D bP flakes was 1 μm, the obtained values relative to the binding energies were collected in region A and region B, indicating respectively the region in presence and in absence of 2D bP. In fact, in region A were detected the P 2p peak at BE = 130.0 eV, characteristic for elemental P as it was found in the pristine bP reference sample and then attributable to 2D bP (Figure 2.3.3).[127] In addition, the Au $4f_{7/2}$ peak was positioned at BE = 84.4 ÷ 84.8 eV instead of BE = 84.0 eV, typical Au$4f_{7/2}$ peak of bulk gold (Au^0). This chemical shift strongly suggests an electronic interaction occurring between Au atoms and the 2D bP surface.

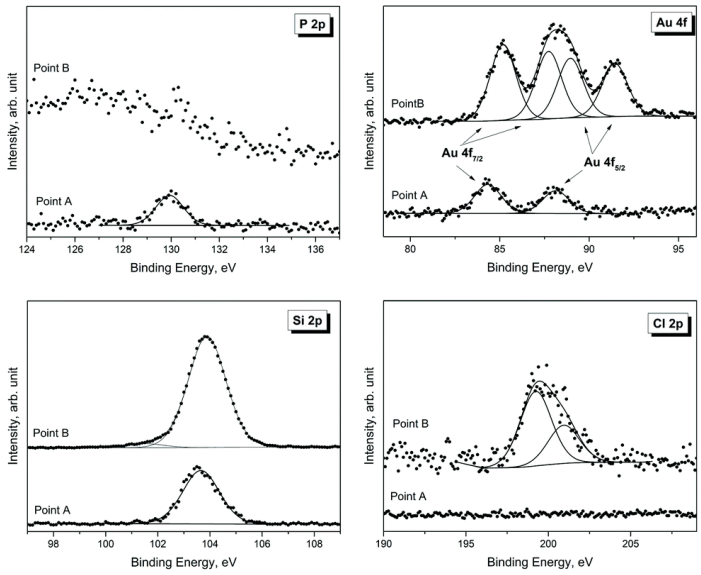

Figure 2.3.3. XPS spectra, acquired in regions A and B of samples of 2D bP flakes functionalized with Au NPs on a Si/SiO2 substrate. Reproduced from Ref. [107] with permission from the Royal Society of Chemistry.

In the B regions, where 2D bP was absent (no P 2p signal was detected), the Au 4f signal showed two doublets Au$4f_{7/2}$-Au$4f_{5/2}$, assigned to two different electronic configurations of Au centres (i.e. Au^+ and Au^{3+}).[128] In the same point, also the Cl 2p signal was detected at peak position with BE = 199.2 eV (Figure 2.3.3). This value is characteristic for Cl^-, most probably due to the presence of Cl^- counteranions necessary to electronically stabilize Au^+ and Au^{3+} atoms on the NPs surface in the absence of 2D bP.

To further evaluate the nature and the amount of interactions between the materials at the heterostructure interface, DFT computational study was carried out.

From the calculation, was revealed a slight positive charge (+0.2) on the Au atoms directly bonded to the P centers of the phosphorene. This, together with the observation of the positive overlap population of the Au-P interactions, confirms the XPS measurements, indicating that the Au NPs and nanoclusters present a fraction of Au atom in an oxidation state higher than 0. Hence, from an energetic point of view, simulations confirmed the propensity of 2D bP to bind the Au NPs by fixing a fraction of Au atoms at their periphery through a covalent bond.

From a structural viewpoint, simulations also confirmed that the 2D bP crystalline structure is perfectly preserved after the adsorption of Au NPs. Moreover, a partial charge transfer between P and Au atoms is revealed, with a positive charge being localized on the Au atoms directly bonded to the 2D bP. This may also explain the quenching of the plasmonic band of the Au NPs in the 2D bP/Au NPs heterostructure, as shown by absorption spectroscopy (Figure 2.3.1).

Finally, it was found that the greater is the size of the gold cluster and the smaller becomes the bandgap, starting from the 2.20 eV for the naked phosphorene and reaching the lowest limit of 1.41 eV for phosphorene functionalized with the tetranuclear gold cluster.

In conclusion, the realization of this heterostructure involving the soft-pairing of P atoms from the 2D bP surface and the Au NPs deposited in-situ and in total absence of stabilizer, makes clear that i) 2D bP fully preserves its crystalline structure beneath the interface with Au NPs, as evidenced by Raman spectroscopy; ii) a partial charge transfer at the 2D bP/Au interface occurs, with a positive charge being localized on the Au atoms directly bonded to 2D bP, as predicted by calculations and confirmed by XPS experiments; iii) a 2D bP band gap lowering which is more pronounced as the nuclearity of the Au clusters increases.

The proposed heterostructure gives a theorical insight and an overall deeper understanding of the interface in the heterostructures based on 2D bP/Au NPs leading to a “stabilizer-free” surface and optimal nanostructuring, holds promise for improved performance in specific applications, such as electro-, photo- or photoelectro-chemical catalysis, within others.

2.4 Controlled oxidation of 2D bP flakes by large-area electrospray deposition

Part of this paragraph is adapted from:

S. Moschetto, M. Bolognesi, F. Prescimone, M. Brucale, A. Mezzi, L. Ortolani, M. Caporali, P. Pingue, M. Serrano-Ruiz, D. Pisignano, M. Peruzzini, L. Persano, and S. Toffanin
ACS Applied Nano Materials, **2021**, 4 (4), 3476

Despite all the proposed chemical-physical approaches to realize 2D bP-based heterostructures with superior properties in terms of chemical stability and functionalities, the need to scale up the 2D bP deposition process requires to go further mechanical and liquid exfoliation techniques. Work on large-scale and highly controlled environmental conditions, given the high 2D bP reactivity with water and oxygen, bring to light the need to control the oxidation process in order to facilitate the working conditions. Consequently, as happened for graphene and graphene oxide,[130,131] although for different reasons, it becomes necessary to know the functional and structural characteristics of phosphorene oxides (2D PO_x).

In particular, phosphorene oxides have recently attracted the community for their potential application in electronic, optoelectronic, and energy- harvesting fields, showing high stability in ambient conditions. In particular, some recent works have predicted that the oxidized form of 2D bP can show piezoelectric properties,[132] namely the capacity to convert mechanical energy into electrical energy typical for the noncentrosymmetric crystalline structures, such as many metal oxides[133] and metal dichalcogenides.[134,135]

Inspired by these predictions, it was developed a method to deposit oxidized 2D bP flake on large-scale by an unconventional wet technique. In particular it was employed electrospray, a technique to deposit a material from solution by applying a large electric bias between a spraying nozzle and the substrate (Figure 2.4.1).

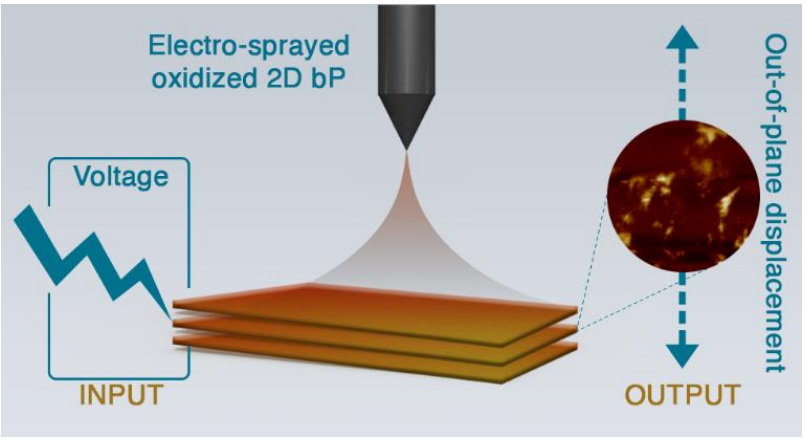

Figure 2.4.1. Schematic of the electrosprayed 2D bP with input and output figures. Figure by Moschetto et al. (ref. [129]) is licensed under CC BY-NC-ND 4.0.

The electrospray technique has been recently introduced for the deposition of electrodes in supercapacitors[136] and solar cells.[137] In general, electrospray works by applying a high bias (i.e, tens of kVs) between the liquid solution and a collector. Once the applied electric field overcomes the surface tension of an element of fluid formed at the termination of an electrified extruder, in fact, charged droplets are formed and sprayed, namely, accelerating toward the collector.

In this case, the 2D PO_x structures were deposited starting from a suspension of 2D bP in DMSO, which was pumped through a syringe into a stainless-steel nozzle (inner diameter, 200 μm) at a speed 0.5−1.0 mL/h, by applying a voltage of 11−20 kV between the nozzle and a metal support at a distance of 15 cm from the substrate. Given the high affinity of 2D bP toward the oxygen, the whole electrospray process was performed in air, in order to deposit material with high oxygen content.

From the optical characterization of the so deposited material there was clear evidence, in terms of dimensionality, of the crystalline 2D PO_x structures. In particular, the structures showed a high aspect ratio of 10.000 (thickness vs lateral dimension) with a very high average lateral dimension of flakes.

The optical image of the electrosprayed 2D bP (Figure 2.4.2a) highlights the largest elongated solid structures, with an average lateral size that range from tens to hundreds of μm^2. Moreover, the structures have a very low and homogeneous optical contrast, thus indicating a crystalline 2D nature of the material deposited.

On the contrary, the optical images of mechanically exfoliated bP (Figure 2.4.2c) or liquid phase-exfoliated bP (Figure 2.4.2e) indicate that much smaller crystalline flakes are obtained with these two techniques.

For a quantitative comparison, the mean surface areas of the flakes deposited by electrospray, mechanical cleavage and liquid-phase exfoliation were calculated, obtaining values of 480, 26.3, and 0.2 μm^2, respectively (Figure 10 b, d and f). These values clearly highlight the effectiveness of the proposed method for the deposition of large-area 2D structures.

A further morphological investigation of the surfaces of the electrosprayed structure was carried out by AFM, which revealed an atomically flat surface (full width at half-maximum (FWHM) of peak height is <1 nm) extended over a micrometric area. In addition, the morphology of the single-layer structures is highly stable and remains unchanged after overnight exposure to air, as observed from the AFM image taken on the same surface of the same 2D flake.

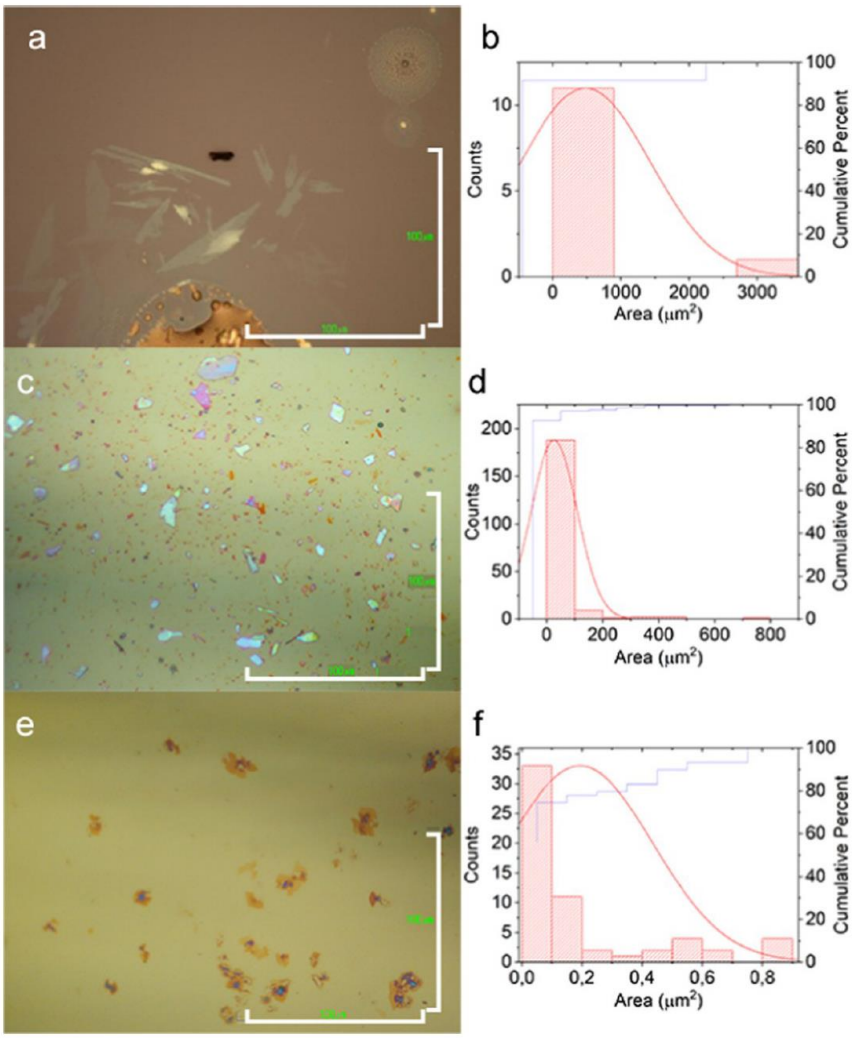

Figure 1.4.2. Typical optical micrographs of samples of: (a) 2D structures deposited by electrospraying and (b) relative surface area distribution; (c) 2D bP flakes obtained from the mechanical exfoliation ofbP and (d) relative surface area distribution; (e) 2D bP obtained by drop-casting a suspension of liquid-phase-exfoliated bP and (f) relative surface area distribution. Scale bar: 100 μm. Figure by Moschetto et al. (ref. [129]) is licensed under CC BY-NC-ND 4.0.

Also, multi-layered flakes were found. The height distribution graph obtained by AFM has revealed terraced structures with periodicity between layers of about 4.3 ± 0.3 nm, indicating a different structure if compared with the interlayer distance for pristine 2D bP[138] or 2D bP intercalated with solvent molecules.[139]

The repeated AFM scans on the surface revealed also higher mechanical fragility of the oxidized structures with respect to the mechanically deposited ones, as reported in the literature for phosphorene oxides.[140] More in detail, after 15 min of scan on the 2D PO_x surface, the flake showed a hole in the center and the force curves acquired showed a breakthrough event under 1-3 nN applied force. On the other hand, pristine 2D bP flake remained unperturbed after 270 min of scan and applying forces up to 5 nN.

To verify the composition of the deposited material by electrospray, XPS, energy-dispersive X-ray analysis (EDX) and transmission electron microscopy (TEM) analyses were performed on the surface of the samples.

XPS measurements revealed the P $2p_{3/2}$ peak positioned at BE = 134.1 eV, which is typical for P at higher oxidation state (+5) and thus theoretically imputable to P in the configuration of P_2O_5. In contrast, measurements performed onto pristine 2D bP mechanically exfoliated, have shown a P $2p_{3/2}$ peak positioned at BE = 130.0 eV, characteristic for P – P bond. These results confirm that the deposited material by the proposed electrospray deposition is a good method to produce oxidized phosphorene-based material, 2D PO_x.

The scanning electron microscopy (SEM) images and the EDX spectroscopy confirmed that the signal from oxidized species identified by XPS can be attributed to the electrosprayed material.

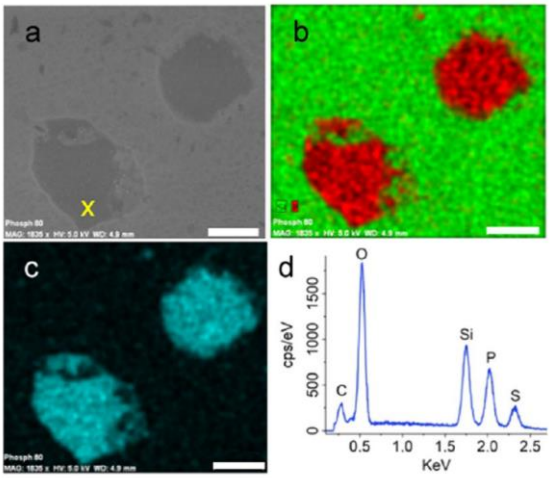

Figure 2.4.3. (a) SEM image of 2D PO_x flakes. (b, c) Phosphorus (red), silicon (green), and oxygen (cyan) EDX maps recorded from the 2D POx flakes shown in (a). (d) EDX spectrum taken at the point indicated with X in (a). Scale bar: 30 μm. Figure by Moschetto et al. (ref. [129]) is licensed under CC BY-NC-ND 4.0.

In the SEM image reported in Figure 2.4.3a the flakes deposited by electrospray correspond to the darker areas while on the substrate, only Si and O signals are registered. Figures 2.4.3b and c show the elemental analysis maps extrapolated from EDX measurements on the same area, which highlights respectively the presence of phosphorus and oxygen in correspondence of flakes. The EDX spectrum registered on the point X of Figure 2.4.3a shows the P, Si, and S peaks that are related to (i) the electrosprayed structures of 2D POx, (ii) the substrate, and (iii) the DMSO solvent in the proximity of flakes.

Once obtained the information about the composition of the structures by XPS and EDX measurements, the samples were investigated by TEM characterization to understand the crystalline features.

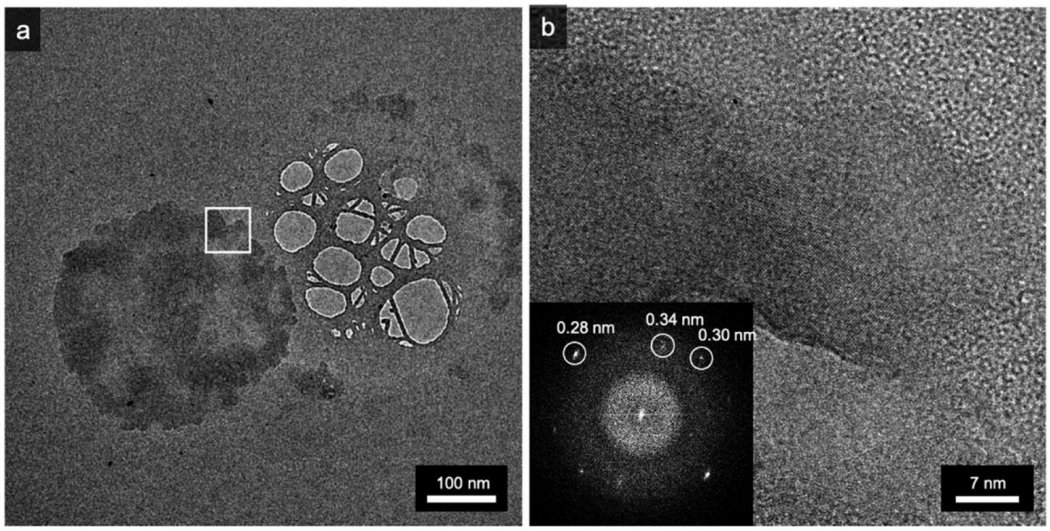

Figure 2.4.4. TEM characterization of electrosprayed 2D PO_x material. (a) TEM image of crystal aggregate over the amorphous carbon film of the TEM grid. (b) HREM image of the area highlighted by the white rectangle in (a), showing lattice fringes of the deposited material; (inset) FFT of the HREM image showing reflections corresponding to planes spaced by 0.34, 0.30, and 0.28 nm, compatible with the P_2O_5 crystal structure. Figure by Moschetto et al. (ref. [129]) is licensed under CC BY-NC-ND 4.0.

In the first analysis, the deposited structures on the amorphous carbon film of the TEM grid presented different morphology with respect to the same material deposited over Si or Si/SiO_2 substrates, showing a regular circular shape with smaller lateral dimensions (Figure 2.4.4a). This is probably due to a nanodroplet of the spray procedure and could reveal that the size and shape of the PO_x flakes deposited through electrospraying are largely dependent on the substrate.

From the magnification of the area in the white rectangle in Figure 2.4.4a, which is obtained by high-resolution electron microscopy (HREM, Figure 2.4.4b), the lattice fringes are visible. The correspondence fast Fourier transform (FFT) shown in the inset contains the periodicities of 0.34, 0.30, and 0.28 nm, compatible with the crystal structure of P_2O_5 found in the literature, namely, (120) 0.335 nm, (211) 0.305 nm, and (220) 0.283 nm. These values confirm the composition found by XPS spectroscopy.

In order to find the piezo-responsive behaviour expected from the theorical calculations, the deposited 2D P_2O_5 flakes were investigated by piezoresponse force microscopy (PFM). This technique probes the mechanical deformation of the investigated material in response of the applied bias between the AFM tip and the sample, opportunely deposited on a conductive substrate. More in detail, the applied voltage is $V_{ext} = V_{dc} + V_{ac} \times \cos(\omega t)$, where V_{dc} is an optional dc offset and V_{ac} is the amplitude of the alternated voltage with angular frequency ω. The PFM can track both in-plane and out-of-plane components of

the material response to the electric field at modulated frequency by lock-in detection. Evidently, the electro-mechanically active materials exhibit a nonzero amplitude PFM signal when an external field is applied.

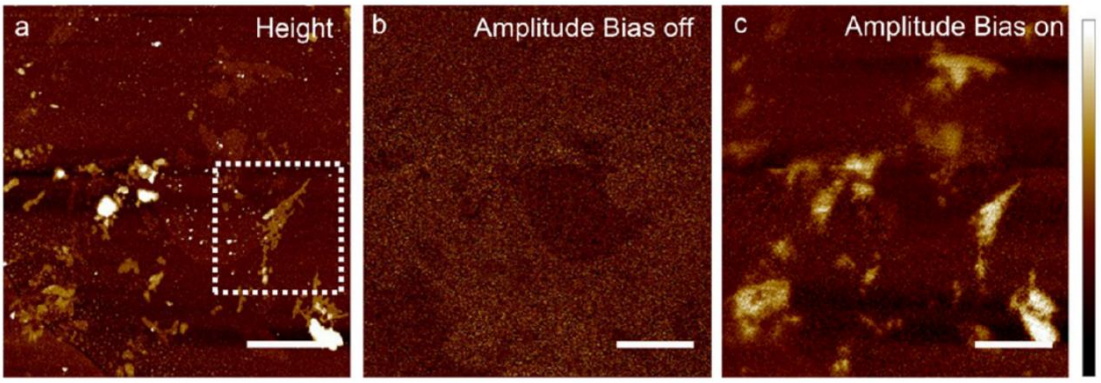

Figure 2.4.5. AFM topographic image and the corresponding PFM image at bias voltages 0 V(b) and 5 V (c). Scale bar: 3 μm. Vertical scales: (a) −12−20 nm; (b, c) −17−30 pm. Figure by Moschetto et al. (ref. [129]) is licensed under CC BY-NC-ND 4.0.

Figure 2.4.5a shows the typical height signal of the electrosprayed structures. In the corresponding out-of-plane amplitude images, the mechanical response of the material is clearly visible when the tip-sample bias is applied (Figure 2.4.5c), if the collected image is compared with the one in which the bias is switched off (Figure 2.4.5b).

Through a deep analysis of the flake signed in Figure 2.4.5a (white rectangle), is possible to understand the behavior of the P_2O_5 flakes under electrical field stimulations. The height-image magnification of the under-examination flake is shown in Figure 2.4.6a. The signals relative to the PFM measurements were acquired at Vdc =0, Vac = 5 V, and a frequency of 30 kHz.

As the first consideration, it is evident the good match between all the amplitude and phase images related to the out-of-plane and in-plane signals, thus indicating the presence of both vertical and torsional displacements.

From the phase micrographs appear that the out-of-plane dipoles are sensitive to the direction of the applied field, showing the flakes dark when the positive bias is applied to

the tip and the sample is grounded (Figure 2.4.6c), and the flake bright when the bias is inverted of 180° (Figure 2.4.6d), indicating a clear out-of-phase response.

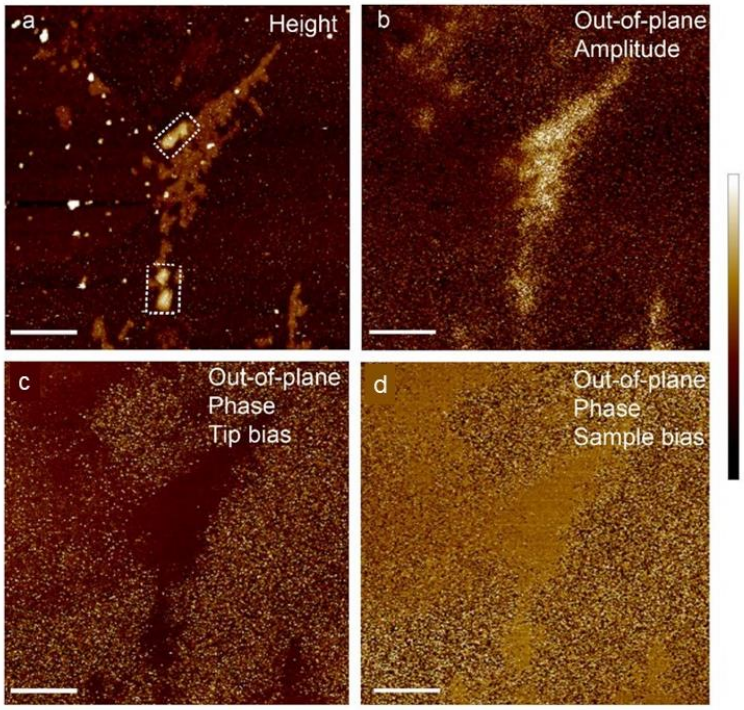

Figure 2.4.6. Piezoresponse force microscopy (PFM) micrographs of P_2O_5 flakes. a) Height image, vertical scale: -8 nm-20 nm. b) Piezoresponse out-of-plane amplitude, vertical scale -20-40pm. c-d) Piezoresponse out-of-plane phase shift. In c (d) a voltage bias is applied to the tip (sample). Scale bars: 1 μm. Figure by Moschetto et al. (ref. [129]) is licensed under CC BY-NC-ND 4.0.

The value of out-of-plane amplitude, 4-5 pm/V, was extrapolated from the out-of-plane amplitude image (Figure 2.4.6b) and is in line with the theoretical values reported in the literature for the phosphorene oxides.[132]

Moreover, the out-of-plane amplitude intensity increases with the increase of the thickness of the P_2O_5 flakes, as shown in Figure 2.4.7. This result confirms the behavior previously reported for some materials as selenides and sulfides,[141,142] and is ascribable to the nonuniform electric field distribution in the tip-sample system, especially for materials with low electrical permittivity.[143,144]

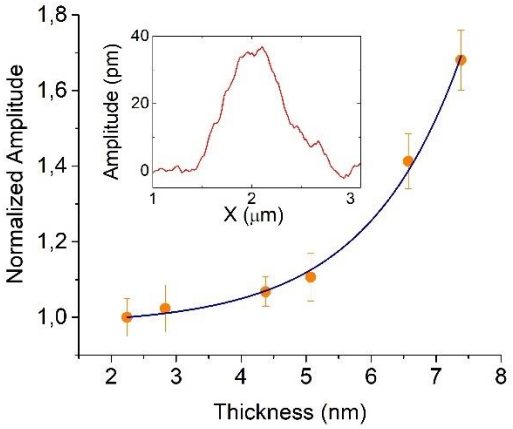

Figure 2.4.7. Maximum out-of-plane amplitude intensity vs flake thickness (black dots). The line is a guide to the eye. Inset: Typical out-of-plane amplitude profile. Figure by Moschetto et al. (ref. [129]) is licensed under CC BY-NC-ND 4.0.

In conclusion, the deposition of 2D P_2O_5 through electrospray has overcome some limitations related to the 2D bP use, allowing to obtain flakes with very high average lateral dimension (hundreds of μm^2) than the 2D bP flakes obtained by mechanical and liquid exfoliation (tens of μm^2). The atomically flat flakes revealed also high stability in terms of degradation and high mechanical fragility if compared with the 2D bP one.

Over the improved stability and the large-scale deposition of the flakes, for the first time ever, it was experimentally demonstrated the electro-responsive behavior of the phosphorene oxides, which showed both in-plane signal (tenths of picometers per V) and out-of-plane signal (some picometers per V) when subjected to an external electric field, confirming the theoretical calculations present in the literature.

Overall, the herein proposed deposition process could enable 2D bP to the real applicability of phosphorus-based 2D nanomaterials for sensing and various classes of energy-harvesting devices.

2.5 Conclusions

In this first part of thesis are described several possible routes to improve the environmental stability and the processability of 2D bP, simultaneously adding new functionalities for extending the spectrum of possible real-setting applications of this emerging class of materials. In this context, it is notable how multiple and different chemical-physical methodologies designed to realize 2D bP-based heterostructures such as vdW coupling with organic molecules, decoration with metal nanoparticles rather than

electrospray-based surface oxidation, may concur to increase the chemical and structural stability in environmental conditions of the as-produced 2D bP-systems. In particular, as the first approach, the stability in air, and the morphological and electrical characteristics of a vdW epitaxial system based on 2D bP coated with tetracosane (C24), are studied. Starting from a model system composed of a monolayer of C24 on a bulk bP crystal, high-resolution AFM revealed a high coverage of the bP surface with epitaxial domains of C24 over areas with lateral size greater than 1 μm^2. Then, the system of interest, as well as the focus of the study, was realized by coating with C24 mono- and multi-layers the mechanically exfoliated 2D bP. The ordering direction of the C24 molecules was the same as in the model system, and it extended from the interface along the multilayer thickness (2 nm), showing excellent protection against the oxidation of 2D bP in air. In fact, the epitaxial C24 multilayers delay the oxidation process by 18 hours, compared to 1 hour for bare 2D bP. Finally, thanks to the EFM it was possible to reveal the modulation of 2D bP polarizability as the effect of the C24 coating, which behaves as an electrical insulator as well as a protecting agent against oxidation. The implementation of functional groups on the linear alkane backbone would allow obtaining a high-performing nanodielectric layer, laying the groundwork to realize MIS structures for micro- and nanoelectronic, photonic and optoelectronic applications.

Because of the distinctive appeal highlighted between phosphorene and organic molecules, a second heterostructure based on the noncovalent interaction between 2D bP and pyrene derivatives, which have permitted to stabilize and, simultaneously add photonic properties to the system, is studied. Indeed, 2D bP terminated with pyrene derivatives forms heterostructures stable in air for more than 6 months. In addition, time-resolved fluorescence emission has revealed relevant modulation of the fluorescence decay time constants of the heterostructures, indicating a possible implementation as active materials in a fluorescent chemosensor for oxygen detection.

An inorganic approach also is provided to realize heterostructures 2D bP-based for improved performance in the catalysis field. Notably, is designed and studied a heterostructure based on 2D bP and Au nanoparticles. It is noteworthy that the Au NPs in-situ formation process through a solid-liquid heterogeneous reaction is functional to (i) fully preserve 2D bP crystalline structure thanks to the soft-pairing/coordination between P atoms of 2D bP surface and Au atoms of the Au NPs, as confirmed by Raman spectroscopy, and (ii) eliminate the use of stabilizer, essential in the synthesis process of Au NPs, allowing an overall deeper understanding of the interface in the heterostructures

based on 2D bP/Au NPs already used in sensing and photonic applications.[145,146] In addition, a partial charge transfer at the 2D bP/Au interface occurs, with a positive charge being localized on the Au atoms directly bonded to 2D bP, as predicted by calculations and confirmed by XPS experiments, paving the way for future "stabilizer-free" 2D bP/Au NPs heterostructures with improved performances in electro-, -photo or photoelectron-chemical catalysis.

Although the proposed approach to create functional heterostructures has proved to be efficient, the scalability issues linked to the effective 2D bP mass produced are not enabling the real applicability of 2D bP-based nanomaterial. Consequently, a new deposition technique of air-stable phosphorus oxide-based nanomaterial, based on the electrospray process, is developed. The produced 2D flakes, specifically 2D P_2O_5 nanoflakes as confirmed by XPS, SEM-EDX, and HRTEM analyses, have an average lateral size of hundreds of μm^2, which is much larger than the average lateral size of 2D bP flakes obtained with standard techniques such as mechanical and liquid-phase exfoliation of bP (tens of μm^2). Together with the lateral dimension enhancement, 2D P_2O_5 flakes showed clear electromechanical responsivity, as predicted in the literature and confirmed by those PFM measurements. In summary, this approach gives important results in view of the 2D bP usability in real life, through which are obtained large-area electromechanical responsive 2D P_2O_5 flakes that can be appealing in the sensing and energy-harvesting fields.

In conclusion, considering that effective placement of functionalized 2D bP-based systems into the electronic consumables mass-market will require a concerted effort in combining wafer scale growth with extremely fine control on the density of functional sites and defects, the introduction of specifically engineered heterostructures proposed in this thesis, can be considered as a smart approach for proving strong control of the interfaces and introducing innovative vertical stacking in multifunctional devices based on 2D bP systems.

Chapter 3

Heterostructures in light-emitting devices

Inorganic materials are very attractive for their outstanding semiconducting characteristics. However, their employment in electronics and optoelectronics is not always trivial as occurring for phosphorene described in the first part of this thesis, that was showed challenges in terms of device fabrication and development due to chemical stability limitations and limited large-scale production in terms produced quantities of 2D bP.[147]

In general, most of the present-day devices use inorganic crystalline materials, which are dominant in electronic devices such as MOSFET,[44,148,149] CMOS[43] as well as high-performing photodetectors.[45–48] The technologically advanced devices based on inorganic materials take advantage largely of the crystalline nature of the deposited inorganic materials, which are grown epitaxially. However, the deposition process is limiting and expensive to obtain a relatively large and defect-free crystalline area..[150] In addition, due to their intrinsic nature, inorganic materials result unsuitable for flexible devices development.[151]

In this context, the realization of systems based on organic materials, i.e., organic semiconductors (OSCs) and functional materials, represent a valid alternative for electronic and optoelectronic applications because of their attitude to maintain the concept of order typical of inorganic counterpart. In addition, when their structure is properly tailored, can arise a nearly unlimited number of OSCs with multifunctional features. Since organic molecules consist of molecular structures with saturated electronic system, the number of intrinsic defects is lower than that of inorganic amorphous semiconductors, which have a large number of dangling bonds. Moreover, in a molecular solid the molecules are held together by weak Van der Waals forces, which decrease as $1/R^6$, where R is the intermolecular spacing. In contrast, the inorganic semiconductors are covalently bonded and strength falls off as $1/R^2$. Accordingly, inorganic materials are hard, brittle, and robust against environmental agents, such as corrosive reagents,

plasmas, and moisture used in the fabrication process of devices, while organic electronic materials are soft and flexible[152] but vulnerable to water vapor and oxygen.[153–155]

If on one hand, the mentioned properties seem to bring to light the fragility of organic materials, on the other hand, they have opened the door to innovative, low-cost and large-scale fabrication methods such as solution-based processes, vacuum sublimation, and other cost-effective techniques.[53–55,156] Accordingly, organic molecules can be deposited on virtually any substrates, including low-cost ones such as flexible plastic, metal foils, and glass.

By focusing the attention on the optoelectronic applications, organic materials have unique chemical physical advantages if compared with inorganic semiconductors. For example, the fluorescence peak of many dyes is strongly red-shifted with respect to the absorption one, resulting in almost no reabsorption losses in organic light-emitting diodes (OLEDs).[157] This characteristic, in conjunction with the low indices of refraction, help to circumvents one of the key problems of inorganic LEDs such as self-heating effect.[158]

In addition, thanks to the extremely high absorption coefficients of some organic dyes in the visible range it is possible to obtain photodetectors and photovoltaic cells using very thin films of organic materials.[159,160]

Nowadays, organic semiconductors are clearly visible in real-life applications thanks to the diffusion of the well-known organic light-emitting diodes (OLEDs) and to their large employment in displays. The substitution of conventional displays in favor of this technology is justified by low power consumption, lightweight but also high brightness, high luminous efficiency, fast response time, etc.

In general, the OLED is a nanometer-thick device capable of generating light when a bias is applied to its two electrodes. The light is generated from an organic light-emitting layer sandwiched between two electrodes and, as a result, light has to pass through one of these electrical contacts (Figure 3.1). However, in this vertical structure, limitations to the device performance originate from the limited electrode transparency, exciton quenching at the electrodes, optical cavity effects, etc.[161]

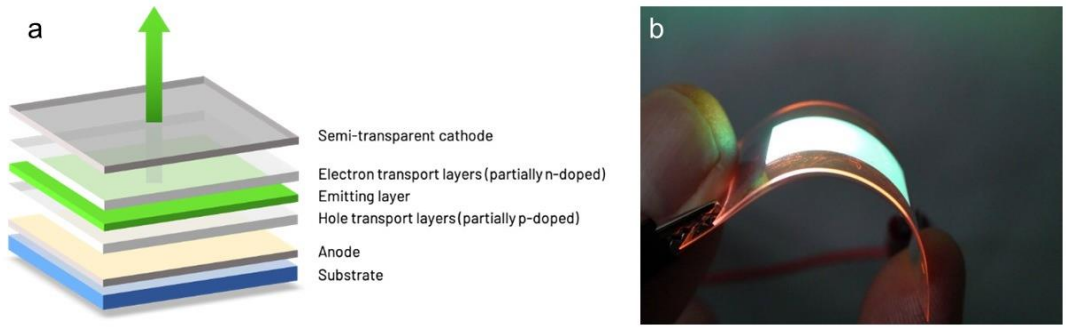

Figure 3.1 a) Schematic structure of OLED; b) OLED technology on flexible support. Figure a by Credoxys GmbH, 2021, https://www.credoxys.com/application/oled/.

To overcome these limitations, an innovative device architecture is hereafter discussed. The new architecture involves the use of a field-effect transistor to generate light from a nanometer-thick device, that is respectively named as organic light-emitting transistor (OLET). This structure has gained increasing attention from the scientific community in reason to the integrated functionalities of logical switching of the transistor with the light-emitting of the OLED in a planar structure in which the light is emitted far from the metal electrodes of the device.[162–164]

In addition, the structure of OLETs represents a key-enabling characteristic to (i) integrate devices with advanced characteristics in more complex systems exploiting multiple functions thanks to its planar structure; (ii) reduce the need of a driving circuitry in the case of display applications and (iii) simplify the manufacturing process towards a cost-effective production with respect to OLEDs.

The OLET structure is composed of a metal-insulator-semiconductor (MIS) stack, respectively gate, dielectric, and semiconductor, which is the basis for the field-effect operation that regulates the movement of the charges within the transistor channel. Additional layers can be deposited onto the MIS structure to favor the process of light emission and/or the electrical ambipolarity.

Over the mentioned advantages in fact, in ambipolar conditions (more details can be found in section 3.1.1) the device structure enables the recombination of opposite charges to occur on the same plane (Figure 3.2a), thus forming excitons and emitting a stripe of light as large as a few tens of micrometers. Therefore, OLETs show the outstanding characteristics to be intrinsically micrometer light sources.

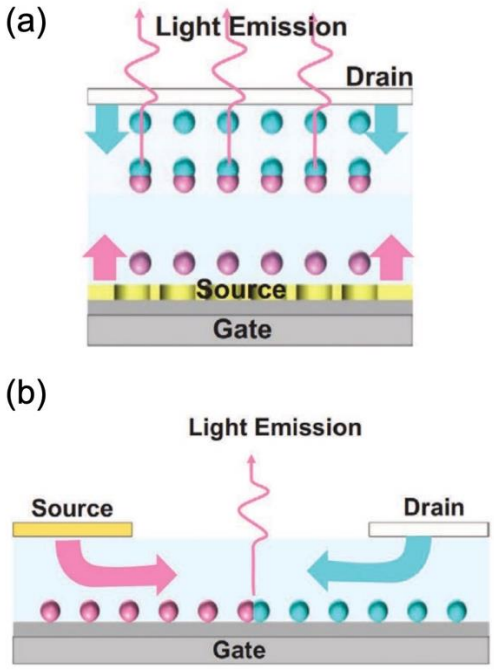

Figure 3.2. Schematic representation of the device structure and operation of a) OLET: charge recombination occurs in-plane within the transistor channel; b) OLED: electrons and holes move vertically across the organic layers and pass through the anode. Figure by Gao et al. (Adv. Mater. 2022, 34, 2108795) is licensed under CC BY-NC-ND 4.0.

Moreover, the flow of electrons and holes, and hence the region of charge recombination and light emission, can be tuned in the lateral direction across the transistor channel by simply playing on the operational driving parameters, resulting in enhanced external quantum efficiency (EQE). EQE describes the number of outcoupled photons per injected charges in the device and it is one of the most important figures of merit to characterize the optoelectronic operation.

Due to the different bias driving scheme and the architecture with respect to the OLED (Figure 3.2b), OLETs represent an ideal structure to improve the efficiency and the lifetime of organic light-emitting devices. In particular, the excitation quenching phenomena, which are of increasing importance when devices are driven under high-injection conditions for high-brightness emission, are essentially due to (i) interaction with the metal contacts, (ii) interaction with the external applied electric field, and (iii) interaction with charges.

In addition to that, the emission of light under ambipolar operation allows excitons to be generated far from the electrodes thus reducing quenching phenomena if compared to the OLED structure (Figures 3.2a and b).

Typically, a reduction of the optical efficiency is observed in OLEDs due to the excitation quenching by interaction with the high electric field applied to the devices, potentially exceeding 10^8 V/cm.[165,166] In contrast, the electric field intensity in OLETs remains below 10^6 V/cm also for a gate bias up to 100V, because of the dielectric thickness (typically around 500 nm) and the planar intralayer charge transport.

Relevant differences between the two structures are noticed also when considering the exciton-charge quenching phenomena, which usually occurs via Förster transfer (dipole-dipole interaction) from an excited neutral molecule to a charged molecule that consequently dissipates the excitation energy nonradiatively. If considering that the charge density in OLEDs is typically about 10^{15} cm^{-3}, the resulting charge-charge distance is on the order of about 100 nm, which is negligible with respect to the diffusion length of the excitons that is in the range of tens of nanometers.[167,168] On the contrary, in OFET devices the charge density can reach values up to 10^{14} cm^{-3},[169] corresponding to a distance of 1 nm among charges and then compatible with the diffusion length of excitons[91] and prone to exciton-charge quenching.

Nevertheless, a quantum efficiency decrease is not observed experimentally in a polymer OLET driven at a current density of 50 A/cm^2.[170] It is noteworthy that in a conventional OLED the current density is on the order of 1-10 A/cm^2 at the point of maximum efficiency.

Moreover, the extreme spatial localization of charge carriers in OLETs, coupled with a third electrode that can balance electron and hole currents, can further favor an effective dissociation between the populations of charge carriers and excitons, resulting in another advantage of OLETs.

Overall, in OLEDs the charge carrier currents that converge in the emission layer form the excitons in it, but spatially coexist with the excitons, making this structure subject to significant exciton-polaron quenching.[171–174]

In this context, the aim of OLET development is to overcome the deleterious photon losses and excitons quenching phenomena occurring in OLED architecture and to exploit its geometry enabling their use in more integrated systems for optoelectronic applications. In this second part of the thesis, two types of OLETs that guarantee an ambipolar operation will be exhaustively exanimated, i.e. the single-layer and the trilayer device architecture.

In the following paragraphs (3.1) the working principle of OLETs are discussed, with particular attention to the most important building blocks and factors with respect to the

device performances such as the dielectric layer, semiconductor and emissive layers, orientation and disorder of organic molecules, and charge injection process. An introductive discussion on the ambipolar conditions is also provided together with the essential requirements for an OLET realization. In paragraph (3.2) it is discussed a device based on a multifunctional layer capable to transport both holes and electrons and to emit light, i.e. the single-layer ambipolar OLET. Alternatively, in paragraph (3.3) an in-depth analysis focuses on a multilayer device that is composed of an emission layer sandwiched between two semiconducting layers which are respectively devoted to transport holes and electrons, i.e. the trilayer OLET.

3.1 Working principles of OLETs

Electrical characteristics

As mentioned in the introduction, by virtue of the technological peculiarities that make them very attractive, this second part of the thesis is focused on OLETs.

OLETs can be described, in a preliminary and simplified view, as thin film transistors endowed with emissive characteristics. A description of the architecture and the field-effect behavior of organic field-effect transistors (OFETs) will be hereafter provided to introduce the more in-depth discussion on the OLET operation.

The field effect transistor is a three-terminals device: *source*, *drain*, and *gate*. Overall, depending on the configuration of the electrodes, it is possible to distinguish between *top gate/top contacts, bottom gate/top contacts, top gate/bottom contact, and bottom gate/bottom contacts* (Figure 3.1.1) even if, over the years, several advanced geometries have been developed to enhance the OLET performance.[175–178]

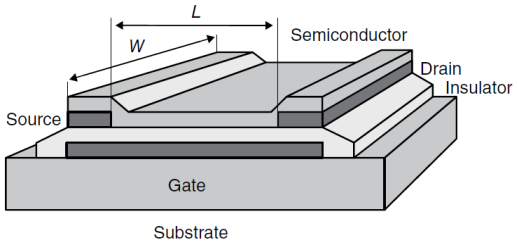

Figure 3.1.1. Bottom gate/bottom contacts representation of an organic thin film transistor in which the channel length (L) and the channel width (W) are indicated. Reproduced with permission from M. Muccini, S. Toffanin, Organic Light-Emitting Transistors: Towards the Next Generation Display, Wiley, New Jersey, 2016.

The organic active layer is comprised between the source and drain electrodes. This distance is defined as the length L of the transistor channel, while the transverse

dimension of the structure is the channel width W. Both these geometrical sizes are important structure parameters for the overall function of the device.

The third electrode, the gate, is placed under the organic semiconducting layer and is separated from it by a thin insulating film, thus forming a metal-insulator-semiconductor (MIS) structure.[179,180]

In general, the behavior of the charges in the channel is regulated by two independent perpendicular electrical fields, obtained by applying one bias between the source and gate electrodes (V_{gs}) and another one between the drain and source electrodes (V_{ds}), Figure 3.1.2a). In a unipolar device only one type of charge carrier (electrons or holes) is transported across the transistor channel and in this type of operation the source electrode acts as a charge injecting contact and the drain electrode acts as the charge collecting one. When the organic semiconductor is ambipolar, that means that the semiconducting thin film provides an efficient transport of both types of charge carrier, source and drain electrodes similarly act as injecting/collecting electrodes.

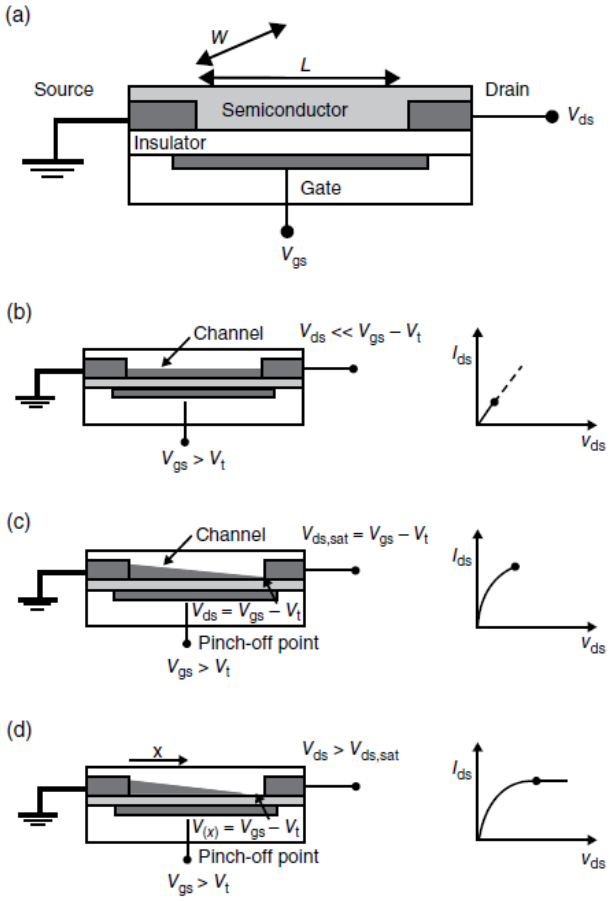

Figure 3.1.2. Schematic representation of a (a) field-effect transistor in (b) linear regime; (c) start of saturation regime at pinch-off, and (d) saturation regime. Reproduced with permission from M. Muccini, S. Toffanin, Organic Light-Emitting Transistors: Towards the Next Generation Display, Wiley, New Jersey, 2016.

For the sake of clarity, a material is considered as a hole (electron) transporter when its ionization energy (electron affinity) closely matches the Fermi level of the electrode material,[181] which is defined as the highest energy level that an electron can occupy at the absolute zero temperature.[182] Together with the energy levels, there are other relevant factors that regulate the charge transport in OSCs, as will be discussed after.

Figure 3.1.2b-d illustrates the basic operation regimes for an n-type OFET, where the OSC is capable to transport only electrons. A positive gate bias V_{gs} is applied in order to induce negative charges (electrons) at the interface between the insulator and the organic semiconductor. Obviously, when the semiconductor transports holes (p-type), a negative V_{gs} bias is applied to accumulate positive charges (holes).

The number of charges accumulated in the semiconductor layer is proportional to the applied V_{gs} and to the capacitance C_i of the insulator. However, not all the charges induced within the semiconductor are free to move in it and contribute to the current in a FET. In a real device, there are traps (see the previous section) to be filled before the additionally induced charges can be mobile. Hence, before the applied gate voltage became effective, there is a threshold voltage V_t to reach to fill the traps. Therefore, the effective applied gate voltage will be given by the value $V_{gs} – V_t$.

The operation regimes of the OFET are essentially three and can be resumed as *linear regime*, the start of saturation regime (*pinch-off* effect), and *saturation regime*.

When no source-drain bias is applied, the charge-carrier concentration (in this case electrons) within the transistor channel is uniform. Applying a small potential between source and drain electrodes, a linear gradient of charge density is formed in the channel (Figure 3.1.2b, $V_{ds} << V_{gs}$). In these conditions, the current flowing through the channel is directly proportional to V_{ds} voltage and the OFET works in linear regime.

By increasing the V_{ds} voltage, a potential value where $V_{ds} = V_{gs}-V_t$ will be reached. At this point, in the region close to the drain electrode, a charge density depletion zone will occur because the gate voltage does not exceed the V_t value. This effect is called pinch-off. In this region, the carriers are swept from the pinch-off point to the drain as the effect of the comparatively high electric field in the depletion region, resulting in a space-charge-limited saturation current $I_{ds,sat}$ flowing across this narrow depletion zone (Figure 3.1.2c).

The further increase of V_{ds} does not lead to an increased I_{ds} current as an expansion of the depletion zone is caused and hence a shortening of the channel occurs (Figure 3.1.2d).

The I_{ds} current will remain constant at $I_{ds,sat}$ value because the potential at the pinch-off point remains V_{gs}-V_t and thus the potential drop between the source and that point is constant. In these conditions, the OFET is working in saturation regime.

To ensure the appropriate charge distribution with respect to the one created by source-drain voltage, the dielectric thickness must be one order of magnitude higher than the channel length.[183] On contrary, the gate voltage will not be able to create the pinch-off condition and then the "on" or "off" state of the transistor.[184,185]

The characteristic curves of an OFET are essentially three: (i) the *transfer curve* (Figure 3.1.3a), where the gate voltage V_{gs} is varied at a constant drain voltage V_{ds}; (ii) the *output curve* (Figure 3.1.3b), where the drain voltage V_{ds} is varied keeping constant the gate bias V_{gs}; (iii) the *locus curve*, where both V_{ds} and V_{gs} potentials are varied simultaneously keeping the same value.

In linear regime, when $V_{ds} << V_{gs}$ and the drain current I_{ds} is directly proportional to V_{gs} bias, the current I_{ds} expression can be described by the equation:

$$I_{ds} = \left(\frac{W}{L}\right) W \mu C_i \left[\left(V_{gs} - V_t\right) V_{ds}\right]$$

where W and L are geometrical parameters, width and length of the channel, respectively; μ is the charge mobility, and C_i is the capacitance per unit area of the gate dielectric.

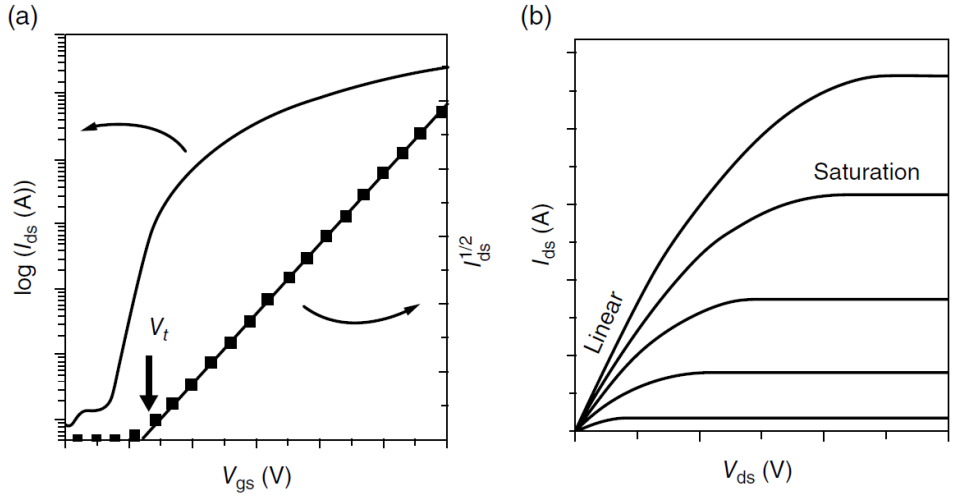

Figure 3.1.3. Characteristic voltage-current curves of an OFET device. (a) transfer curve, with indicated Vt as threshold potential, and (b) output curves in linear and saturation regimes. Reproduced with permission from M. Muccini, S. Toffanin, Organic Light-Emitting Transistors: Towards the Next Generation Display, Wiley, New Jersey, 2016.

The charge mobility can be thus extrapolated from the transfer curve in linear regime as the gradient of the I_{ds} curve.

Since in saturation regime $V_{ds} = V_{gs} - V_t$, substituting this value to the previous equation it is possible to obtain the I_{ds} equation for the saturation regime:

$$I_{\text{ds, sat}} = \left(\frac{W}{2L}\right)\mu C_i \left(V_{\text{gs}} - V_t\right)^2$$

In this regime, the square root of the drain current is directly proportional to the V_{gs} potential, and its gradient is proportional to the mobility. In addition, extrapolating the linear fit to zero obtained the V_t value.

After the description of the basic working principles and the operation regimes of an OFET device, a detailed analysis of the photophysical processes and the composing layers of an OLET is below described.

Electroluminescence

The generation of light by electrical excitation is defined as electroluminescence and was reported for the first time in an organic semiconductor in 1960s, for an anthracene single crystal.[186,187] The process of electroluminescence requires the injection of electrons from one electrode and holes from the other, the capture of the electron-hole pair (exciton), and the radiative decay of the excited exciton state produced by this recombination process.

Generally, the excitons in conjugated systems are considered to be more strongly localized than excitons in three-dimensional semiconductors because they are substantially confined to a single π-chain. In van der Waals solids the fundamental excitons are Frenkel excitons,[188] which are characterized by a very small radius of the electron-hole pair (< 5 Å) because of their strong binding energy (~1 eV).

The exciton is generated by the injection of hole and electron in the device through the relative electrodes. Then, a crucial process occurs in view of the optoelectronic device realization, that is the exciton migration process. Since exciton is a quasi-particle, it is characterized by a wave-like motion. Immediately after exciton creation, the phases of the work functions of all excited molecules have a unique defined relationship to each other. If the phases are maintained during the excitation migration, the exciton moves as a wave and it is said to be coherent. Conversely, the coherence can be lost by interaction with phonons (lattice modes) and/or crystal defects.

For time greater than the coherence time, the exciton can be described as a localized excitation undergoing a random hopping-like motion. During the hopping movement,

excitons can experience sites with an energy lower than the exciton band edge. In this case, if the thermal energy is not sufficient to promote the hopping, the exciton is trapped.

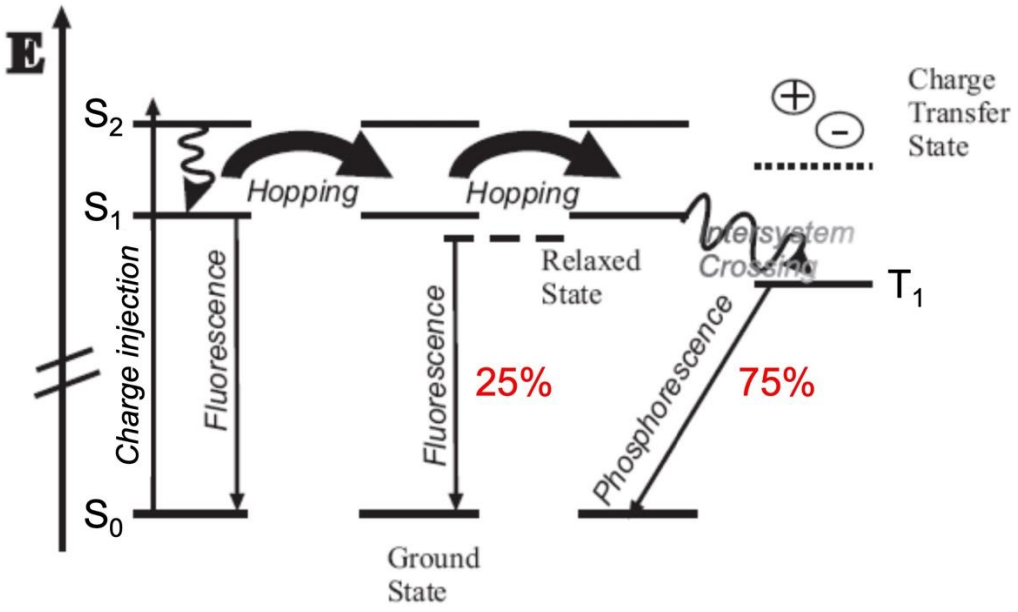

Figure 3.1.4. Jablonski diagram for charge injection, fluorescence, and phosphorescence in a molecular solid. The charge injection process leads to excited singlet (S1) and triplet (T1) states with percentages of 25 and 75%, corresponding to 1:3 ratio, respectively. Thick bend arrows show the exciton hopping between adjacent molecular sites. Non-radiative processes (internal conversion and intersystem crossing) are represented by wavy downward arrows. Radiative processes such as fluorescence and phosphorescence are represented by straight downward arrows.

Hence, excitons can relax in many pathways to the fundamental ground state (S0), as it is possible to see from the energy-level diagram (state diagram) for a molecular solid reported in Figure 3.1.4 (the diagram is obtained from atomic orbital (AO) and molecular orbital (MO) theory).[189]

The spin wave function of the exciton can be singlet (S1) or triplet (T1) because of the two spin-½ electronic charges (Figure 3.1.4). As a consequence of the confinement, the energy difference between singlet and triplet (exchange energy) may also be large.[190]

The spin-allowed radiative emission is from singlet only and it is called *fluorescence*. Since the *intersystem crossing* from triplet to singlet is forbidden, then the triplet excitons can decay by an indirect process such as triplet-triplet annihilation, or by *phosphorescence*. Phosphorescence is the radiative deactivation from triplet (T1) to ground singlet (S0) and it is spin forbidden. When *phosphorescence* occurs, the decay lifetime is longer than that of *fluorescence* and then it is preferred in light emitting devices.

In optoelectronic devices both triplet and singlet exciton are created with a ratio of 3:1, respectively. Hence, because there is the generation of 75% of triplet states in which the radiative deactivation (*phosphorescence*) is spin forbidden, high-atomic-number elements are used, as will be described after, with strong spin-orbit coupling to allow the *phosphorescence*.

One of the most important figures of merit in light emitting devices is the external quantum efficiency (EQE), which is the expression to quantify the conversion of the injected charge carries into emitted light. The EQE can be defined as the ratio of the flux of photons per unit area measured outside the device with respect to the flux of carrier per unit area ζ injected into the device:

$$\eta_{ex} = \zeta\, \gamma\, \Phi_{PL}\, \chi\, \sigma_{OUT}$$

where γ is the ratio between the excitons formation events within the device with respect to the number of charges flowing in external circuit, Φ_{PL} is the luminescence quantum yield of the exciton formation layer, χ is the spin multiplicity of the radiatively recombining excitons, and σ_{OUT} is the light outcoupling efficiency from the device into the open space.

Effect of molecular orientation on the optoelectronic characteristics

One of the most affecting factors with respect to the device performance is the orientation of molecules (molecular packing). Indeed, the orientation of molecules has effects on both electrical and optical performances, because it is crucial in the transfer integrals of electrons on one hand, and in the diffusion process of excitons on the other hand.

In general, the organic semiconductors can adopt four different kinds of packing: 1) face-to-edge packing (Figure 3.1.5a), where the molecules are not π-π overlapped between adjacent molecules; herringbone packing (Figure 3.1.5b) with π-π overlap between adjacent molecules; 3) lamellar packing in one-dimension (Figure 3.1.5c) where a π-π stacking of molecules occurs; 4) lamellar packing in two-dimensions (Figure 3.1.5d) with π-π stacking between molecules.

The most effective charge transport occurs when the molecules are packed in 2D lamellar packing since it can transport the charge carriers through an almost straight line.[191]

Moreover, since the most efficient charge transport occurs along the direction of intermolecular π-π stacking, molecules oriented with the long axes parallel to the normal direction of the OFET substrate are preferred to optimize the charge conduction from source to drain.[192]

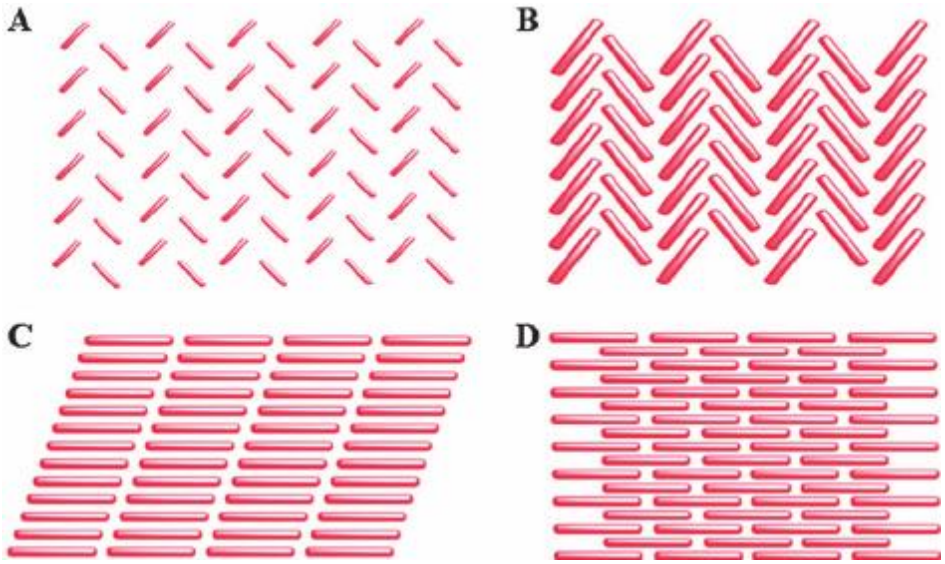

Figure 3.1.5. Molecular packing in organic semiconductor materials. a) face-to-edge packing; b) herringbone packing; c) lamellar packing (1D); d) lamellar packing (2D). Reprinted with permission from Chem. Rev. 2012, 112, 4, 2208–2267.

The herringbone structure is not a priori the most favorable packing for transport because of the large angle between the planes of adjacent molecules along the herringbone diagonal. In this context, several approaches have been followed in order to improve carrier mobilities by theoretically calculating the conjugated backbones in structures where adjacent molecules are cofacial.[193]

Unfortunately, there is actually no clear evidence that an organic semiconductor cofacial-packed can lead to higher mobilities than a herringbone-packed. The reason is that the molecules are never exactly superimposed on top of one another because the electrostatic repulsive terms in a perfect cofacial situation are largest. As a consequence, displacements along the long and/or short molecular axes between adjacent molecules, usually occur.[181] Some theoretical investigations have revealed that such displacements do strongly affect intermolecular couplings. This coupling intimately depends on the bonding-antibonding pattern of the frontier molecular orbitals HOMO (highest occupied molecular orbital) and LUMO (lowest unoccupied molecular orbital,[194] see Appendix A).

These two energy levels are characteristic for any OSC and are of fundamental importance with respect to the charge injection process, where their mismatch with the Fermi level of the metal is crucial.

In molecular solids the *diagonal disorder* and the *off-diagonal disorder* are usually distinguished. The diagonal disorder reflects the fluctuation in site energies, such as

HOMO/LUMO level energies of chain segments or individual molecules. The off-diagonal disorder reflects the strength of the interaction between adjacent molecules or chain segments, such as the modifications of their relative positions and orientations. Off-diagonal disorder can generate conducting pathways through the material as dead-ends for the charge.[181]

In polymer chains, a contribute to diagonal disorder is due to the torsion angles and/or the presence of chemical impurities which can arise different HOMO and LUMO energies as a result of the conjugated segments with different lengths. In the case of flexible molecules/chain, a major contribute to diagonal disorder is conformational freedom, as it leads to a distribution of torsion angle between adjacent moieties.

A further contribute to diagonal disorder is induced by electrostatic/polarization effects of the neighboring molecules, which vary with the fluctuation in local packing. This effect is amplified if the molecule/chain contains local dipole moments.[195]

The fact that the transport is controlled by the degree of order of the molecular solid, has been demonstrated for small molecules by acting on the deposition condition such as the temperature or nature of the substrate, the film thickness, etc.[196,197]

From the optical point of view, the molecular arrangement strongly influences the excitonic energy levels of a molecular solid. The modulation of the parameters of deposition also leads to different degrees of molecular order which impact the optical properties of the film.[198,199]

The substrate on which the film is deposited has a key role. Indeed, it has been demonstrated that using a single crystal substrate[199] it is possible to obtain high degrees of order, which lead to superradiance.[198] Contrarily, when an amorphous substrate is used, the molecules in direct contact with the surface can have aggregation forms very different from the single crystal.[200]

In general, it is possible to assert that the exciton levels and the optical properties of a film will be similar to those of the corresponding single crystal if the film has a crystalline morphology. On contrary, for amorphous films, the optical properties will be similar to those of isolated molecules.[201]

Actually, between these two extremes there are a lot of degrees of morphology that tune the optical properties. A common situation is the coexistence of crystalline and amorphous domains. In this case, the excitons generated in the crystalline domains can diffuse by thermally activated hopping process until finding a site with low energy level, and then can relax. In presence of trapping sites, which increase with the increase of

molecular disorder, the excitons can be entrapped if the thermal energy is not sufficient for de-trapping.

Dielectric layer

The overall performance and crucial process of charge recombination and accumulation do not depend only on the organic active layer, but the dielectric layer and its interface play a fundamental role in the OFET characteristics. Indeed, the roughness and the polarity of the dielectric layer affect the morphology and the molecular arrangements of the overlaying layers, directly impacting the charge mobility and the threshold voltage of the semiconductor layer.[202,203]

The most important parameter of this layer is the dielectric constant *k*, which determines the capacitance $C_i = \varepsilon_0 k / \mathrm{d}$, where ε_0 is the permittivity in vacuum and *d* is the dielectric layer thickness. Hence, in order to achieve a high number of charges within the channel (increments C_i) one can assume that it is possible (i) reduce the thickness of the dielectric layer d; (ii) increase the k constant of the material. The gate dielectrics need to have low gate leakage current and the ability to sustain high voltage without dielectric breakdown, thus the first hypothesis is not recommended. Consequently, it is preferable to use high-k dielectrics material in organic device because they allow to scale down the device dimensions and lower the driving voltage.[204]

The most common dielectric material used as a gate in OFET is SiO_2 (200-400 nm thick) because of its large availability. The presence of hydroxyl groups on the surface induces a large density of traps, which requires surface treatments with hexamethyldisilazane (HMDS) or alkanetrichlorosilanes to create a self-assembled monolayer (SAM) on the surface to reduce traps. This issue combined with the low dielectric constant (k = 3.9), has driven the interest towards other metal oxides with higher k with respect to that of SiO_2, such as Al_2O_3 ($k \approx 8$), TiO_2 ($k \approx 41$), ZrO_2 ($k \approx 25$) etc.[204]

Together with traditional inorganic dielectric materials, polymers have shown properties complementary to those of traditional inorganic materials such as being lightweight and having low-temperature solution processability and mechanical flexibility. Moreover, these dielectric materials often exhibit smooth surfaces because they are amorphous or poorly crystalline, resulting in an ideal surface for depositing organic material and for its growth characteristics. Several of those are reported in an extensive review accessible via the following reference: [205].

The implementation of a high-k dielectric layer dramatically reduces the threshold voltages. For example, an OLET based on a low k dielectric such as PMMA reaches its full-ON state when driven at -100 V. Conversely, when a high-k dielectric is introduced, such as the polymer P(VDF-TRFE-CFE), the same ON state is obtained at -20 V.[206]

Because of their flexibility and the intimate contact nature with the organic semiconductors,[191] the interest on polymeric dielectrics is exponentially increasing.[206–209] In particular, polymethylmetacrylate (PMMA) was implemented as gate dielectric in the OLET devices described in this thesis.

Organic semiconductors

According to the molecular weight, organic semiconductors can be divided into small molecules and polymers. Despite polymers having good solution-processability and being the preferential system for optimizing the emission properties in OLETs, they generally have low field-effect charge mobility due to the amorphous organization at the solid state. In this context, small molecules have exhibited higher mobility values with respect to the polymers because of (i) the defined structures; (ii) the long-range order molecular organization in thin film, essentially due to the deposition by thermal evaporation; (iii) the higher control of the level of purity.

To date, organic semiconductors do not equally support the conduction of electrons and holes, but the majority of them are p-type conducting. In this context, while the mobility record for p-type organic materials is still being reset frequently (43 $cm^2 V^{-1}s^{-1}$ for C8-BTBT),[210] many less n-type small molecules have been reported and the absolute mobility values are still lower when compared with the first one (12.6 $cm^2 V^{-1}s^{-1}$ for F_4-BDOPV).[211]

The problem behind this gap mainly resides in the intermolecular interaction of molecules. When isolated molecules approach each other, the resulting valence bandwidth remains larger than the conduction bandwidth.[212] This is the basic reason that explains why organic materials typically display higher hole mobilities than electron mobilities.

A strategy to increase the electron mobility in OSCs could be the introduction of strong electron-withdrawing groups such as -CN, -Cl, -F, and CF_3. The introduction of these groups leads to an increase of LUMO level energy, and then to molecules not very stable under ambient conditions.[211]

While the most commonly p-type semiconductors used in OLETs are based on linear acenes or oligoacenes and thiophene-based polymers and oligomers, the n-type semiconductors are based on oligothiophenes. Therein, often the molecular energy levels are tuned by substitution with cyano, perfluoroalkyl/aryl, and alkyl/arylcarbonyl, naphthalene and perylene derivatives, phthalocyanine and fullerenes (Figure 3.1.6).

Over the small molecules, are used many polymeric semiconductors such as poly(thiophene-thienothiophene) (PBTTT-C14), poly[2,5-(2-octyldodecyl)-3,6-diketopyrrolopyrrole-alt-5,5-(2,5-di(thien- 2-yl)thieno[3,2-b]thiophene)] (DPP-DTT) (Figure 3.1.6).

Organic emitters

On one hand, the charge mobility is typically favored by the solid-state order of organic molecules. On the other hand, the luminescent properties are generally affected by such strong intermolecular coupling. As a result, some device architectures include two different layers that separately provide electrical and optical characteristics. In this view, traditional organic emitters are used and, according to the spin statistics, singlet and triplet excitons are formed with a ratio of 1:3. Traditional fluorescence emitters cannot utilize triplet excitons to radiatively deactivate, resulting in a loss of 75% of the light which is returned in the form of heat. In order to recover the loss of radiative deactivation, it is possible to use organic metal complexes to break the spin selection rule by spin-orbital coupling.[213] In fact, by using heavy atoms in phosphorescent emitters it is possible to promote the intersystem crossing process (ISC) and utilize triplet state to emit phosphorescence, while the ligands can tune the energy level of the excited states.[214]

Consequently, the obtaining of a phosphorescence emitter is based on a host-guest system, in which Förster and/or Dexter energy transfer processes occur between host and guest, allowing to harvest of both singlet and triplet excitons generated by electrical injection.[215]

To date, numerous **phosphorescent emitters** are used such as tris(2-phenylpyridine)iridium(III) [$Ir(ppy)_3$], and bis(2-methyldibenzo[f,h]quinoxaline)(acetylacetonate) iridium(III) [$Ir(MDQ)_2(acac)$] (Figure 3.1.6).

Other traditional **fluorescent emitters** are tris(8-hydroxyquinoline)aluminum (Alq_3), and 9-(9-phenylcarba- zole-3-yl)-10-(naphthalene-1-yl)anthracene (PCAN), as reported in Figure 3.1.6.

Other strategies were adopted to develop both highly efficient and cost-effective materials, as the materials based on the thermally activated delayed fluorescence such as 2,4,5,6-tetra(9H-carbazol-9-yl) isophthalonitrile (4CzIPN).

This effect is based on the reverse intersystem crossing (RISC) from the triplet excitons to singlet one by thermal activation.[216] The thermally activated delayed fluorescence (TADF) emitter 2,4,5,6-tetra(9H-carbazol-9-yl) isophthalonitrile (4CzIPN) are reported in Figure 3.1.6.

These combinations of the reported emitters have been shown highly efficient in OLET devices.[217–219]

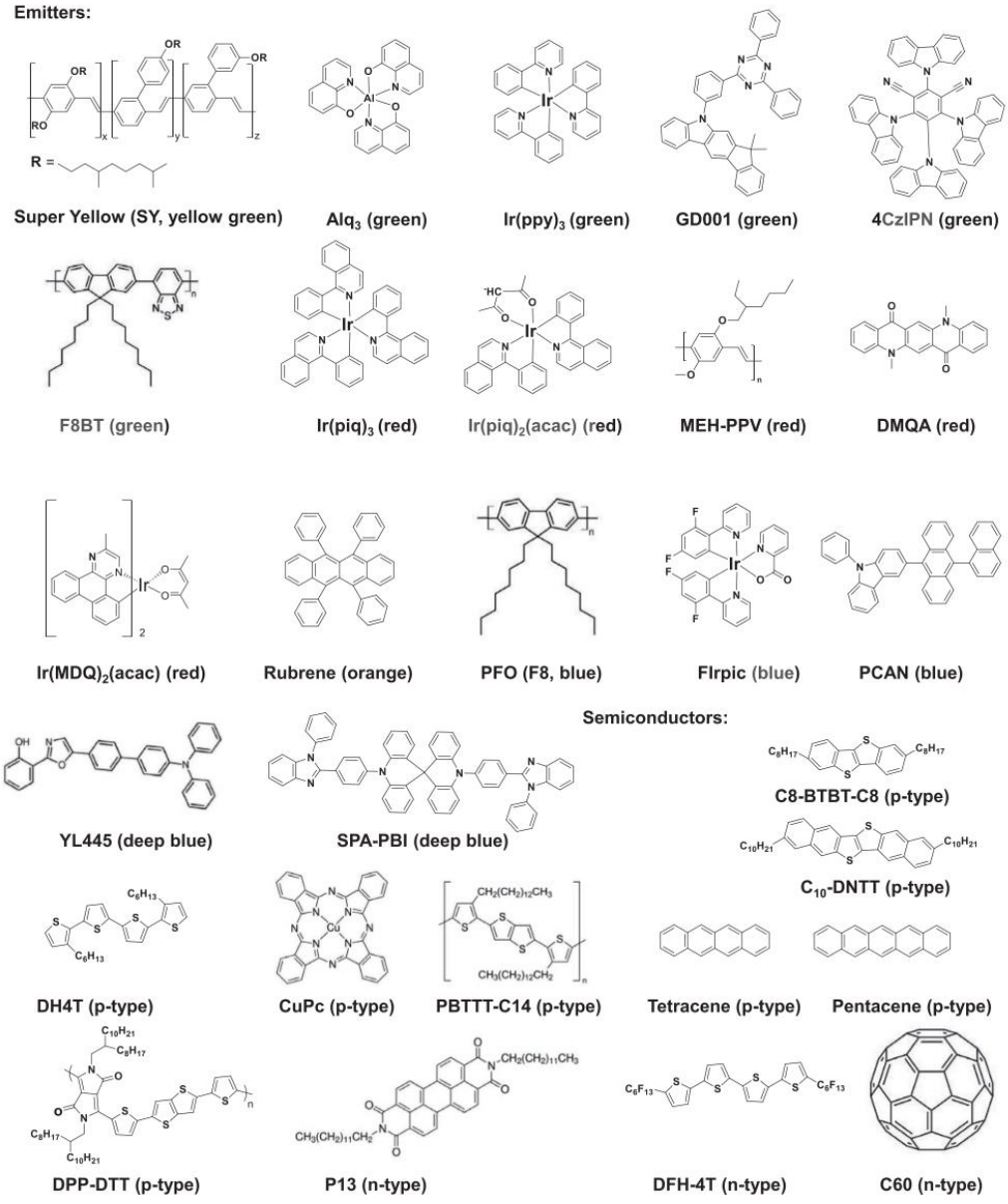

Figure 3.1.6. Chemical structures of organic emitters and semiconductors used in OLETs. Reproduced with permission from Chen et al, Small 2021, 17, 2007661, Wiley.

Polymeric emitters have been also developed such as super yellow (SY), poly(9,9-di-n-octylfluorene-alt-benzothiadiazole) (F8BT), poly[2-methoxy-5-(2′-ethyhexyloxy-1,4-phenylene-vinylene)] (MEH-PPV), and poly[9,9-di(ethylhexyl) fluorene] (PFO). There emitters are widely used because of their processability from solution, good solubility and suitable energy levels.

Charge injection

Before flowing in the semiconductor layer, charges need to be efficiently injected from the electrodes. The interface formed when the organic semiconductor and the metal electrode are in contact, is usually treated as a Mott-Schottky barrier, where the barrier height is given by the difference between the HOMO and the metal work function (WF_m) if holes are injecting (between LUMO and WF_m for electron injection).

Physically, the interface is a region of uncompensated charges where a potential drop occurs. From an energy point of view instead, there is a bending of the energetic levels of semiconductor which forms a gap with the work function of the metal electrode. The higher the energy gap, the less efficient the charge injection process (non-ohmic contacts)[220] and vice versa.

If considering the example shown in Figure 3.1.7, when the metal and the organic semiconductor come in intimate contact, the organic material is in the potential rise of the tail of the metal electron distribution. Thus, both the vacuum levels get aligned in a very narrow interfacial gap.

Since the WF_m is larger than the work function of organic material (Φ), the metal and the organic semiconductor interface is not in equilibrium (Figure 3.1.7a) and some electrons can move through the interface from the organic semiconductor to the metal.

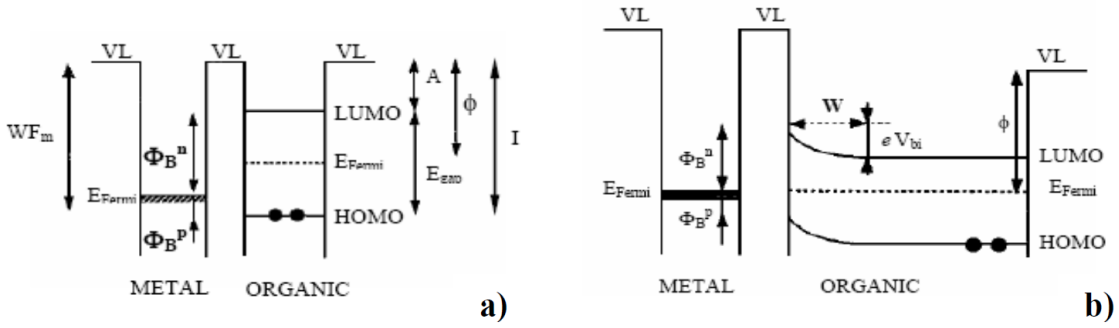

Figure 3.1.7. (a) Schematic representation of an ideal organic semiconductor/metal interface with WF_m metal working function, A organic semiconductor electron affinity, I ionization energy, Egap energy band gap. Φ_B^p and Φ_B^n are the energy injection barrier for holes and electrons respectively and ϕ the work function of the organic material. (b) Energy level band bending at the organic semiconductor/metal interface. A diffusion layer of thickness W compares.

The electron migration into the metal leaves the organic semiconductor positively charged at the interface, generating an overall charge redistribution that hinders further electron movements until both Fermi levels are aligned.

The result is the formation of a diffusion layer (W) by band bending and the generation of an organic layer potential (V_{bi}, Figure 3.1.7).

The classic Schottky-Mott equations for hole and electron injection in simple contacts are described as:

$$\phi_B^p = I - WF_m$$

and

$$\Phi_B^n = WF_m - A = E_{gap} - \phi_B^p$$

where I and A are the organic semiconductor ionization energy and the electron affinity, respectively.

In real cases, the simplistic model discussed above is not effective for the description of the metal/organic semiconductor interface. Often, the generation of an interface dipole can occur that shifts upward the vacuum level of the semiconductor with respect to the metal, worsening the charge injection. The interface dipole generation can be caused by several factors, such as the charge transfer between semiconductor molecules and metal, population of metal-induced mid-gap (creation of new energy levels), or reduction of the metal work function due to adsorption of the organic layer. The potential change of the dipole presence must be taken into account in the calculation of the valence band offset:

$$\phi_B^p = I - WF_m \pm \Delta$$

where Δ represents the interface dipole and the sign on front is chosen to reflect its direction.

The Schottky-Mott model often is not sufficient to describe properly the charge injection into organic semiconductors. Thus, other models such as the thermally assisted tunneling from the metal into the localized states of the semiconductor were proposed.[221]

In general, the most used electrodes are made by metals such as Au (preferred for p-type semiconductors because of its high work function) or Ca (low work function, used for n-type semiconductors). In addition are used also heavily doped silicon, metallic conductive oxides (e.g., Indium Tin Oxide (ITO)), conductive polymers such as

poly(3,4ethylenedioxythiophene) doped with poly(styrene sulfonate) (PEDOT:PSS) and graphene.[191]

A crucial role for the optoelectronic performances in organic light emitting devices is the electron-hole capture process. In order to obtain efficient capture in the in-plane and wide volume of OLETs, it is necessary to guarantee a sufficiently high charge density so that charges of opposite signs can encounter each other within the collisional capture radius.[190]

In order to improve the energy levels alignment as well as the charge density, polymeric and molecular semiconductors, such as the molecular compound named as "bphen", were introduced at the electrode/active layer interface to favor the charge injection process. An in-depth discussion will be provided in the last chapter.

3.1.1. Ambipolar conditions

Some of the advantages described in the introduction while comparing the OLET and OLED devices are closely linked to a fundamental working condition of the transistor, the ambipolarity. When this condition is achieved, both holes and electrons are injected into the channel by the source and drain electrodes, favoring the generation of excitons within it. The light generated in the channel can be spatially modulated by V_{ds} and V_{gs} potentials and this is the main condition to enhance the device efficiency, as the excitons-electrode quenching is reduced and light should not pass through a semi-transparent metal electrode, as occurring in OLED devices.

The behavior of an ambipolar transistor can be mathematically rationalized by coupling of two *noninteracting* unipolar p-type and n-type OFETs. This coupling is defined by the edge conditions of the three contact voltages.

To explain the ambipolar behavior, it is easiest to start from a unipolar transistor where is applied a positive drain voltage V_{ds} and a positive gate voltage of $V_{gs} = V_{ds}$. $V_{t,e}$ and $V_{t,h}$ are the threshold voltages for electrons and holes, respectively.

If (i) the applied V_{ds} voltage is higher than the threshold voltage for electrons ($V_{ds} > V_{t,e}$) and (ii) the gate voltage V_{gs} is more positive than the source electrode, electrons are injected from the source into the accumulation layer and drift toward the drain. In this condition the transistor is working in *unipolar regime.*

By reducing the V_{gs} bias, the gate voltage will be more negative than the drain voltage of a quantity $V_{gs} – V_{ds}$ (Figure 3.1.8a). The V_{gs} reduction leads to the interruption of electron

injection from the source electrode because $V_{gs} < V_{t,e}$. Contrary to what happens in a unipolar device in which these conditions power off the device, the drain electrode in an ambipolar transistor will inject holes into the channel if $V_{gs} - V_{ds} < V_{t,h}$. Hence, if the two conditions on V_{gs} are simultaneously fulfilled, such as $V_{gs} > V_{t,e}$ and $V_{gs} - V_{ds} < V_{t,h}$ (Figure 3.1.8a), both electrons and holes are present in the channel (Figure 3.1.8b).

This regime is called the *ambipolar regime*, in contrast to the unipolar regime, where only charges with only one polarity are present in the channel for any particular biasing conditions.

The characteristic curves obtained in ambipolar devices are different whit respect to the unipolar transistor. In particular, if compared with the transfer curve of the unipolar device (see the previous section), the ambipolar one shows a *v-shape* of the I_{ds} current in a semi-logarithmic graph (Figure 3.1.8c).

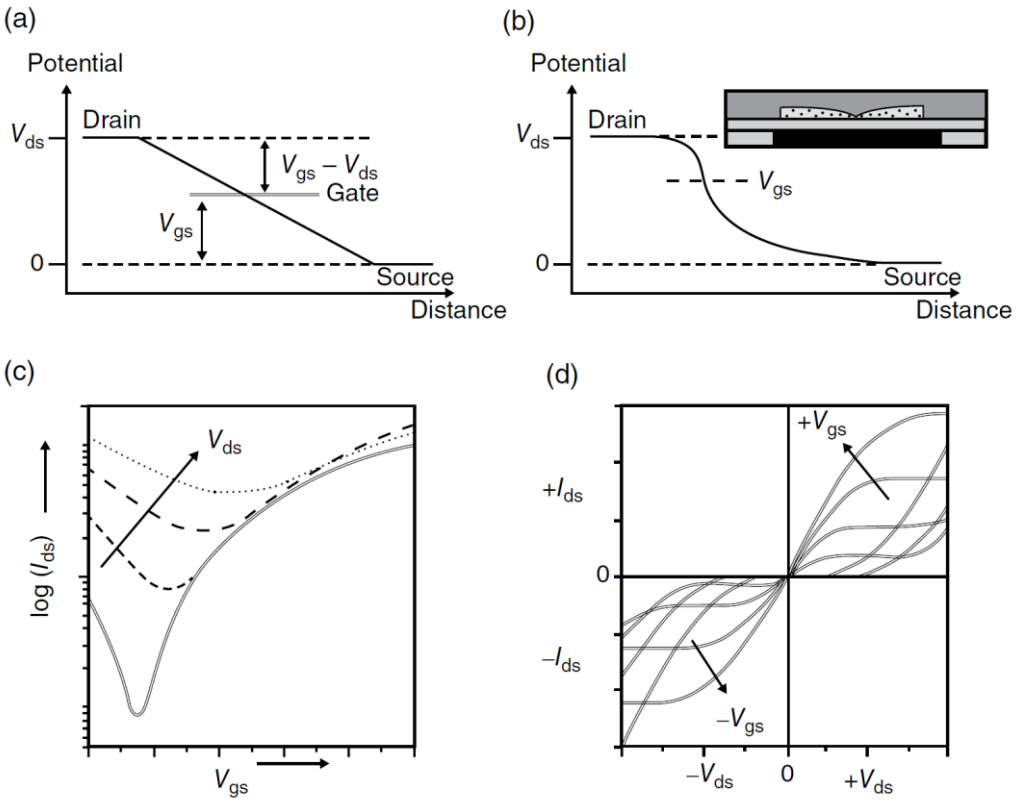

Figure 3.1.8. a) Representation of source, drain, and gate potentials with respect to each other in a field-effect transistor; b) recombination of opposite charge carriers within the transistor channel in ambipolar regime; c) transfer curves in semilog for an ambipolar transistor with equal hole and electron mobilities and slightly different threshold voltages; d) Calculated ambipolar output characteristics for the same transistor for positive (first quadrant) and for negative (third quadrant) Vg and Vds, respectively.

The opposite branches of the I_{ds} current curve represent the flows of the opposite charge carriers (electrons and holes) resulting from the local difference between the applied

voltages at the source, drain and gate electrodes. In the proximity of the edges, the I_{ds} current can be considered as unipolar due to the major contribution of one type of charge carriers, while the minimum of the curve represents the maximum of the ambipolar behavior, when the two charge-carriers currents are totally balanced. Also, the characteristic output curves for ambipolar devices change their trend with respect to the unipolar ones, showing two different phases in reason of the fact that either opposite charges flow in the channel (Figure 3.1.8d). In the first phase, when just one charge carrier is flowing in the channel, the behavior is similar to that of the unipolar device and the I_{ds} current reaches a temporary plateau. Once reached the appropriate local bias that permits the injection of the opposite charge carrier, the I_{ds} output curve raises quadratically.

A simple analytical expression for the ambipolar regime within the graduate channel approximation[222] can be derived. Assuming an infinite recombination rate of holes and electrons in which all the injected charges have to combine within the transistor channel, it is possible to assert that the source-drain current equals the electron and hole current for each channel. Hence, combining the expressions for the saturated currents for the holes and electrons channel, the source-drain current for the ambipolar regime can be written as:

$$|I_{\mathrm{ds}}| = \frac{WC_i}{2L}\left\{\mu_e\left(V_{\mathrm{gs}} - V_{t,e}\right)^2 + \mu_h\left(V_{\mathrm{ds}} - \left(V_{\mathrm{gs}} - V_{t,h}\right)\right)^2\right\}$$

and the position x_0 of the recombination zone within the channel is obtained by

$$x_0 = \frac{L\left(V_{\mathrm{gs}} - V_{t,e}\right)^2}{\left(V_{\mathrm{gs}} - V_{t,e}\right)^2 + \frac{\mu_h}{\mu_e}\left(V_{\mathrm{ds}} - \left(V_{\mathrm{gs}} - V_{t,h}\right)\right)^2}$$

confirming that the position of the light-emitting area (recombination zone) depends on the applied voltages and on the electron- and hole-mobility values.

3.1.2. General overview

After a detailed discussion of the working principles of OLET and the relative materials and processes that can affect its operation, it is possible to resume that ideal OSCs should have (i) high-charge mobility for both electrons and holes, (ii) efficient exciton formation and electroluminescence emission in the solid state and (iii) controlled molecular packing, which is crucial to the former two points. The accurate balancing of electrons and holes,

ensured by a good energy levels alignment between OSCs and metal contacts, enhances electrical properties and then guarantees a spatial tuning of the OLET emission region.

Apart the balance between holes and electrons, the other feature that must be provided by a good OSC candidate for an OLET device is light emission. If the charge mobility is favored by strong intermolecular π-π stacking, the luminescence generally decreases due to the quenching of singlet excitons.[223] Consequently, it is clear that the optimization of the OLET performances is a trade-off between the two processes.

In particular, in paragraph 3.2 a single-layer OLET structure composed of an emissive ambipolar material is discussed. The milestone among the emissive ambipolar materials is poly(9,9-di-n-octylfluorene-alt-benzothiadiazole) (F8BT), a green emitting D–A (electron-donor and electron acceptor, respectively) conjugated polymer with a photoluminescence efficiency of 50–60% in solid films,[224] which has shown in single-layer OLET saturation mobility of 7-9 $cm^2\ V^{-1}s^{-1}$ for both holes and electrons. Despite these interesting properties, the polymeric nature leads to low field-effect charge mobility in the amorphous phase.

Aimed at better control of the morphology of the deposited film, the herein proposed structure is composed of a multifunctional layer, named NT4N, which is deposited by thermal evaporation. Despite the light stripe movement inside the channel, which highlights good ambipolar behavior, the optical power of the single-layer device is resulted low.

Then, it was developed a bilayer structure, discussed in paragraph 3.3. The bilayer structure is composed of a transporting layer of p-type OSC named C8-BTBT, and an emission layer (EML) of host-guest phosphorescent emitter composed of a matrix of Alq3 doped with a near infrared (NIR) (Pt(tpbp)). The aim of this structure is the development of a consolidated basis, in terms of electrical and optical characteristics, to drive the subsequent experiments with the trilayer OLET structure. To now, many bilayer structures have been reported,[225–227] but the unipolar nature of the devices does not allow light emission within the transistor channel.

In addition, in paragraph 3.3 a trilayer structure is presented and discussed. A trilayer structure with high EQE values was already reported.[164] Nevertheless, a comparative study is hereafter reported with the aim of unraveling the interconnected phenomena between charge injection, electron transport and quantum efficiency in this class of devices,. In particular, different n-type OSCs with different characteristics (P13, N-F2-6, DFH-4T) were deposited onto the bilayer structure in order to test the effect of the

intrinsic characteristics such as energy levels, charge transport and morphology on the global performances of the devices. In addition, an electron injection layer was added in order to fill the gap in n-type conduction with respect to the p-type one and then develop more charge-balanced devices.

3.2 Single-layer OLET based on NT4N multifunctional ambipolar semiconductor

As described in the previous section, the accurate balancing of hole and electron mobilities is crucial to guarantee both high external quantum efficiency and spatial tuning of the OLET emission region (Figure 3.2.1).
The integration of several features in a unique material is very challenging, and in literature the systems having these characteristics are not more.

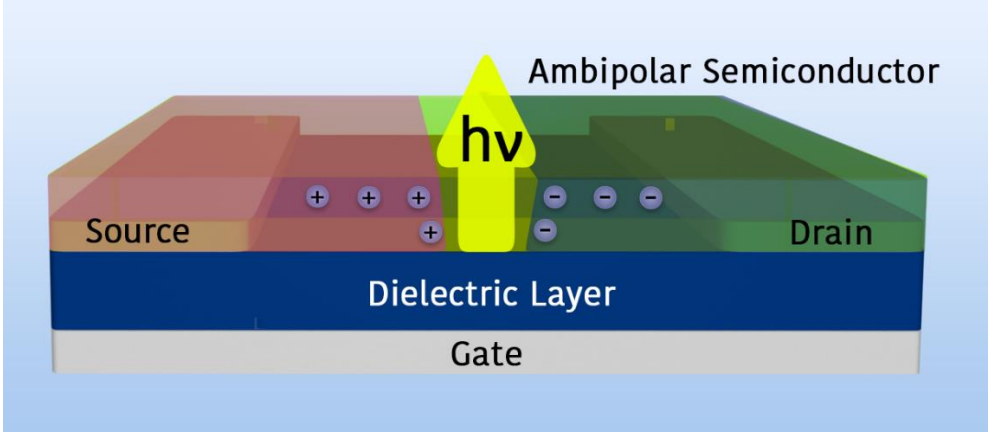

Figure 3.2.1. Schematic representation of a single-layer OLET. In the depicted device, the transport of both electrons and holes, and the light emission are carried out by a single multifunctional organic layer. Figure by Moschetto et al. (J. Mater. Chem. C, 2020, 8, 15048) is licensed under CC BY-NC-ND 4.0.

Other than the mentioned F8BT, the growing research of novel multifunctional materials for highly-integrated systems has paved the way for new strategies of molecular engineering to enhance the coexistence of both processes. One of these is the rigidification of the molecular structure by limiting the torsion angle, the introduction of substituents with inductive or mesomeric effects, the stabilization of the aromatic or the quinoidal resonance form, the increase of the extension of the π conjugation, and the rational conjugation of substituted monomers to induce intermolecular order. Another strategy, one of the most successful, is the synthetization of molecules or copolymers with

either an electron-donor (D) or an electron-acceptor (A) moiety.[228,229] In this way, the strength of intermolecular π-π stacking is regulated by the D-A interactions, decoupling the light emitting function onto the most emissive moiety of introducing a new moiety devoted to radiative recombination. Some of the most used electron-acceptor building-blocks are Isoindigo,[230,231] diketopyrrolopyrrole (DPP)[232] and naphthalene diimide (NDI).[233,234]

Although all implemented strategies to obtain multifunctional materials, the polymeric nature of the proposed materials is not ideal for obtaining long-range order of the films and they are unsuitable for the design of an ambipolar single-layer OLET. Therefore, the scientific community is pushing attention to the long-range order of molecular packing achievable in thermally evaporated thin films. Among them, conjugated oligomers are surely promising structures for realizing high-mobility OLETs.

In this context, in recent years a class of materials has shown great potential as emissive ambipolar compounds with easy tunable structural and optoelectronic properties,[235] thieno[2,3-c]pyrrole-4,6-diode ended oligothiophenes, better known and herein referred to as 2,3-thieno-imide (TI) ended oligothiophenes. This class of small molecules was inspired by two of the most studied p- and n-type analogues semiconductors, a,o-dihexyl-quaterthiophene (DH4T)[236,237] and dicarbonyl ended quaterthiophene (DHCO4T),[238] respectively. In particular, maintaining the oligothiophene size have been introduced TI group (Figure 3.2.2a) in order to (i) obtain electron transport, (ii) modulate ambipolarity (major p- or n-type behavior) on the basis of the number of TI groups, (iii) tune the HOMO and the LUMO energy values, and (iv) influence the solid-state packing.[239] Moreover, the introduction of TI moieties has promoted the light emission capability of oligothiophenes in the visible range (Figure 3.2.2b), making them suitable candidates for OLET application.

In addition to that, in many cases, different structural phases (polymorphs) and then different molecular organizations were observed,[240] resulting in the attractive possibility to tune the optoelectronic and photonic properties by processing/post-synthesis treatments. Hence, through various conventional and non-conventional deposition techniques, it was possible to obtain a specific molecular arrangement characterized by designed features.[241]

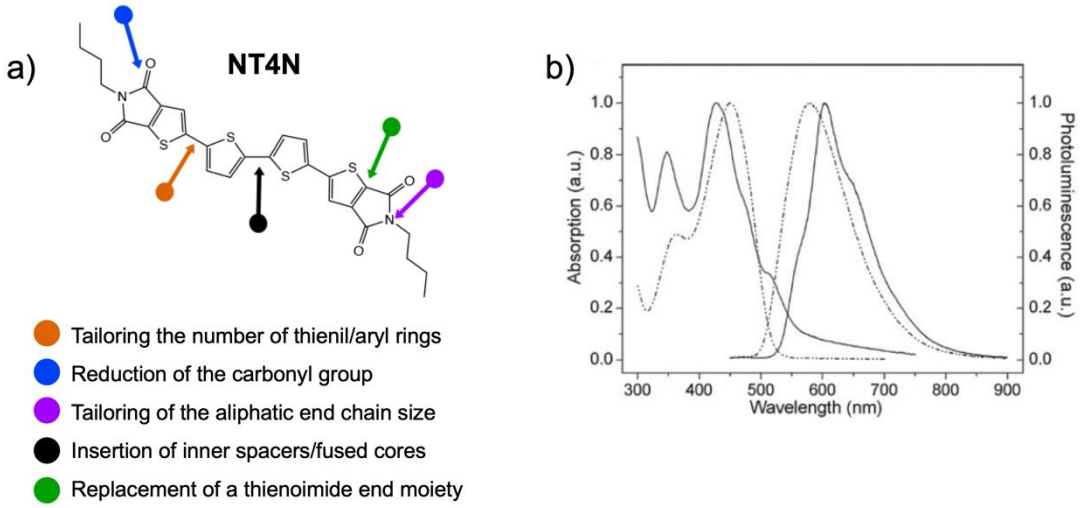

Figure 3.2.2. a) Molecular structure of the quaterthiophene derivative endowed with two TIs (NT4N) and general strategies for its modification; b) normalized absorption and emission of NT4N solution (CH_2Cl_2, 4 x 10^{-5} M, dashed line) and film (100 nm thick, solid line).

In this thesis the 2,20-([2,20-bithiophene]-5,50-diyl)bis(5-octyl-4-phenyl-4H-thieno[2,3-c]pyrrol-6(5H)-one (NT4N) small molecules was adopted (Figure 3.2.2a) as multifunctional ambipolar material in single-layer OLET fabrication.

To date, several methods to perturbate π-conjugated system of NT4N and to ultimately tune the optoelectronic and packing properties have been developed, such as the insertion of unsaturated bridges between the two thiophenes of the inner core[242] or their substitution bithiazole and thienothiophene fused rings.[243] The modification of the NT4N structure has revealed also polymorph formation, the study of which has provided essential information about molecular packaging.[244]

Several single-layer devices based on oligothiophene derivatives have been reported,[245] which have demonstrated that the NT4N-based one is the most performing.[246]

The aim of this work is to reach high ambipolar behavior coupled with the light emission of the results reported in the literature, as a starting point for the study of this class of devices and further implementation in more complex optoelectronic systems.

The symmetric end-substitution in NT4N molecule not only strongly affects the LUMO distribution and energy levels with respect to the conventional oligothiophenes but also promotes π-π stacking packing motif rather than the herringbone one, which is well-known for the enhanced capability of charge transport in molecular semiconductors (see paragraph 3.1).

From a conformational point of view, while the inner thiophene rings are always arranged in *anti*-conformation, the thienoimide moieties can adopt both *syn* and *anti*-conformation

with respect to the inner ones. As a result, two polymorphs with different conformation can exist, *anti-anti-anti* and *syn-anti-syn* (Figure 3.2.3a).

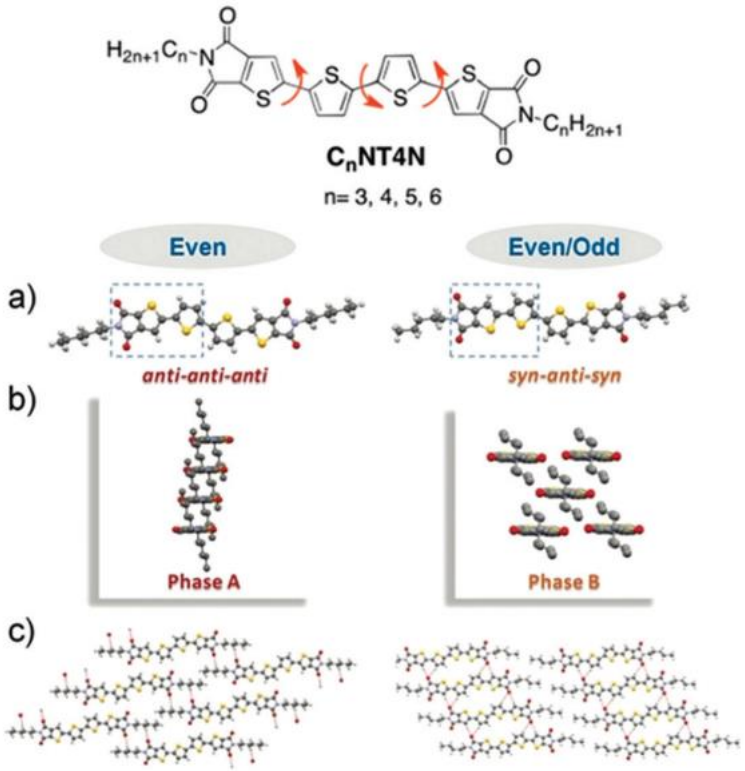

Figure 3.2.3. a) Molecular conformation of Cx-NT4N with b) view parallel to the main molecular plane and c) view normal to the main molecular plane. Figure by Moschetto et al. (J. Mater. Chem. C, 2020, 8, 15048) is licensed under CC BY-NC-ND 4.0.

The two polymorphs can adopt two different molecular packings (Figure 3.2.3b) in which the molecules can pile in columnar stacks with strong π-π vertical interactions (phase A) or molecules interact in a brick wall arrangement (phase B).[247]

The herein fabricated devices by thermal sublimation adopt selectively phase B. It has been demonstrated also the possibility to obtain phase A through the drop-casting deposition,[244] but up to now, no charge conduction has been demonstrated for this phase. NT4N layer was implemented in a bottom-gate/top-contact structure, as depicted in Figure 3.2.4.

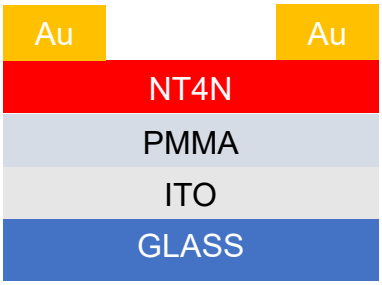

Figure 3.2.4. Schematic structure of a single-layer OLET NT4N-based in bottom-gate/top-contact configuration.

A 25 x 25 mm transparent substrate was composed of glass patterned with 150 nm thick ITO as gate electrode. The insulator layer was a film of 450 nm of PMMA spin-coated on the substrate, according to the literature procedure.[226] Then, 75 nm of NT4N active layer was deposited onto the dielectric layer by thermal sublimation in high vacuum chamber (~ 10^{-7} mbar) at a deposition rate of 0.1 Å/s. Finally, two symmetric 70 nm thick gold contacts were sublimated using a shadow mask, resulting in a transistor with channel length of L = 70 μm and channel width of W = 1.2 cm.

In order to investigate the charge transport and the optoelectronic properties of the NT4N-based field-effect transistor the standard electrical characterization was performed. As expected, the device has shown ambipolar behavior with the typical v-shape curve present in the transfer curve (Figure 3.2.5, blue curve).

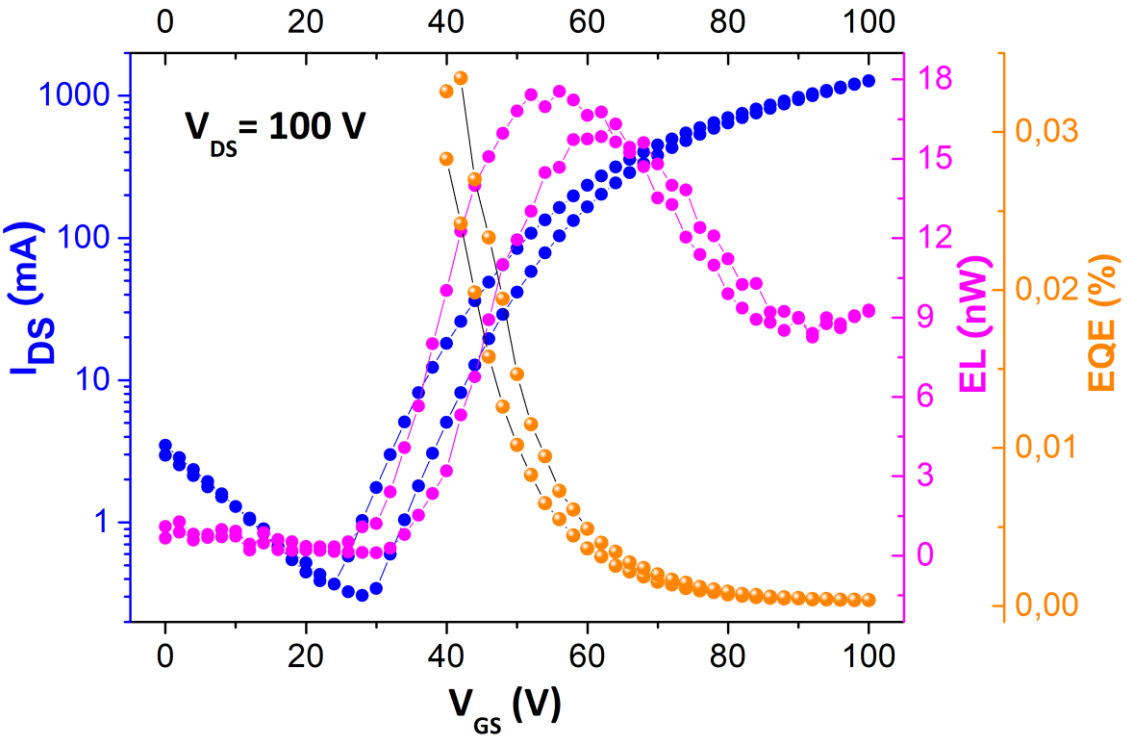

Figure 3.2.5. Characteristic curves of the NT4N ambipolar OLET. The transfer curve (blue dots) presents the typical v-shape for the ambipolar device, due to the presence of two opposite charge contributions. The optical power curve (pink dots) shows a maximum peak between 50 and 60 V of Vgs that confirms the light emission within the channel. EQE curve (orange dots) reaches the maximum roughly at the maximum of OP, decreasing exponentially in unipolar conditions (Vgs = 100 V).

From this curve both the electron and hole mobilities were extrapolated, using the I_{ds} equation for the saturation regime described in section 3.2. The resulting mobilities are of 4.6 x 10^{-1} and 4.4 x 10^{-3} cm^2 V^{-1} s^{-1}, respectively. The ON/OFF ratio has resulted in 10^7. The threshold values for electrons and holes are V_{th}^{e} = 38 V and V_{th}^{h} = -70,6 V, highlighting a partial charge unbalance in favor of electrons. These results are consistent with those reported in the literature. The curve related to the electroluminescence (Figure 3.2.5, pink curve) shows a maximum peak around V_{gs} ~ ½ V_{ds} (55 V) which represents a clear fingerprint of the light emission within the transistor channel. In fact, in unipolar devices the minority charges are injected by the metal electrode but remain under the electrode. This causes several phenomena of photon quenching due to, essentially, the excitons-contact interactions. [91,171–174] Unlike the unipolar device in which only one type of charge is effectively transported through the channel and the recombination occurs under the drain electrode because is limited by the minority charges, here the injection of

both charges from the respective electrodes leads to the recombination inside the channel, away from the electrode.

The external quantum efficiency curve (Figure 3.2.5, orange curve) in function of the I_{ds} current shows the maximum peak with a value of 0.03 % in correspondence with the maximum EL peak at around V_{gs} = 50 V, confirming that the emission inside the channel leads to highest values of EQE.

Both absolute values of optical power and EQE are resulted lower than that reported in literature, probably due to the degree of purity of the starting materials, which is not commercial.

The optical characterization of the working NT4N-based OFET highlights the emissive stripe motion within the channel (Figure 3.2.6). In particular, the images show that the emissive stripe is closer to the drain electrode when the applied V_{gs} bias is high. Conversely, the stripe moves inward at decreasing the V_{gs} value. Despite the electroluminescence area results well separated from the electrode, better balancing between hole and electron mobilities can further move the stripe inside the channel.

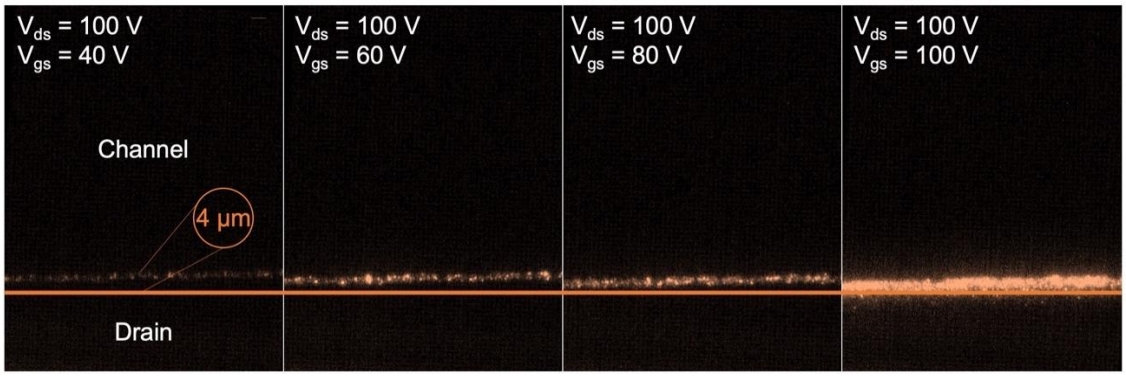

Figure 3.2.6. Optical images of the channel of NT4N-based OLET driven in different bias conditions. Keeping fixed the V_{ds} bias (100 V) and decreasing the V_{gs} one, the light emitting stripe moves from the edge of the drain electrode to the inner of the channel. Length of the channel 70 µm.

The realization of OLETs potentially usable in real-life applications requires high in-plane carrier mobility and high luminescence quantum yields, where the latter is usually low in the small molecules due to the luminescence quenching in the solid state. In this context, the NT4N molecule has proven to well-conjugate high flowing charge-density and efficient rate of formation of emissive excitons. The peculiar packing mode of this oligothiophene TI-ended, which typically organize in a brick wall arrangement (phase B), has revealed crucial in the reaching of (i) well-balanced charge carrier mobilities, as revealed from the v-shape in the transfer curve; (ii) field-effect sensitivity, as shown in

the optical images of the working OLET. In particular, as a remarkable example in the state of the art of ambipolar organic conjugated molecules, the NT4N molecule has shown an outstanding n- and p-type charge mobilities respectively of 4.6×10^{-1} and 4.4×10^{-3} $cm^2\ V^{-1}\ s^{-1}$.

Over these encouraging results, the direct access to the active channel in transparent NT4N-based OLET by using an electrooptical scanning probe technique has provided a new powerful tool for the study of charge-carrier injection, transport, and recombination properties within the same single device, permitting, in principle, to decouple the device-dependent and material-dependent issues that affect the electrical performance in organic field-effect transistors.

Despite the reported results, it is evident that enormous effort is still needed in terms of absolute performances, i.e. EQE and optical power, for the achievement of adequate performance in real-life applications. NT4N has shown an acceptable charge balance which has permitted the movement of the light stripe inside the channel of the transistor. On the other hand, if the intermolecular π-π stacking plays a positive role in the charge transport process, it is detrimental in terms of luminescence. The result is that the majority of injected charges are not converted in photons, lowering the EQE of the device.

As a consequence of this, the next section of this thesis work will be focused on the complex interconnection between the electroluminescence and ambipolar charge transport properties using another device structure, the trilayer OLET. Through an in-depth study of the interplay of the key fundamental features by exploring electron transport semiconductors with different properties, this thesis will contribute to the understanding of what factor is determinant for the device performance.

3.3 Advanced trilayer heterostructures to improve the performance of ambipolar OLETs

Part of this paragraph is adapted from:

S. Moschetto, E. Benvenuti, H. Usta, R. Ozdemir, A. Facchetti, M. Muccini, M. Prosa, and S. Toffanin
Adv. Mater. Interfaces, **2022**, 2101926 *Nanoscale*, **2019**

The use of a single ambipolar semiconducting layer endowed with electroluminescence characteristics has suffered of the low intensity of light emission under ambipolar operation due to the challenge of obtaining OSCs with both efficient ambipolar charge

conduction and electroluminescent emission in the solid state, as discussed in the previous section.

In this context, a breakthrough was achieved by introducing the trilayer OLET architecture,[164] in which the required optical and electrical characteristics are provided by three different layers. In particular, an emission layer (EML) is sandwiched between a p-type and an n-type semiconducting layers. The resulting device showed high EQE values that outperform those of the correspondence OLEDs.[164] Nevertheless, the brightness of this device is revealed weak and, consequently, several strategies have been proposed to understand the complex originating phenomena and to improve it. Among them, the use of a polyelectrolyte as an electron-injection layer (EIL) at the OSC/electrode interface was proven to improve the brightness of the device by reducing non-radiative recombinations.[249] In another approach, it was developed an asymmetric trilayer, in which top electrodes are non-planar.[250] If on one hand, both approaches have drastically improved the OLET trilayer performance, on the other hand, the devices have lost the light-emitting stripe movement within the channel via tuning of the applied biases, which is the distinguishing feature of the OLET technology.

The balance between the n-type and p-type charge transport is still a significant limitation to realizing efficient ambipolar devices. Specifically, the library of n-type OSCs with high charge mobility and suitable energy levels is relatively small if compared with p-type OSCs.[251–258] This is one of the main reasons why most studies focus on a limited number of OLET devices with similar components.[217] In addition, charge transport of OSCs used in OLETs has been mostly investigated in structures where the semiconducting layer is deposited onto a flat surface. Differently, the deposition on top of an EML in a multilayered architecture could have a serious impact on the interface between EML and the top-lying semiconducting layer, leading to relevant modification in energy levels and electrical characteristics of the semiconducting layers.[164]

The interplay of the intrinsic optoelectronic limitations of the semiconducting materials, the complex energy level alignments, and the fine control needed for the morphological properties in the multi-layered stack realization, contribute to the complex design and development of efficient device structures. As a matter of fact, the operation mechanisms of trilayer OLETs under ambipolar conditions are not fully mastered.

In this section, a comparative study is carried out to analyzes in-depth the optoelectronic features of ambipolar trilayer as a function of the EML/n-type semiconductor (n-OSC)

interface properties (Figure 3.3.1). Indeed, despite this interface is a key element for the device operation, poor attention has been devoted.

Herein, three different ambipolar trilayer OLETs based on three different n-type OSCs, i.e. ditridecylperylene-3,4,9,10-tetracarboxylic diimide (P13), (2,5-bis(4-(perfluorooctyl)phenyl)thieno-[3,2-b]thiophene (N-F2-6), and α,ω-diperfluorohexyl-quaterthiophene (DFH-4T), are fabricated, analyzed and compared. The choice of the three OSCs as the top-lying semiconductor layer arises from their different electron mobilities, and energy levels, which are expected to induce crucial changes in both the electrical and optical characteristics of the corresponding OLETs, as well as in the electron injection process into the EML.

In addition, to further identify the contribution of the EML/n-type semiconducting interface to the overall device characteristics, an interlayer was also implemented.[259] Specifically, an EIL based on a thin film of bathophenanthroline (bphen) was deposited between the EML and the n-OSC (Figure 3.3.1), and its effects on the morphological characteristics of the n-OSC and the optoelectronic characteristics of the device were investigated.

The EIL plays a fundamental double effect of (i) vertical injection of electrons, permitting to inject electrons in EML to meet the vertical flux of holes and (ii) holes extraction blocking from the EML to the n-OSC, favoring the increase of the electroluminescence efficiency.

In summary, this study aims at understanding and identifying the properties dominating the device operation mechanisms and to unravel the impact of energy levels alignment, intrinsic molecular properties, and morphological packings on charge transport and light generation processes in ambipolar trilayer OLETs.

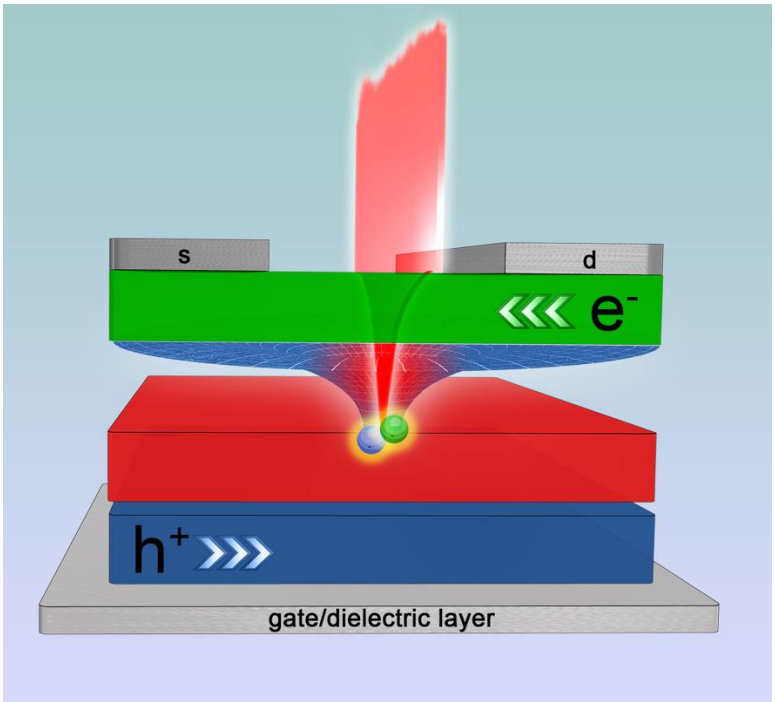

Figure 3.3.1. Schematic representation of a trilayer OLET where the EML (red layer) is sandwiched between the p-type OSC (blue layer) and the n-type OSC (green layer). The conic layer at the EML/n-OSC interface represents the electron injection layer, bphen in this case, that boosts the excitons recombination (blue and green spheres are hole and electron, respectively) inside the transistor channel with consequent light emission. Figure by Moschetto et al. (Adv. Mater. Interfaces 2022, 9, 2101926) is licensed under CC BY-NC-ND 4.0.

The three different trilayer OLETs, based on P13, N-F2-6 and DFH-4T n-OSCs, were fabricated by depositing the n-OSC on top of a bilayer structure composed of 2,7-dioctyl[1]benzothieno[3,2-b][1] benzothiophene (C8-BTBT) as the p-type charge transport material and tris(8-hydroxyquinoline)aluminum(III) (Alq3) doped with a near infrared (NIR) emitter Pt(II)–tetraphenyltetra-benzoporphyrin (Pt(tpbp)) as the host-guest EML (Figure 3.3.2a).[260]

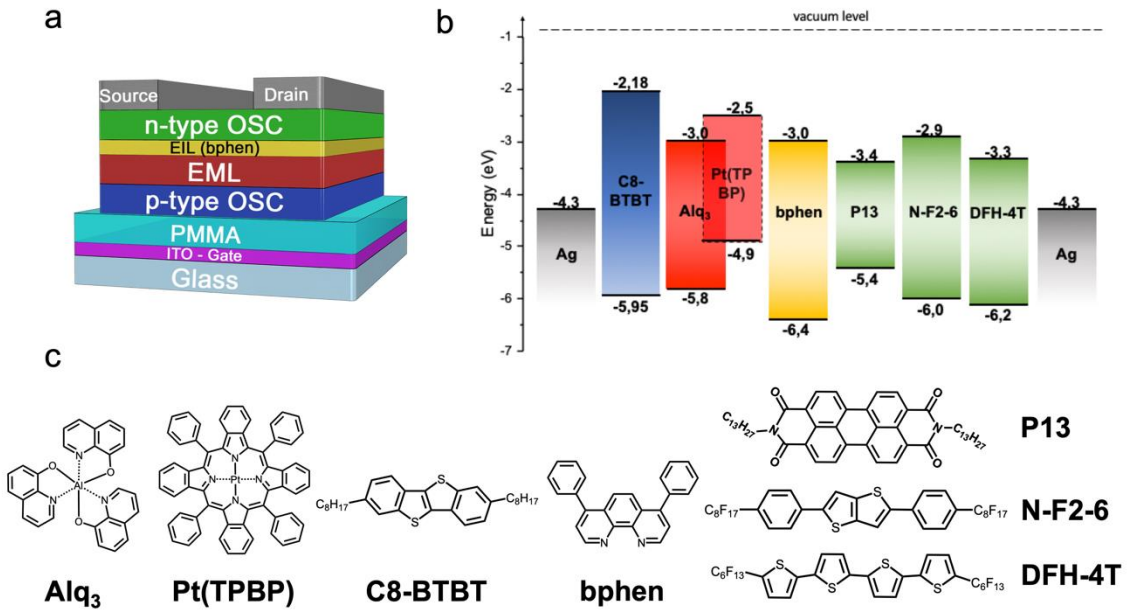

Figure 3.3.2. a) Device structure of trilayer OLETs comprising P13, N-F2-6, and DFH-4T as n-OSC. Reference trilayer OLETs do not include any bphen interlayers. b) Energy level diagram of all employed materials in the trilayer OLET structures. c) Chemical structures of the molecular compounds used in this work. Figure by Moschetto et al. (Adv. Mater. Interfaces 2022, 9, 2101926) is licensed under CC BY-NC-ND 4.0.

The choice of this dopant is dictated by the interesting NIR electrophosphorescence that could enable the device for sensing and night-vision applications.[55] Moreover, this host-guest EML has achieved EQE values as high as 6% in OLED devices.[260] All the devices were fabricated onto transparent substrates composed of glass/ITO/PMMA in order to promote light emission in both top and bottom directions. All layers were deposited by thermal evaporation in order to minimize the presence of non-rated factors in the comparative analysis. The energy levels of the layers are shown in Figure 3.3.2b.

The excellent energy alignment of the HOMO of C8-BTBT with respect to that of Alq3 guarantees an efficient p-type operation, ensuring a barrier-less hole injection from C8-BTBT to the host-guest EML. Regarding the n-OSC selection, in addition to a good energy level alignment, a high n-type mobility is necessary to guarantee a good ambipolar behavior of the trilayer structure. In particular, the hole mobility reported for C8-BTBT in bilayer device is 0.19 cm^2 v^{-1} s^{-1},[227] hence it is reasonable to choose n-type semiconductors with similar values. However, while the p-OSC is deposited on a flat surface (PMMA), n-OSC is deposited in the multilayered stack of materials and could be subject to morphological modification which consequently affects the semiconductor properties of the compound.

In particular, P13 was selected for its good electron mobility of 0.1 $cm^2 V^{-1}s^{-1}$,[261] which has led to high-performing ambipolar and unipolar OFETs.[234,262] In addition, P13 has shown well-ordered morphology in thin films due to the strong molecular interactions in the solid phase,[261] which could guarantee efficient charge transport in a multilayered device. However, in terms of energy level alignment, P13 does not guarantee an optimal alignment within the trilayer structure (Figure 3.3.2b). The LUMO level of P13 presents a non-negligible energy misalignment with respect to the Alq_3 one, suggesting a poor electron injection efficiency in the EML. In addition, its relatively high HOMO level with respect to the Alq_3 favors undesirable hole extraction from the EML. The coupling between the optimal charge transport and the suboptimal energy level alignment of P13 is beneficial to specifically understand the role of the injection barriers in OLETs.

In order to guarantee a suitable energy level alignment in the trilayer structure, the N-F2-6 semiconductor is an ideal candidate because the energy of its LUMO level is higher than that of Alq_3 (Figure 3.3.2b), ideally guaranteeing a very efficient electron injection in the EML. Nevertheless, the relatively poor electron mobility of about 8×10^{-3} $cm^2 V^{-1}s^{-1}$,[263] should negatively impact on the ambipolar characteristics of the device.

At this point, it is clear that the comparative analysis between P13 and N-F2-6-based trilayer devices is functional for understanding the roles of energy level alignments with respect to ambipolarity, respectively.

Since the trilayer structure is subjected to multiple constraints, it is necessary to find a suitable compromise between the electrical, morphological, and energy characteristics of the n-OSC.

Among the plethora of selectable n-type OSC, DFH-4T has represented the right compromise in terms of electron mobility and energy level alignments. In fact, despite the offset of LUMO energy at the interface with the EML, DFH-4T is characterized by a lower HOMO level that ensures an effective hole-blocking effect at the interface with the EML (Figure 3.3.2b), and the highest electron mobility herein reported of 0.5 $cm^2 V^{-1}s^{-1}$, comparable with the hole mobility of the counterpart C8-BTBT. This, coupled with the strong long-range molecular interaction which leads to a morphology based on large 2D islands of DFH-4T films,[264] should enable the fabrication of efficient multilayered devices.

The role of the EML/n-OSC interface and the mechanisms occurring within it are crucial in the development of an effective ambipolar device.[265] In particular, the critical role of

this interface is the switching from the horizontal flux of electrons flowing in the n-type semiconductor to the vertical flux necessary for injecting electrons in the EML.

In order to favor the electron injection process in the EML, while avoiding undesirable holes extraction into the n-OSC layer, it was introduced a typical EIL used in OLEDs, the bphen (HOMO = −6.4 eV and LUMO = −3.0 eV, Figure 3.3.2b). The introduction of this bphen-based EIL should balance the density of both charge carrier types within the EML,[266] and in addition, could act as a physical spacer to avoid undesirable non-radiative charge-exciton recombination at the EML/n-OSC interface.

The bphen EIL was introduced in all the devices in order to have a better comparative analysis. In fact, the LUMO level of bphen (- 3.0 eV) ensures the same energy offset at the EML/n-OSC interface with respect to the reference trilayer device without any EIL.

Preliminary verification of EIL in Bilayer OLETs

As the first experiment, the effectiveness of the bphen layer and its vertical injection effect into the EML layer was verified in a bilayer OLET with and without bphen-based EIL (reference device). Then, the following device stacks were fabricated: ITO/PMMA/C8-BTBT/Alq3:Pt(TPBP)/bphen/Ag and ITO/PMMA/C8-BTBT/Alq3:Pt(TPBP)/Ag (Figure 3.3.2a).

The transfer curves related to both devices show the typical characteristic for the devices operating in unipolar regime, with a quadratic increment of I_{ds} as a function of V_{gs} (Figure 3.3.3a).

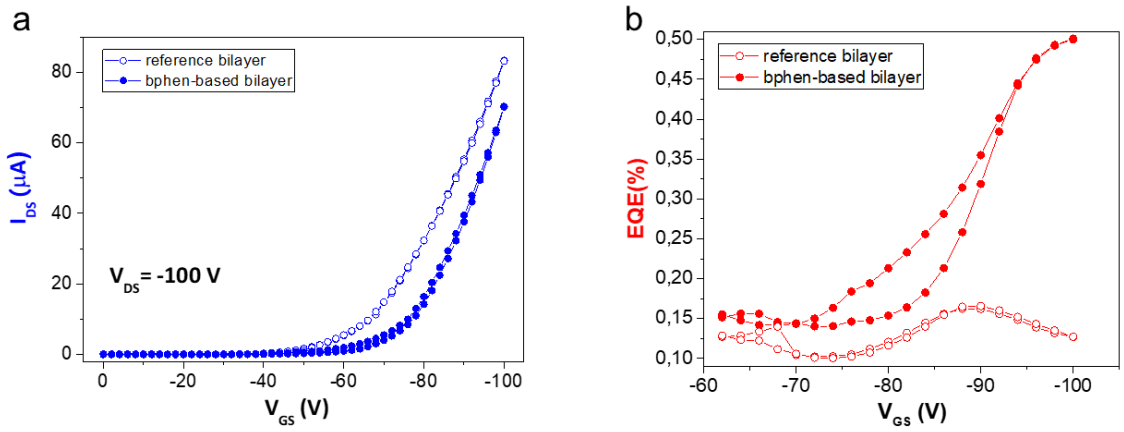

Figure 3.3.3. a) P-type transfer curves in saturation regime of bilayer OLETs with (filled blue dots) and without (empty blue dots) any bphen interlayer; b) EQE as a function of V_{gs}, at V_{ds} = −100 V, of bilayer OLETs respectively with (filled red dots) and without (empty red dots) bphen interlayer. Figure by Moschetto et al. (Adv. Mater. Interfaces 2022, 9, 2101926) is licensed under CC BY-NC-ND 4.0.

The hole mobility μ_h and the threshold voltage V_{th}^h for both the reference and the bphen-based bilayer OLETs are respectively 4×10^{-2} cm^2 V^{-1}s^{-1} and −46 V, and and 8×10^{-2} cm^2 V^{-1}s^{-1} and −62 V. The increase in the threshold voltage is due to the hole-blocking layer effect (HBL) from the source electrode of the p-type semiconductor layer.[227] As a consequence of the same effect, the electrical resistance of the device results lower and the μ_h value is doubled with respect to the reference device.

Consequently, an improvement in the optical performance with the insertion of the bphen interlayer is expected. The value of the converted free charge into photons is defined by the EQE curves reported in Figure 3.3.3b. Both devices show the typical increase of EQE for unipolar OLET, where the maximum EQE value corresponds to the highest V_{gs} value. In particular, the EQE value increases from 0.12% to 0.50% with the bphen interlayer insertion. Therefore, the presence of bphen as EIL guarantees a more efficient electron injection process in the device. Morphological contribution to this improvement arising from the underneath EML can be excluded (data not shown, see ref. [248]).

EIL insertion in Trilayer OLETs

Three different n-type OSCs were incorporated into the bilayer structure to promote the ambipolar behavior. On the basis of the previously discussed characteristics, P13, N-F2-6 and DFH-4T were deposited onto bilayer structure to study the main figures of merits (Table 3.3.1) of the resulting trilayer OLETs, with and without the presence of a bphen interlayer.

Table 3.3.1. Summary of the main figures of merit of trilayer OLETs under investigation.

Trilayer devices	n- mobility (cm^2/Vs)*	V_{th}^e (V)*	$Ids_{max(e)}$ (μA)**	p- mobility (cm^2/Vs)*	V_{th}^h (V)*	$Ids_{max(h)}$ (μA)**	EL_{max} (nW)**
P13	1,7 x 10^{-2}	32,7	180	1,1 x 10^{-1}	-19,3	427	96
bphen/P13	1,6 x 10^{-2}	48,4	214	6,3 x 10^{-3}	-80,4	125	34
N-F2-6	--	--	11	1,4 x 10^{-1}	-39,3	315	2570
bphen/N-F2-6	--	--	--	3,2 x 10^{-1}	-44,5	640	4000
DFH-4T	--	--	--	1,3 x 10^{-1}	-11,7	600	1250
bphen/DFH-4T	6,5 x 10^{-3}	57,0	8	2,3 x 10^{-1}	-30,0	674	815

*Calculated from saturation transfer curves in the saturation regime; **at |Vds| = |Vgs| = 100 V.

The deposition of P13 onto the bilayer structure has led to good ambipolar behavior, as confirmed by the p-type transfer curve in the saturation regime (Figure 3.3.4a). In fact, the v-shaped curve indicates an ambipolar operation.[267] The evidence of the n-type contribution is also confirmed by the analysis of locus and output characteristics (data not shown, see ref. [248]).

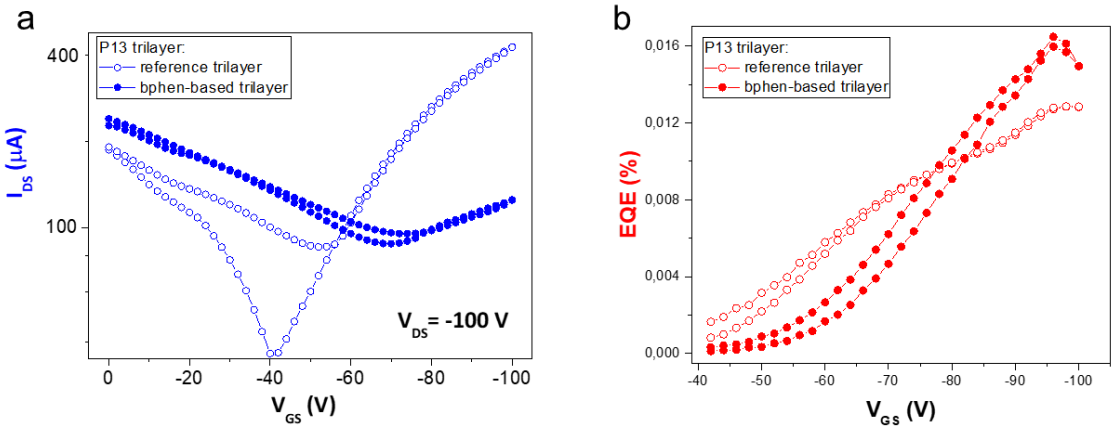

Figure 3.3.4. a) P-type transfer curves in saturation regime of P13-based trilayer OLETs with (filled dots) and without (empty dots) bphen interlayer; b) EQE curves of P13-based trilayer OLETs with (filled dots) and without (empty dots) bphen interlayer. Figure by Moschetto et al. (Adv. Mater. Interfaces 2022, 9, 2101926) is licensed under CC BY-NC-ND 4.0.

Despite the P13-based OLET has reached good ambipolarity behavior, the extrapolated electron mobility μ_e is 0.017 $cm^2\ V^{-1}s^{-1}$ (Table 3.3.1), resulting in an order of magnitude lower than the P13-based OFET, in which is 0.3 $cm^2\ V^{-1}s^{-1}$. This unexpected reduced electron mobility is a consequence of the molecular packaging, which seems to mimic the ring-shaped morphology of the underlying layers, as revealed from the AFM images (data not shown, see ref. [248])

In terms of optical performance, the optical power of P13-based OLET is as low as 96 nW (Table 3.3.1) and the EQE is around 0.016%, both maximized only under unipolar conditions (V_{gs} = V_{ds} = -100 V). These results can be explained by the relatively higher HOMO and lower LUMO levels with respect to those of Alq_3, which hinder the confinements of excitons in the bulk of the EML and then favor the non-radiative recombination over radiative events.

The insertion of the bphen interlayer at the P13/EML interface hinders the holes extraction from Alq_3 matrix, permitting to confine them in the Alq_3 layer because of the energy offset between the HOMO of bphen (−6.4 eV) and that of P13 (−5.4 eV) (Figure

3.3.2b). The transfer curve reported for the bphen-based device reveals a less pronounced p-type behavior, simultaneously promoting the n-type one, with respect to the reference OLET without bphen. In particular, the V-shaped transfer characteristic under p-type polarization shows a lower I_{ds} at $V_{gs} = -100$ V ($I_{dsmax(h)}$) (Figure 3.3.4a). The change in the balance between p-type and n-type behavior is evident also comparing the n-type output characteristics, in which the pinch-off point is reached at values of $V_{gs} \geq 20$ V for this device with bphen interlayer with respect to the reference that showed the pinch-off point at $V_{gs} \geq 80$ V (data not shown, see ref. [248]). The main reason for the different electrical characteristics between the reference and the bphen-based trilayer OLETs is due to the limited hole injection from the source electrode to the C8-BTBT layer because of bphen's deep HOMO level. Accordingly, while the ambipolarity is shifted toward the n-type behavior, the emission intensity is three times reduced with the bphen insertion.

From the EQE point of view, the maximum values are reached in unipolar conditions ($V_{gs} = V_{ds} = -100$ V) and they are similar for both devices, thus resulting in 0.012 % for the reference and 0.014 % for the bphen-based device. The maximization of the EQEs under unipolar conditions indicates that the light emission is mainly driven by the flux of holes. On the basis of these results, it is possible to assert that the radiative recombination process is limited by the energy barrier for the injection of electrons into the EML layer due to the deep LUMO level of P13, and the presence of bphen has negligible influence on this process. In summary, the implementation of P13 in trilayer OLETs has highlighted the crucial role that the energy level alignment has on the optical characteristics of the devices.

In order to provide better energy level alignments, N-F2-6 was implemented in trilayer OLETs. Indeed, the high LUMO level of N-F2-6 (-2.9 eV) with respect to that of Alq_3 (-3.0 eV) should guarantee an efficient electron injection process into the EML. This is confirmed by the high EQE of 0.5 % (Figure 3.3.5b) and the optical power of 2570 nW (Table 3.3.1), both reached in unipolar conditions ($V_{gs} = V_{ds} = -100$ V). On one hand, the fact that the maximum value of EQE is similar to that of the reference bilayer OLET (Figure 3.3.3b) confirms the optimal energy level alignment within the OLET structure.

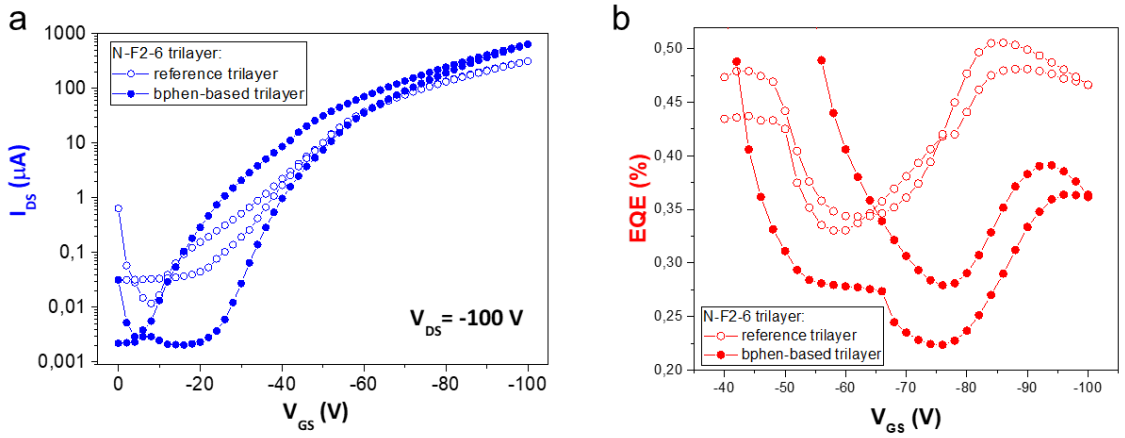

Figure 3.5.5. a) P-type transfer curves in saturation regime of N-F2-6-based trilayer OLETs with (filled dots) and without (empty dots) bphen interlayer; b) EQE curves of N-F2-6-based trilayer OLETs with (filled dots) and without (empty dots) bphen interlayer. Figure by Moschetto et al. (Adv. Mater. Interfaces 2022, 9, 2101926) is licensed under CC BY-NC-ND 4.0.

On the other hand, the transfer characteristics (Figure 3.3.5a) do not show any v-shaped curve, and hence a very poor n-type behavior is obtained, as highlighted by a low $I_{dsmax(e)}$ (Table 3.3.1) that also hinders the estimation of $V_{th(e)}$ and μ_e. The significant imbalance between electron and hole transport in the N-F2-6-based device is further confirmed by the n-type output curves, in which the saturation regime is not reached even at a bias as high as V_{gs} = 100 V (data not shown, see ref. [248]). These poor electron transport properties make the N-F2-6-based OLET a unipolar device. In addition, the similarity of their characteristics to those of bphen-based bilayer OLETs suggests that N-F2-6 functions as an EIL, rather than an n-OSC. Thus, to evaluate the effect of the insertion of an EIL on the n-type behavior of the n-OSC, a bphen interlayer was implemented at the N-F2-6/EML interface. The insertion of the bphen interlayer has further deteriorated the n-type electrical properties with respect to the reference device, as confirmed by the locus curve (data not shown, see ref. [248]). While the output characteristics remain similar to those of the reference device, the p-type transfer curve (Figure 3.5.5a) shows a more pronounced hysteresis. This behavior, coupled with the EQE decreasing from 0.50 % for reference to 0.36 % for bphen-based device, indicates a charge accumulation process at the N-F2-6/bphen or EML/bphen interface due to the presence of the bphen interlayer. The relatively poor transport characteristics of N-F2-6 was investigated by morphological analysis (data not shown, see ref. [248]) which has revealed that the molecular packing is i) independent of the presence of a bphen interlayer and ii) similar to the molecular organization occurring on flat surfaces.[263] Hence, the further deterioration as a

consequence of the bphen introduction is probably due to the formation of a new interface (i.e., N-F2-6/bphen or EML/bphen) that traps electrons. It is possible to conclude that the insertion of a new additional layer in an optimized structure in terms of energy level alignment is critical for the device performance.

Overall, from the study of P13- and N-F2-6-based devices, it is possible to conclude that the achievement of optimal performances in terms of ambipolarity and optical power generation is closely linked to the interplay between energy level alignment, charge transport characteristics of n-OSC, and the nature of the EML/OSC interface in trilayer OLETs. In the first case, the OLET based on P13 has shown well-balanced charge densities but poor emission characteristics because the electrons mostly populate the P13 layer rather than being injected into the EML. Conversely, the OLET based on N-F2-6 has shown good emission properties as the consequence of an optimal energy level alignment but exhibiting a unipolar behavior of the device. In both cases, the implementation of the bphen-based EIL has had a negligible influence on the electrical and optical properties of the devices.

In order to find the right balance of the optoelectronic properties, DFH-4T was investigated as n-OSC in trilayer OLETs. In fact, DFH-4H is characterized by charge transport similar to those of P13 and, in addition, it presents a deeper HOMO level (-6.2 eV) with respect to that of P13 that could prevent the injection of holes from EML to the n-OSC.

The trilayer OLET based on DFH-4T showed a rather unbalanced electrical behavior that is mostly dominated by hole transport, as it can be seen from the unipolar behavior of p-type saturation transfer characteristics (Figure 3.3.6a). This result is unexpected considering the comparable values of charge mobilities between C8-BTBT and DFH-4T.

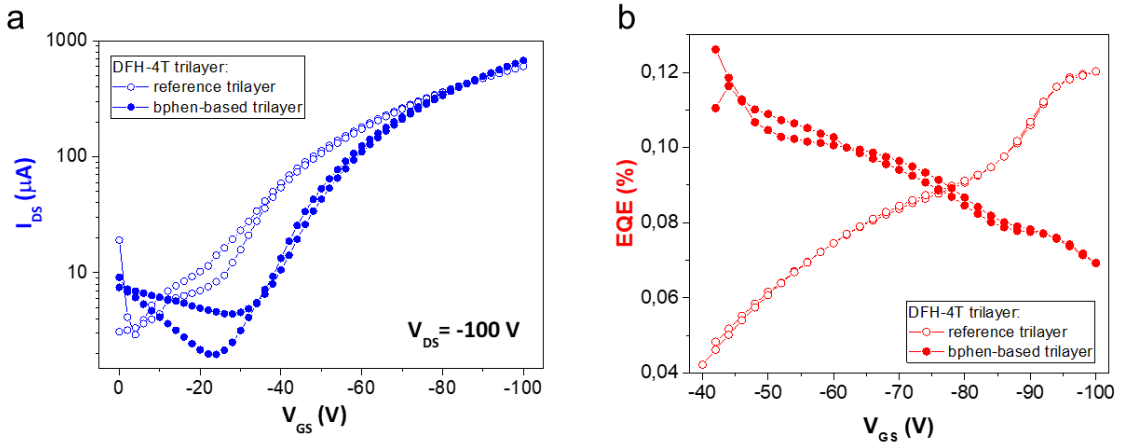

Figure 3.3.6. a) P-type transfer curves in saturation regime of DFH-4T-based trilayer OLETs with (filled dots) and without (empty dots) bphen interlayer; b) EQE curves of DFH-4T-based trilayer OLETs with (filled dots) and without (empty dots) bphen interlayer. Figure by Moschetto et al. (Adv. Mater. Interfaces 2022, 9, 2101926) is licensed under CC BY-NC-ND 4.0.

The p-type operation of the device is also confirmed by the output curves in which the I_{ds} saturation regime is reached only under negative polarization of the gate dielectric (Figure 3.3.7a) and the pinch-off point not reached under positive gate polarization (data not shown, see ref. [248]). Interestingly, the use of an n-OSC with a deeper HOMO lever than that of P13 has led to an improvement in terms of light emission intensity under unipolar conditions. The optical power has increased from 96 nW to 1250 nW passing from P13- to DFH-4T-based devices (Table 3.3.1). Accordingly, the EQE_{max} is one order of magnitude higher than that of the P13-trilayer OLET and increases from 0.012% to 0.12% at $V_{gs} = -100$ V (Figures 3.3.4b and 3.3.6b). It is clear that the HOMO level of DFH-4T is crucial in the exciton formation processes in the EML thanks to the barrier effect for the hole injection into the DFH-4T layer.

The insertion of a bphen interlayer at the DFH-4T/EML interface has dramatically changed the electrical characteristics of the trilayer OLET based on DFH-4T. In particular, in addition to the p-type one, the n-type contribution is appeared in p-type saturation transfer curve, as indicated by a clear V-shape curve which was absent in the reference device (Figure 3.3.6a). Despite the p-type contribution is more pronounced, the n-type characteristics are clearly visible from the locus curve and the n-type output curves (data not shown, see ref. [248]). Hence, unlike the P13-based OLET, the implementation of the bphen interlayer into DFH-4T OLET improves the n-type performances while preserving the p-type behavior of the OLET structure. The electrical characteristics modifications also affect the threshold values V_{th}^{h}, which increases from -11.7 to -30.0,

probably due to the enhanced hole injection barrier from the source electrode to the C8-BTBT as a result of the bphen insertion. The most interesting and totally unexpected behavior of bphen-based OLETs is represented by the inversion of the EQE trend as a function of V_{gs}, if compared with the reference OLET (Figure 3.3.6b). In particular, the maximum value of 0.12% is reached for the reference OLET in unipolar conditions at V_{gs} = V_{ds} = −100 V, while bphen-based OLET reaches the same value at V_{gs} = -40 V, decreasing at V_{gs}= -100 V.

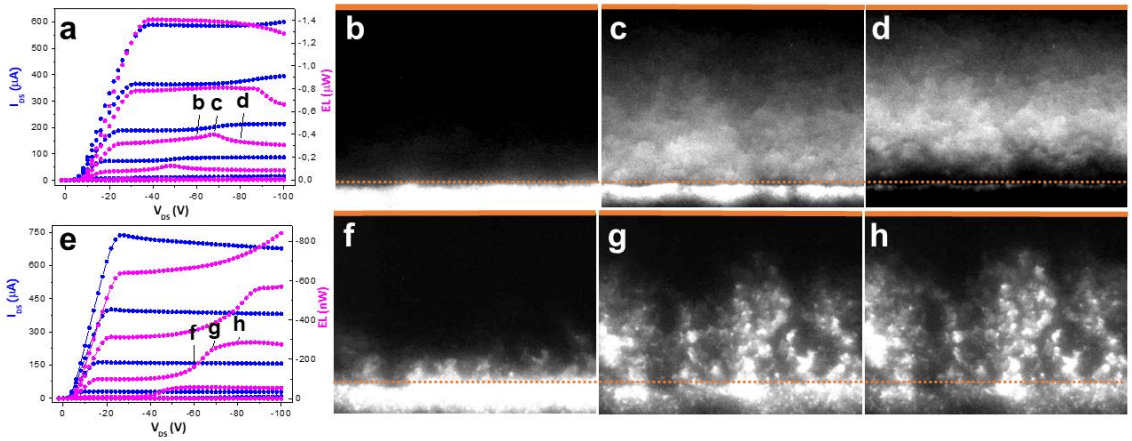

Figure 3.3.7. a,e) P-type output curves and b–d,f–h)optical images of reference (a–d) and bphen-based (e–h) DFH-4T-trilayer OLETs. From left to right, optical images refer to V_{gs} = −60 V and V_{ds} = −60, −68, and −80 V as indicated in the corresponding panel (a) and (e). Dotted and solid orange lines indicate the inner edge of the drain and the source electrodes, respectively. Images are recorded through the glass substrate with a 60× magnification. The lateral dimension of the optical images is 120 μm × 80 μm. Figure by Moschetto et al. (Adv. Mater. Interfaces 2022, 9, 2101926) is licensed under CC BY-NC-ND 4.0.

By comparing those EQE values with that reported in the literature, it is further clear the optical switching from unipolar to ambipolar behavior of the device as a consequence of the bphen interlayer introduction. In fact, while unipolar OLET reaches maximum EQE values at the maximum gate bias,[227] at the same bias the ambipolar ones have values close to zero, to reach the maximum EQE for minor values of V_{gs} bias.[164]

From the light emission point of view, unusual variations have been noticed during the analysis of the p-type output curves (Figures 3.3.7a,e). In particular, the reference device shows a transient peak of the optical power of emission with increased V_{ds} at V_{gs} = -60 V (Figure 3.3.7a, please refer to points b, c and d). Diversely, bphen-based OLETs exhibit a gradual enhancement of the optical power as a function of V_{ds} at V_{gs} = −60 V, which reaches a plateau by further increasing V_{ds} (Figure 3.3.7e, please refer to points f, g and h). To analyze the device operation in-deep, an optical imaging of the spatial region of

emission as a function of the source-drain bias was performed. The optical images were acquired, keeping a constant V_{gs} of -60 V, at three different V_{ds} values of -60, -68, and -80 V (Figure 3.3.7).

When a bias of $V_{gs} = V_{ds} = -60$ V is applied, the device is operating in an almost unipolar condition. The corresponding optical images for the reference and the bphen-based devices (respectively, Figures 3.3.7b and f) exhibit a pattern of emission that involves the spatial region corresponding to the drain electrode. Since the electrical characteristic of the reference trilayer device has exhibited unipolar behavior, the light emission is not expected to be detected in the region of the transistor channel, in the range of V_{ds} from -60 V to -68 V. Conversely, the relative image (Figure 3.3.7c) shows a pattern of emission that involves the transistor channel in conjunction with a residual illumination from the region corresponding to the drain electrode. Thus, the evidence of light emission occurring within the transistor channel, typical for ambipolar OLET, is in contrast with the electrical characterizations, which instead highlights a unipolar behavior. It is possible to speculate that the ambipolarity of the reference DFH-4T-based OLETs hides behind a more pronounced p-type behavior. All electrical curves are characterized by an n-type contribution that is overwhelmed by the p-type behavior. As a consequence, the emission pattern of OLETs can provide a direct fingerprint and a more sensitive indicator of the fundamental device electrical characteristics with respect to the standard electrical measurements. Therefore, the bias-dependent optical emission can be implemented as a straightforward method to better identify the intrinsic OLET electrical features.

The bphen-based OLET is assumed to operate under a slightly more ambipolar regime with respect to the reference device, then it is expected that the radiative recombination events are located between the source and the drain. Diversely, the bphen-based device shows a pattern of emission involving both the drain electrode and the transistor channel by increasing the V_{ds} from -60 to -68 V. Unlike the reference devices, homogeneous illumination of the full area of the drain electrode can also be noted in bphen-based OLETs. This observation likely suggests that the operation of the bphen interlayer as EIL enables radiative recombination events to occur in the region corresponding to the drain electrode, thus adding up to the light emitted in the OLET channel under this specific bias condition. Generally, the further increase of the V_{ds} bias to -80 V, at fixed $V_{gs} = -60$ V, favors a more pronounced ambipolar regime. Then, it is expected that the charge recombination processes move gradually from the drain electrode region toward the transistor channel for both devices. In the reference device, the optical power is reduced

(Figure 3.3.7a, point d) and the emission zone becomes wider (Figure 3.3.7d), thus confirming the assumption reported before.

The analysis of the emission pattern for the bphen-based device underlines the light emission from both the transistor channel and the drain electrode (Figure 3.3.7h), as it occurs for bias of V_{ds} = -68 V (Figure 3.3.7g). The main difference between the reference device and the bphen-based device concerns the emission of light under the drain electrode. Since the light emission under the drain is not expected in ambipolar conditions and it is known that it is dominant under unipolar conditions, it can assert that the bphen interlayer implementation in DFH-4T-based OLET promotes the vertical injection of electrons from the drain electrode to the EML layer, acting as an effective EIL.

The analysis of the pattern of emission under different bias conditions can help to understand the trend inversion of EQE as a consequence of the bphen interlayer insertion (Figure 3.3.6b). In general, in both devices, the unipolar regime is induced at $|V_{ds}| = |V_{gs}|$, while the ambipolar regime occurs when $|V_{ds}| > |V_{gs}|$. Hence, if analyzing the EQE at V_{ds} = −100 V and V_{gs} = −40 V (Figure 3.3.6b), the ambipolar regime of operation occurs in both devices and hence their emission patterns is expected to resemble that shown in Figure 3.3.7d,h. The enhancement of the EQE in the bphen-based device with respect to the reference device is clearly due to the improved electron injection into the EML.

Considering increasing the V_{gs} up to -100V, at V_{ds} of -100 V both OLETs switch from ambipolar to unipolar operation. In this case, the pattern of emission should be similar to that shown in Figure 3.3.7b,f, where the OLETs were in unipolar conditions (V_{ds} = V_{gs} = -60 V). In these conditions, where the emission region in both the device corresponds to the drain electrode but the EQE values are different (Figure 3.3.6b), it is possible to assert that the EIL enables a diode-like behavior of the device in which quenching mechanisms, such as exciton-charge annihilation, occur.

Together with the light emission zones, in optical images it is possible to see different patterns of emission for the bphen-based and reference trilayers. In particular, the pattern of emission of the bphen-based device presents a coarser pattern with respect to the reference device (Figures 3.3.7c,d,g,h). Consequently, a deeper morphological investigation was performed by AFM (Figure 3.3.8).

It is worth noting that the morphology of the DFH-4T films deposited on a flat surface generally is composed of homogeneous 2D islands.[164] In this case, the deposition of DHF-4T directly onto the EML leads to 3D domains as high as ≈ 50 nm (Figure 3.3.8a), which is probably the reason for the poor ambipolar characteristics of the DHF-4T-based

OLETs. Diversely, the addition of the bphen interlayer at the DFH-4T/EML interface has significantly changed the morphology of the DFH-4T film with respect to that grown on top of the EML.

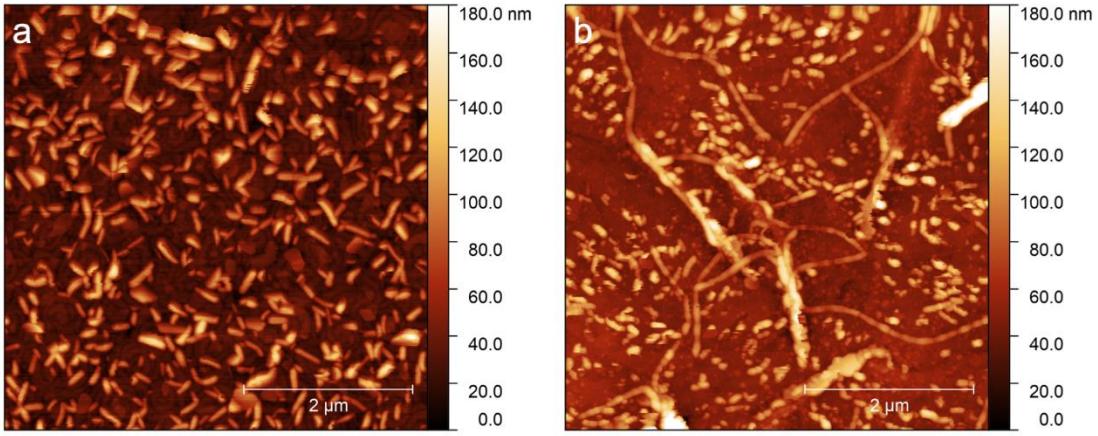

Figure 3.5.8. AFM images of DFH-4T recorded within the corresponding OLET channel of the a) reference and b) bphen-based devices. Lateral dimensions: 5µm. Calculated RMS is 26 nm for both devices. Figure by Moschetto et al. (Adv. Mater. Interfaces 2022, 9, 2101926) is licensed under CC BY-NC-ND 4.0.

The DFH-4T film grown onto bphen layer presents filamentary structures a few micrometers long (Figure 3.3.8b), which lead to the formation of long percolative pathways. From the electrical point of view, this effect explains the increase of the lateral electron transport through the DFH-4T layer, which results in a more balanced ambipolar behavior of the bphen-based device with respect to the reference device. If comparing the relation between the increased ambipolarity and the high EQE values in ambipolar conditions in bphen-based device, it is clear that a greater number of electrons pass through the DFH-4T layer and then are injected into the EML layer with respect to the reference device.

Overall, the insertion of the bphen interlayer in DFH-4T OLET allows to i) extend the spatial area of emission by keeping the region under the drain electrode active even under ambipolar operation, and ii) improve the number of recombination events as a consequence of the formation of lateral percolative pathways, permitting to double EQE values with respect to those obtained in reference device by using V_{gs} as low as -40 V.

The optimal design of ambipolar trilayer OLETs is subjected to a multitude of factors contributing to its performance and operation.

This comparative work has analyzed the interplay of different factors such as energy level alignment, charge transport, and morphology with the aim to elucidate and to understand their role and weight on the performances of this class of devices.

The importance of the energy level alignment and the need of well-balanced charge transport was confirmed by the use of P13 and N-F2-6 as n-OSCs layers on top of the EML. Coupled with these intrinsic characteristics of the materials, the weight of morphology and then the interfacial properties at the EML/n-OSC have proved to be equally important for optimizing charge transport and light generation in DFH-4T-based OLETs. The DFH-4T deposition onto the EML indeed has led to the formation of 3D domain, impacting the charge transport properties of the DFH-4T layer and then causing a poor ambipolar behavior of the DFH-4T-based OLET. The bphen interlayer implementation at the DFH-4T/EML interface has acted on the solid-state molecular packing, improving its organization and thus favoring the ambipolarity. Together with the morphologic modifications, the efficient vertical injection property has permitted to increase the number of electrons injected into the EML, allowing a $\approx 2\times$ improvement of EQE at reduced bias applied. To summarize, the introduction of a bphen interlayer in DFH-4T-based OLET has allowed to i) expand the OLET emissive area and the geometrical fill factor, as it is desired for pixel design in display applications, and ii) extend the library of materials that can be used in OLET applications starting from materials typically used in OLED devices.

In conclusion, the bidimensional nature of the OLET trilayer heterostructure coupled with the pivotal importance of interfaces in multilayered optoelectronic devices, underlines the necessity to have better control of the multitude of mechanisms that occur at the two EML/OSC interfaces. Moreover, despite the need to extend the n-type library to improve the ambipolarity behavior of the trilayer structure, the use of an injection layer thoroughly selected is strongly recommended in this kind of device.

Furthermore, thanks to the study of the bias-dependent pattern of emission, this work has provided a more sensitive method to evaluate the OLET ambipolarity with respect to the standard analysis of the electrical characteristics of the device.

3.4 Conclusions

The second part of this thesis focused on developing highly ordered organic heterostructures to avoid exciton quenching and other phenomena that lead to photons losses in traditional optoelectronic devices, such as OLEDs.

In this context, one of the most promising structures to reach high efficiency and optical performance is OLET. Basically, the improvement in terms of electroluminescence and EQE in those devices is strictly linked to the ambipolar condition.

In order to reach ambipolarity, several OLETs structures have been developed. As the first approach, it was used a single-layer OLET based on the ambipolar emissive organic semiconductor NT4N. This small-molecule semiconductor has reached well-balanced charge carrier mobilities, as confirmed by n- and p-type charge mobilities of 4.6×10^{-1} and 4.4×10^{-3} cm^2 V^{-1} s^{-1}. Moreover, NT4N-based OLET has shown high field-effect sensitivity, as highlighted by the light stripe movement inside the channel of the transistor by varying the gate voltage. In this context, the direct access to the active channel in transparent NT4N-based OLET by using an electrooptical scanning probe technique has provided a new powerful tool for the study of charge-carrier injection, transport, and recombination properties within the same single device, permitting, in principle, to decouple the device-dependent and material-dependent issues that affect the electrical performance in organic field-effect transistors.

Despite these results, the electroluminescence intensity in NT4N film resulted to be poor. This was ascribed to the intermolecular π-π stacking, which positively influenced the charge transport at the expense of luminescence.

Aimed to maximize both the electroluminescence and the ambipolar charge transport, the trilayer OLET was therefore investigated. Through a comparative study on different n-type OSCs such as P13, N-F2-6, and DFH-4T, coupled with an electron injection layer such as bphen, an interesting insight on the OLET trilayer operation was obtained. The use of P13 and N-F2-6 has confirmed the importance of the energy level alignment and the need of well-balanced charge transport. On the other hand, the bphen insertion in DFH-4T-based OLET has caused a switch from unipolar to ambipolar behavior because of morphological changes of the n-type OSC, with a clear inversion of the device EQE trend and a $\approx 2\times$ improvement of EQE at reduced bias applied. Moreover, the bphen interlayer addiction has expanded the emissive area and the geometrical fill factor, as desired for pixel design in display applications.

Together with these important results with respect to the complex phenomena in trilayer OLETs, thanks to the study of the bias-dependent pattern of emission, this work has provided a more sensitive method to evaluate the OLET ambipolarity with respect to the standard analysis of the electrical characteristics of the device.

In conclusion, the NT4N-based heterostructure has underlined the limitations still affecting the realization of an OLET based on a multifunctional single-layer. The separation of the device functions into different layers, that is the case of trilayer OLET architectures, resulted more effective in terms of optical performance in comparison with ambipolar single-layer devices. Nevertheless, the bidimensional nature of the trilayer OLET heterostructure has underlined the necessity to have better control of the multitude of mechanisms that occur at the two EML/OSC interfaces and the need to extend the n-type library to improve its ambipolarity.

Chapter 4

Conclusions

This work of thesis aims at realizing hybrid and fully organic heterostructures in order to overcome current material limitations as well as to add new functionalities to the final system.

In the first part, the thesis focused on a 2D material with excellent optoelectronic properties, the phosphorene or 2D bP. Despite its appealing properties, such as the direct, tunable band-gap and high charge mobility, its environmental instability and lab-scale processability hamper a possible use in real-setting applications.

Multiple and different chemical-physical approaches were developed to control the high reactivity of 2D bP in air and to enable large-area deposition.

In relation to approaches for passivating the oxygen sensitive 2D bP outer surface, a hybrid inorganic/organic vdW heterostructure composed of 2D bP and tetracosane (C24) was realized. In the C24 multilayer/2D bP heterostructure the oxidation process was delayed, since the new system preserves the phosphorene-correlated properties for 18 hours, instead of only 1 hour as in the case of bare 2D bP. Finally, the experimental evidence of the modulation of polarizability of 2D bP by the C24 epitaxial layer corroborates the hypothesis of the use of the hybrid vdW heterostructure for possible use in in metal-insulator-semiconductor based devices.

Another hybrid heterostructure based on noncovalent interactions was realized by exploiting the affinity between the 2D bP and organic molecules. In particular, 2D bP was functionalizated with pyrene derivatives molecules. The 2D bP/pyrene derivatives heterostructures showed high stability in air for more than 6 months. In addition, thanks to photosensitive properties of pyrene moiety that are modulated by the presence of the underneath 2D bP, the system can be implemented as a fluorescent chemosensor for oxygen detection.

The investigation of different chemical-physical approaches in the decoration of 2D bP has led to the realization of inorganic/inorganic heterostructure implementing Au NPs.

Contrary to what is already present in the literature, the realization of this heterostructure consists of in-situ formation process of Au NPs through a solid-liquid heterogeneous reaction which does not consider the use of stabilizer. Moreover, as predicted by theoretical calculations and confirmed by XPS measurements, the formation of the heterostructure involves the soft-pairing/coordination between P atoms form the surface of 2D bP to the Au atoms on the surface of the Au NPs. A partial charge transfer with a positive charge localized on the Au atoms directly bonded to the 2d bP, occurs. This "stabilizer -free" approach can enhance the intimacy contact between 2D bP and Au NPs, improving the performance of the already used 2D bP/Au NPs systems in electrochemical sensing[145] applications, or in plasmonic- or photonic-based biological applications.[146]
Although all the proposed approaches to create functional heterostructures has proved to be efficient, the scalability issues correlated to the possible mass production of 2D bP might prevent the use of 2D bP-based nanomaterials for the electronic appliances market. Consequently, it was developed a new exfoliation technique based on the electrospray process for the production of air-stable phosphorus oxide-based nanomaterial. The deposited electro-sprayed flakes had an average lateral size of hundreds of μm^2, conversely to the tens of μm^2 obtained by mechanical and liquid exfoliation. Moreover, the piezoresponse force microscopy measurements performed on the exfoliated P_2O_5 flakes revealed clear electromechanical responsivity, making it very attractive in the sensing and energy-harvesting fields.

The realization of 2D bP-based heterostructures clearly demonstrated that the combination of different materials with different properties can modulate, suppress or add characteristics to the starting material.
In this context, the second part of the thesis focused on the implementation of fully organic heterostructures as active region in OLET devices, in order to completely exploit the high potential of this class of devices for reaching high external quantum efficiency and bright light emission. A single-layer OLET based on the multifunctional ambipolar emissive organic semiconductor NT4N was introduced and developed. The device based on this small-molecule semiconductor reached well-balanced charge carrier mobility and has shown high field-effect sensitivity, as highlighted by the bias-dependent movement of the emissive stripe inside the channel. Despite the promising results, the collected optical emitted power was too small to support the use of multifunctional NT4N film in real-setting applications. This result is expected for this class of conjugated compounds

since the strong intermolecular π-π stacking that masters the packing of the molecules in the thin film positively influences the charge transport but while affects light-emission efficiency.

To further improve the electroluminescence under ambipolar operation, an organic-organic heterostructure was developed and inserted as active region in the OLET. In detail, the heterostructure is composed of an emission layer (EML) sandwiched between an n-type and a p-type organic semiconducting layers (OSCs). Through a comparative study using different electron transporting organic semiconductors and introducing an electron injection layer , we demonstrated that several criteria must be considered in the realization of multilayer stack based OLETs, such as (i) the suitability of the energy level alignment within the structure, (ii) the request for well-balanced charge mobilities of holes and electrons, and (iii) the control of the morphology at the EML/OSCs interfaces. By satisfying all the criteria, the trend in the optoelectronic performance of prototypal OLET devices was modulated from unipolar to ambipolar charge transport while a $\approx 2\times$ improvement of EQE was obtained at reduced applied bias.

In conclusion, we engineered and investigated innovative heterostructures on both inorganic and organic materials, and implementing both ordered bidimensional and polycrystalline thin-films whose properties are strictly correlated not only to the functional and structural properties of the single materials comprising the heterostructures but also on the processing.

The introduction of suitably engineered vdW heterostructures based on 2D bP might be considered a smart approach for proving strong control of the interfaces and introducing innovative functionalities. In fact, the mass production of 2D bP for the electronic appliances market will require a concerted effort to combine wafer-scale fabrication and high control of the atomic-ordered surface.

The optimization of organic heterostructures in a benchmark device platform such as OLET highlighted the crucial role of the interface between the emission layer and the topmost charge-transport semiconductor in multilayered optoelectronic devices in terms of energy levels alignment, electron injection process, and thin-film morphology for assessing a synergetic trade-off between field-effect lateral charge transport and bulk transversal charge recombination.

In general, the effective use and the combination of the knowledge and skill gained during the experimental activity developed in this thesis work will help to design electronic and optoelectronic devices based on niche and/or innovative materials in view of their

possible implementation in large-scale production. In particular, new routes of engineering of 2D bP-based heterostructures, coupled with the developed large-area deposition process, could lead to a first step of macro-application of this material. In addition, considering that phosphorus is an extremely abundant element, its large-scale implementation could lead to filling the gap arising from the ongoing and increasing semiconductor shortage in the field of chips.[268] Further, the knowledge acquired on the multilayered organic optoelectronic devices can be exploited as a tool to overcome the limitation in terms of suitable materials for bidimensional devices such as OLETs, paving the way to the commercialization of more efficient and integrated devices as requested by the recent assessment of the sustainable global economy.

Chapter 5

Experimental setup

5.1 Techniques of exfoliation and deposition of 2D bP

Mechanical exfoliation

To date, mechanical exfoliation is the technique that permits to obtain of the purest 2D bP flakes because is performed in absence of solvents.

The process is done entirely in glovebox by using an appropriate adhesive tape called "*blue foil*" o "*blue tape*", having an average thickness of 3 mm.

The black phosphorus crystal is cleaned from eventually oxidized layers by removing the superficial layers using a piece of blue foil. This process is called peeling (Figure 5.1.1a). Then, the crystal is transferred onto another new blue foil and peeled again depending on the desired amount of material. Once the excess crystal is removed from the blue tape, is possible to exfoliate the remaining pieces of crystal within the scotch. During the folding of the blue tape, it is appropriate to distribute the material homogeneously into the scotch by folding the tape in different directions (Figure 5.1.1b). The more the number of blue tape folding, the more fragmented the phosphorene flakes. The number of folding used in this thesis work ranges from 25 to 35.

2D bP deposition is operated by just leaning the substrate onto the blue foil with small exerted pressure (Figure 5.1.1d). Finally, the blue foil is slowly removed to avoid eventual glue residuals.

Figure 5.1.1. Mechanical exfoliation of black phosphorus. a) peeling of the black phosphorus crystal, b) *blue tape* folding process, c) final result at the end of exfoliation, and d) 2D bP deposition on the substrate.

Below optical (Figure 5.1.2) and AFM imaging (Figure 5.1.3) of the 2D bP mechanically exfoliated by blue tape from bulk bP onto Si/SiO2 substrates or quartz is shown. Are obtained flakes with an average lateral size of around 1µm and thickness from 50 nm to a few nm. The average superficial coverage extrapolated from the optical images in Figure 5.1.2 is 4% of the total area of the substrates.

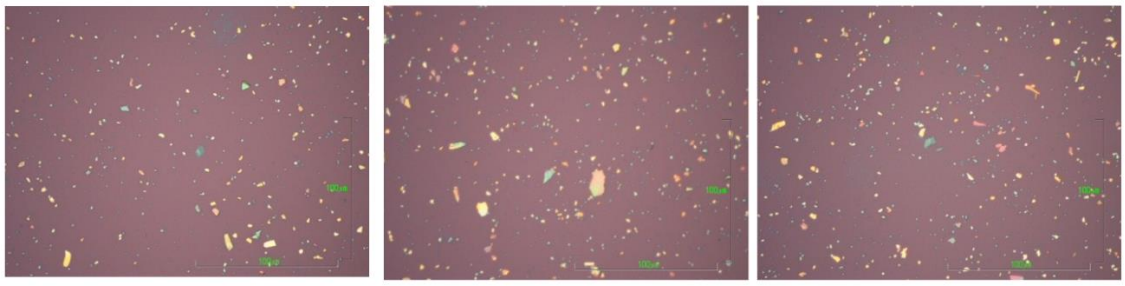

Figure 5.1.2. Optical microscopy images in different areas of a sample of mechanically exfoliated 2D bP on a Si/SiO2 substrate.

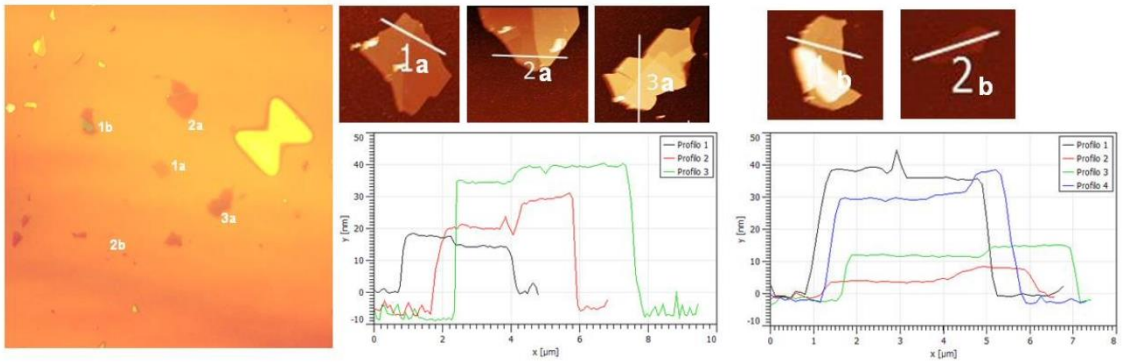

Figure 5.1.3. Left: Optical microscopy image of a sample of mechanically exfoliated 2D bP on a Si/SiO2 substrate equipped with numbered reference points for mapping (i.e. butterfly mark in the image); Top: AFM height images of the flakes mapped with optical microscopy; Bottom: profiles along the lines on the flakes, as reported in images (b-f).

Liquid exfoliation

A black phosphorus crystal is dipped in the solvent (1 mg/ml), usually DMSO, THF (tetrahydrofuran), or NMP (N-Methyl-2-pyrrolidone) and sealed in a glass vial in inert atmosphere. Then, the vial is sonicated for 5 days to exfoliate the black phosphorus crystal. In order to reduce the amount of aggregates and to minimize the staking tendency of exfoliated black phosphorus, the suspensions is centrifuged at 1000 rpm, and the supernatant is collected. The supernatant is dissolved in 1 ml of solvent and centrifuged once again at 2000 rpm. The same process is repeated as the last step at 3000 rpm of centrifugation.

It is clear that the concentration obtained with this process is unknown and often is present residual solvent.

AFM imaging of 2D bP deposited by drop casting from a DMSO suspension onto a SiO2 substrate (Figure 5.1.4), shows significative morphological differences with respect to the 2D bP mechanically cleaved. The flakes obtained by liquid exfoliation have a more rounded shape and average lateral dimensions around 400 nm, lower than flakes obtained by mechanical exfoliation. In contrast, the average thickness of 2D bP flakes in this case results around 5nm, lower than that of flakes obtained by mechanical exfoliation.

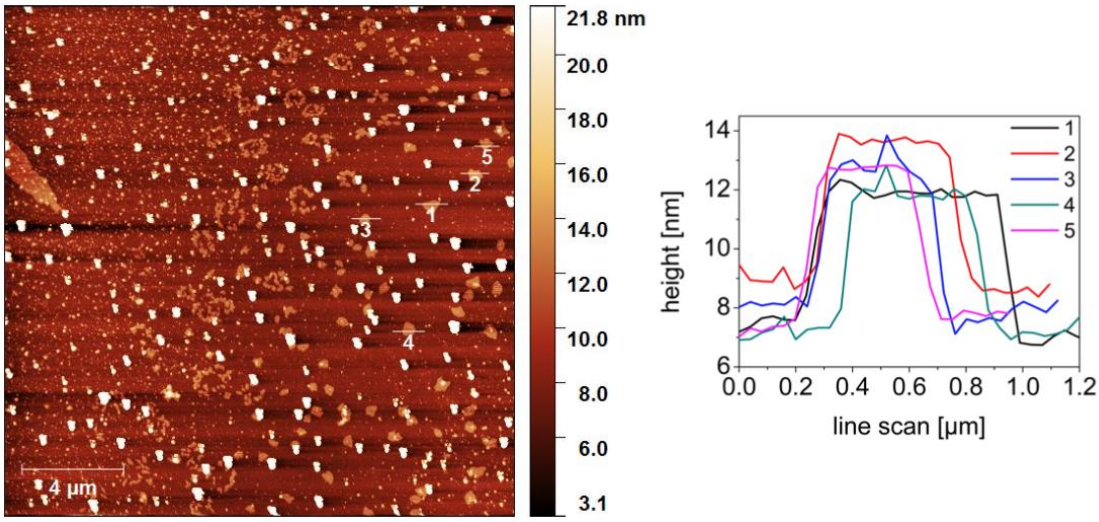

Figure 5.1.4. AFM image and related profiles of 2D bP flakes obtained by liquid exfoliation. 2D bP was deposited onto a SiO2 substrate by drop casting.

Electrospray deposition

This technique is based on the electrospray tool (ES), through which is possible to deposit materials with micrometric/nanometric control.

Its operating principles are related to the insertion of a solution or suspension inside an electrified capillary tube. Between this capillary tube, which pumps the liquid sample with a specific velocity, and the metallic support where the substrate is positioned, is applied a high-voltage bias. When the applied bias between the sample and the capillary tube reaches some kilovolts, the meniscus formed at the end of the capillary tube takes the shape of a cone, called “Taylor’s cone”. Thus, a thin wire of liquid is released from the tip of the cone, which successively is fragmented in a spray of highly charged drops.[269] This method was recently applied to realize tridimensional porous graphene electrodes.[136]

To deposit 2D bP flakes, a suspension of black phosphorus previously sonicated for 5 days and centrifugated at 400 rpm for 1h, it was inserted inside the capillary tube with an inner diameter of 200 µm. As the last step, a bias of 11-20 kV was applied between the tip and the metallic support, which were positioned at a distance of 15 cm from each other.

The unique characteristics of the deposited P_2O_5 nanoflakes are discussed in paragraph 2.4.

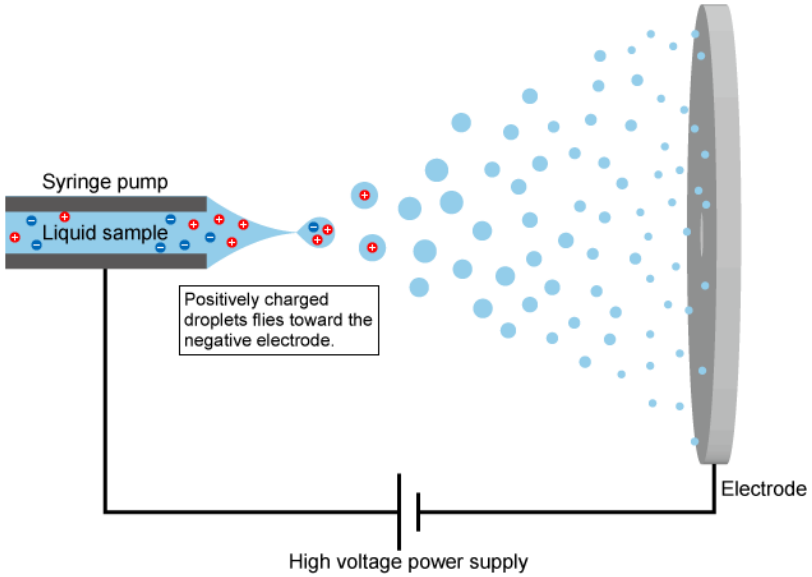

Figure 5.1.5. Schematic representation of the electrospray technique.

5.2 Spin-coating

The spin coating technique is a procedure to deposit uniform thin films to flat substrates. The solution of the material to be deposited is dispensed on the substrate, which is then rotated at high speed (Figure 5.2.1, step 1). When the spinning program is set to start, the spin-up stage begins and the spinning is accelerated until reaches a desired angular speed (ω), typically ranging from 300 to 10.000 rpm (Figure 5.2.1, step 2).

The spin process allows ejecting of most of the solution from the substrate immediately (Figure 5.2.1, step 3). Simultaneously, occurs the evaporation stage as the spinning induces an airflow that accelerates the evaporation of the solvent (Figure 5.2.1, step 4).[270]

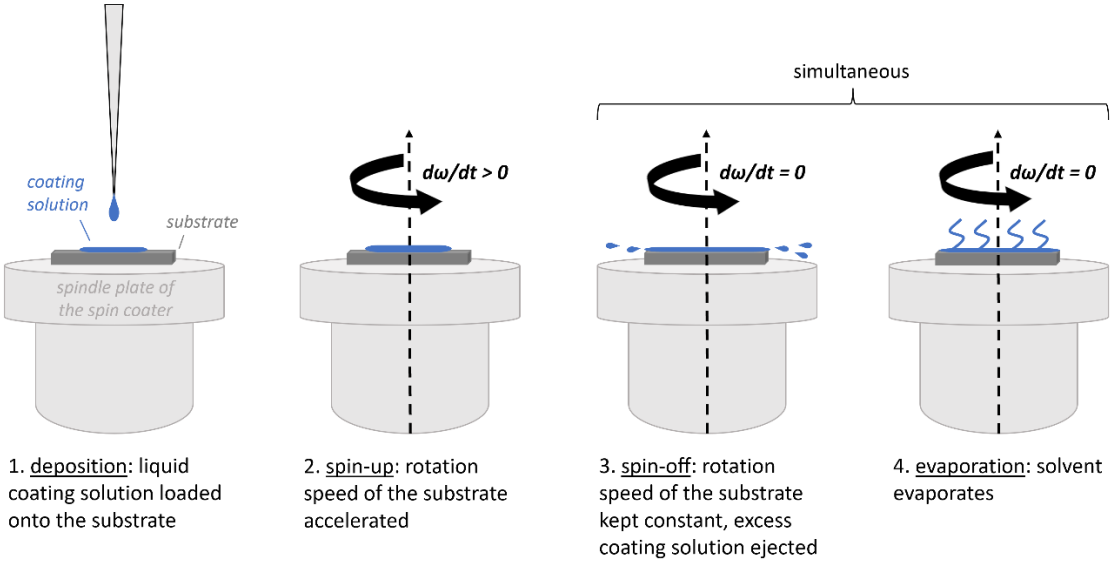

Figure 5.2.1. The four stages of the spin coating procedure. Figure by Sandra Hatakka, https://wiki.aalto.fi/display/SSC/Spin+coating

The total duration of the four stages is typically only less than one minute, which makes the spin coating technique a fast technique for thin film deposition.

From a physical point of view, the obtaining of highly uniform film is strictly linked to the balance between controlled centrifugal forces and viscous forces that are determined by solution viscosity (concentration). The centrifugal forces are regulated by the spin speed of the substrate (rpm). Hence, for the same concentration, it is possible to obtain thinner films by increasing the spin speed. Conversely, at a fixed spin speed, it is possible to obtain thinner films by diluting the solution. Since the solution begins to dry during stage 2 of the process, the acceleration of the substrate towards the final spin speed can affect the properties of the deposited film. The spin time does not significantly act on the thickness of the film.

Overall, spin coating represents a useful technique to process non-sublimable materials.

5.3 Atomic Force Microscopy (AFM)

Atomic force microscopy is a powerful analysis technique used to investigate the characteristics of surfaces. Generally, by scanning the surface of the sample it is possible to obtain high-resolution nanoscale images of the surface. In addition to the morphological ones, it is possible to also extrapolate information about mechanical, viscoelastic, electrical, and magnetic properties.

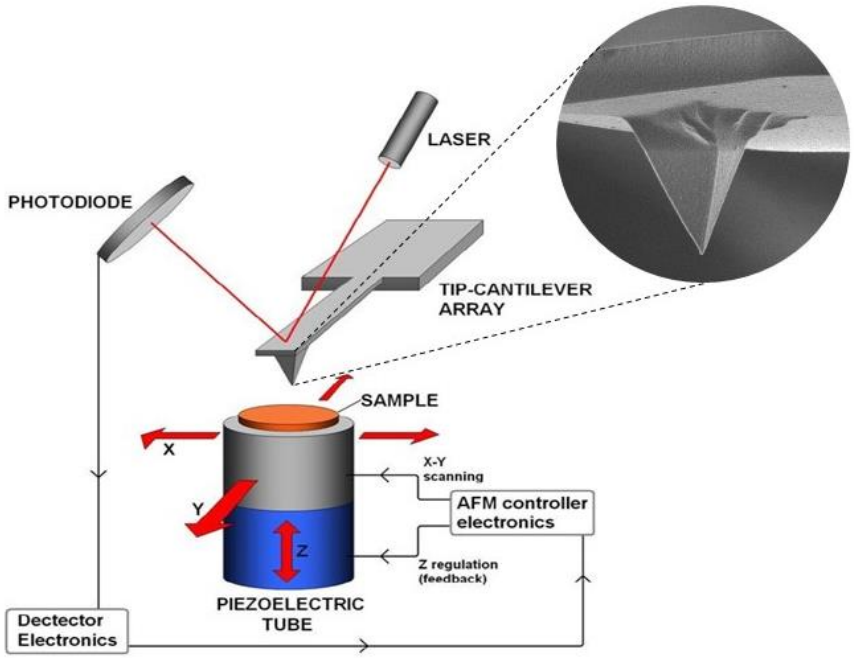

Figure 5.3.1. Schematic representation of the atomic force microscope and (inset) a scanning electron micrograph of a silicon cantilever with an integrated doped diamond coating tip.

The atomic force microscope is composed essentially of (i) a piezoelectric tube that serves as a *scanner*, on which is mounted the sample; (ii) the *probe* that interacts with the surface, which is composed of a cantilever with a known force constant, and a tip with a radius that ranges from 10 to 100 nm (Figure 5.3.1, inset); (iii) a *photodiode system* which reveals the movements of the cantilever through a laser reflex behind it (Figure 5.3.1).

The scanner oscillates the sample in the x-y axes. When the tip is located at interatomic distances from the surface, several interactions involving van der Waals, friction, adhesion, electrostatic, and magnetostatic forces are created. The resultant force causes a cantilever deflection, which is read by a laser pointed at the back of the cantilever and then by a photodiode system. The variations of the laser path activate a feedback circuit which provides to moves the sample on the z-axis in order to prevent tip-sample collisions.

The atomic force microscope can operate essentially in three different modes: *contact*, *non-contact*, and *tapping* mode (Figure 5.3.2). In *contact mode*, the feedback circuit maintains the tip and the sample in close contact distance (a few Å). The resultant force in this case will be repulsive and from the cantilever deflections can be obtained the topographic image.

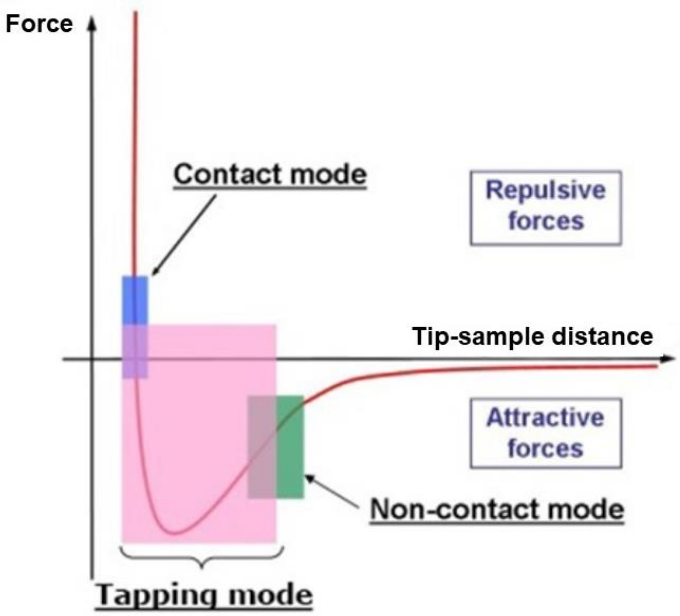

Figure 5.3.2. Working mode of an atomic force microscope.

In *non-contact* mode, the tip-sample distance ranges from 10 to 100 Å and consequently, the involved forces will be attractive. In this mode, the cantilever oscillates at a certain frequency, and the measured force is obtained from the frequency variations due to the interaction with the surface atoms.

In *tapping mode*, the cantilever oscillates at higher frequencies with respect to the *non-contact* mode. In this case, the interactions between the tip and the surface atoms change both the frequency and the amplitude of the oscillation. The amplitude variations are linked to the feedback circuit and then to the z-axis movement, which will move giving back the topographic information. The change in the frequency of oscillation indicates instead a change in the tip-sample interactions, and then a change of the nature of the material at the surface.

5.4 Optical microscopy

An optical microscope is a viewer tool that permits obtaining magnification as well as 1500x and 2000x, without and with oil immersion, respectively. In optical microscopy is generally used the visible light but is possible to also use UV-light by appropriate filters.

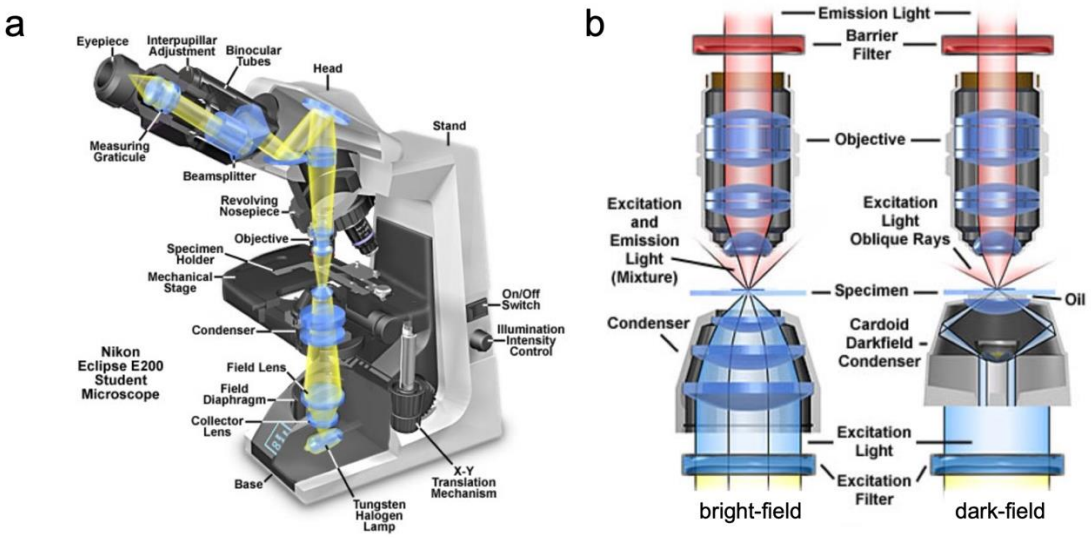

Figure 5.4.1. a) working principles of an optical microscope. b) bright- and dark-field optical microscopy schemes.

The optical analysis can be carried out by reflected light rather than transmitted light. The reflected light permits a higher accuracy level on the structure and the morphology of the examined sample. The light beam emitted from a tungsten halogen lamp is reflected by a mirror, a prism, or a polarizer crystal toward the specimen holder (Figure 5.4.1a).

The optical image can be acquired in *bright-field* or in *dark-field* illumination. In *bright-field* microscopy (Figure 5.4.1b, left) the light passes through perpendicular lenses with respect to the optical axis. The image contrast is obtained from significative variations of absorption and reflection of the flat surface. The light from the non-flat surface is deflected and appears dark in the image. This permits to indirectly reconstruct the microstructure.

The dark-field illumination produces the reverse contrast with respect to that generate in the bright-field illumination. While the light deflected from the non-flat zones is collected and appears bright in the image, the light from the flat surface does not contribute to the image formation. Hence, this technique is highly sensitive to surface irregularities such as grain boundaries, flowing lines, scratches, etc.

5.5 Thermal evaporation

In the last decades, thermal evaporation has largely expanded as a technique for obtaining thin films of organic semiconductors small molecule based.[152]

The advantages to use this technique are multiple. In fact, thermal evaporation provides to (i) control of the sub-monolayer thickness growth, (ii) an ultraclean environment with

a low level of contamination ensures by vacuum, and (iii) the possibility to drive a preferential growth modality acting on different control parameters.

On the other side, the drawbacks that afflict this technique are the high costs (turbomolecular pump, high vacuum chamber, etc.) and the impossibility to process materials with high molecular weight (i.e. polymers).

The core of the thermal evaporation technique consists of a vacuum chamber with a crucible (or more crucibles) and a substrate held perpendicularly to the crucible orifice (Figures 5.5.1a and b). The crucible is filled with the relative material and then is heated until the evaporation temperature. At this point, the material leaves the crucible as a molecular beam and impinges onto the substrate. According to the substrate temperature, the molecules can be adsorbed, desorbed, or diffuse to a nucleation center. In order to determine the evaporation rate and the thickness of deposited material, a quartz microbalance (or more) is placed near the substrate. Evaporation rate and substrate temperature are key parameters to modulate film morphology.[271]

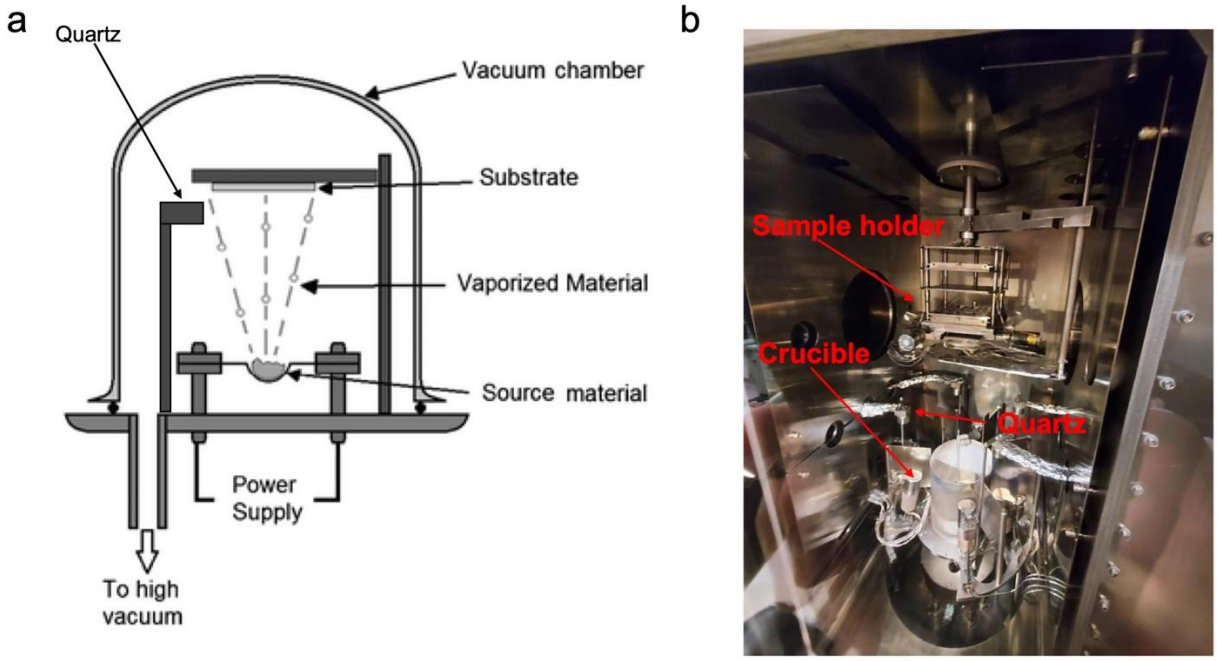

Figure 5.5.1 a) Schematic representation of a vacuum chamber for thermal sublimation of organic materials. b) inside of the evaporation chamber used in this thesis work (Kurt J. Lesker Spectros).

The evaporation system used in this thesis work is a commercial system produced by Kurt J. Lesker Company, the Spectros model. This system is characterized by 8 sources for organic materials and 3 for metal ones. The sample holder permits the simultaneous deposition onto 9 substrates with dimensions of 25x25mm. Together with the turbopump,

a cryopump is coupled in order to reach a high-vacuum base pressure of around 2 x 10^{-8} mbar.

The entire system is contained inside a glovebox and is coupled with a probe station, which permits the immediate optoelectronic characterization of the fabricated devices without any air exposure.

5.6 Optoelectronic device characterization

- **Probe station**

A Süss PM5 probe station (Figure 5.6.1), placed inside a glovebox, is used to electrically connect the devices. The connections are performed by using micrometric positioners connected to tungsten tips, through which is possible to apply a bias to the devices and measure very low currents in the order of the nA. On top of the measurements plane, is placed an optical microscope (magnification 70x) connected to an LCD screen, which allows the right placement of the tips on the device to characterize.

In addition, a photodiode is placed under the sample holder of the probe station to measure also the optical performances of the devices.

Figure 5.6.1. The Süss PM5 probe station used in this work.

- **Device analyzer**

An Agilent B1500A is used as a semiconductor device parameter analyzer (Figure 5.6.2). The analyzer is connected to the probe station through the glovebox by triaxial connections, in order to reduce the noise level in the range of pA. Every single connection

is entrusted to a single plug-in module, able to operate independently each another. Typically, transfer and output curves are performed using this tool. While transfer curves are performed by applying a fixed drain bias (V_{ds}) and sweeping the V_{gs} bias, output curves are obtained by operating in the opposite way (see paragraph 3.1). Together with the electrical characteristic, the electroluminescence of the devices is acquired by the photodiode placed under the chuck plate of the probe station.

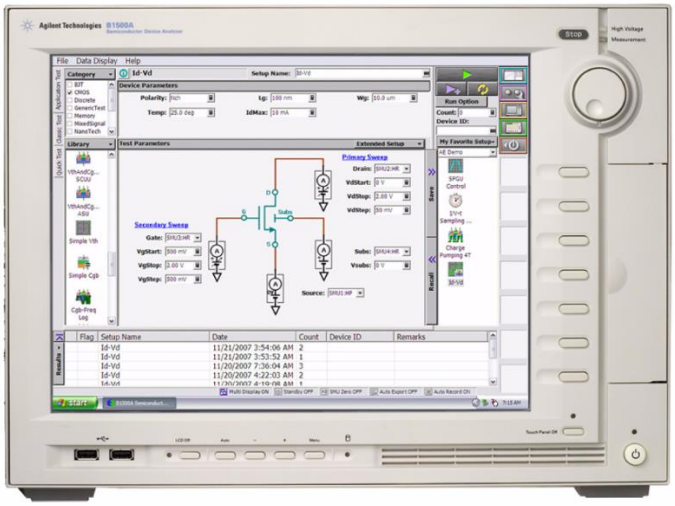

Figure 5.6.2 Agilent B1500A semiconductor device parameter analyzer.

- **Glovebox**

A glovebox is a sealed container designed to allow one to manipulate objects while being in a controlled atmosphere that is usually a very high-purity inert atmosphere (such as argon or nitrogen). Inert atmosphere gloveboxes are typically kept at a higher pressure than the surrounding environment, so any microscopic leaks are mostly leaking inert gas out of the box instead of letting air in. Several gloves are built into the sides of the glovebox, arranged in such a way that one can place his hands into them and be able to perform tasks inside the box without breaking the seal or allowing the potential injury to the worker.

The presence of a glovebox allows using and safe storing of highly oxygen-sensitive materials, usually organic dyes. In addition, the probe station placed inside permits immediate measure the fabricated devices without any oxygen exposure.

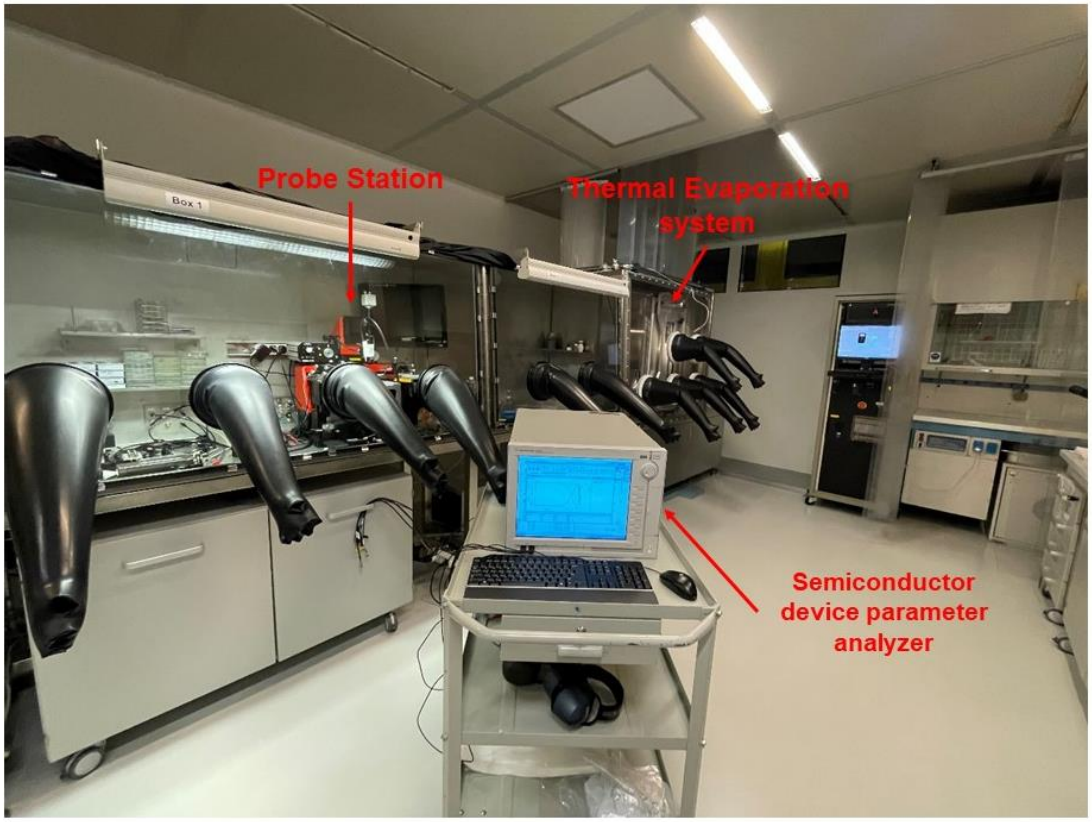

Figure 5.6.3. Picture of the glovebox containing, from the left, the probe station and the thermal evaporation system. In the foreground is the semiconductor device parameter analyzer.

Appendix A: Charge transport in molecular semiconductors

Conjugated molecules

Among the plethora of molecular materials, the core-conjugated molecules are particularly appealing for several properties such as the low-energy optical absorption, which coincides with the visible range. Since the optical band gap is small, this class of molecules has semiconductor behavior and can be defined as organic semiconductors molecules, to distinguish from the inorganic ones (Si, GaAs, etc).

To understand the behavior behind these properties is necessary to watch closely through the chemical bonds within these molecules, from the atomic to the molecular bonds.

Organic molecules are composed essentially of carbon atoms, whose ground state has the following electronic structure: $1s^2 2s^2 2p_x^1 2p_y^1$ (Figure A1).

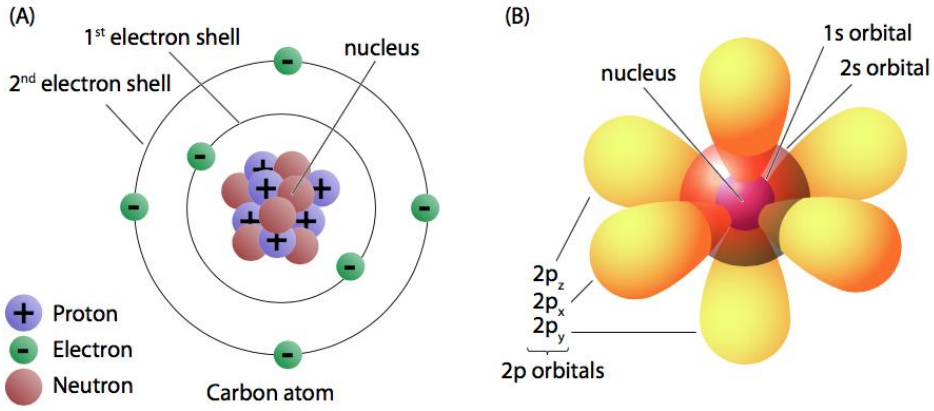

Figure A1. Electrons organization in shells and orbitals. a) representation of electronic shells of a carbon atom: in ground state, six electrons fill the electron shells to neutrally charge the carbon atom which contains six protons in the nucleus; b) representation of carbon atomic orbitals. The first shell contains only 1s orbital, while the second shell contains 2s and 2px, 2py, and 2pz orbitals, which are aligned along three orthogonal axes. Figure from Labxchange site is licensed under CC BY-NC-ND 4.0.

To understand the origin of the semiconducting behavior of organic molecules, it is necessary to consider the hybridization of sp^2 orbitals and presence of unhybridized $2p_z$ orbitals.

In particular, when two carbon atoms bond together, the hybrid atomic orbitals are mixed to form molecular orbitals, which are regulated by molecular orbital theory (MO) described in the next section. One of the two bonds formed between two hybridized orbitals is of σ type, in which is shared one pair of electrons and the electron density lie

between the nuclei (Figure A1a). The second bond, named π bond, is formed from the overlapping of the un-hybridized p_z orbital and is weaker than the highly directional σ bond (Figure A1b). Therefore, the double bonds consist of a σ and a π bond.

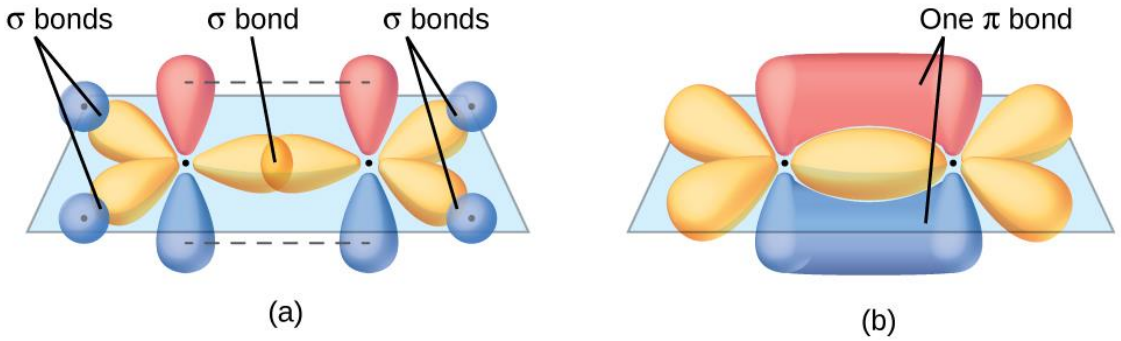

Figure A2. Representation of the simplest double-bond carbon molecule, the ethene (C2H4). a) σ bond between carbon atoms lies on the same plane and has electron density localized between nuclei; b) π bond is displayed as an electronic cloud above (red cloud) and below (blue cloud) the σ bond plane. Figure from Labxchange site is licensed under CC BY-NC-ND 4.0.

As is simple to see from Figure A1b, the electronic density in π bond is not confined between the nuclei, but rather forms a cloud above and below the plane of the σ bond, creating an electronic delocalization over the entire molecule. In real cases, this delocalization can be confined in only a part of the molecule,[272] in fact the conjugation largely determines the electron energy structure of the organic materials.

Overall, organic semiconductors are characterized by the electronic structure based on π-conjugated double bonds between carbon atoms, whose electrons delocalization in π-molecular orbitals is a key feature to allows injection, delocalization, and charge transport.

From single molecule to molecular solid

In general, the combination of two atomic orbitals generates two molecular orbitals, which specify the electronic configuration of the molecules. Since the combination of atomic orbitals on adjacent atoms can occur from different combinations of phases, the generated molecular orbitals have different energy levels. In the case of the combination of s atomic orbitals, the in-phase combination produces a molecular orbital with lower energy σ, defined as bonding orbital, and the out-phase addition produces a higher molecular orbital, σ^* defined as antibonding orbital.

By applying the same theory to the unhybridized p_z orbitals, which represent the key factor in the charge transport in conjugated molecules (see the previous section), two

molecular orbitals with different energy levels are obtained, π and π^* orbitals, respectively defined as bonding orbitals and antibonding orbitals.

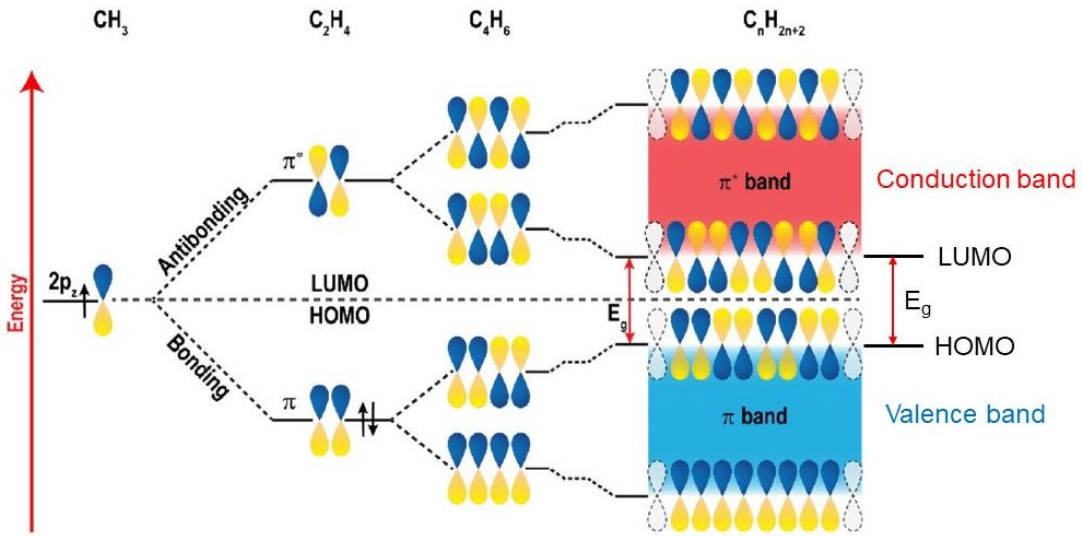

Figure A3. Energy band formation in function of the number of conjugated molecules. Figure by Kosala Wijeratne, PhD thesis "Conducting Polymer Electrodes for Thermogalvanic Cells" is licensed under CC BY-NC-ND 4.0.

The bonding orbitals, generated from in-phase combinations, are at the lowest energy and are shown in the lower part of Figure A3. In the contrast, the antibonding orbitals, in the higher part of the same Figure, are generated from the out-of-phase combinations and correspond to the highest energy orbitals. By increasing the length of the chain, the separation of energy levels between nearby orbitals vanishes and are formed continuous bands from π-orbitals and π^*-orbitals, called valence band and conduction band, respectively (Figure A3, blue and red bands). The energy gap (E_g) between the two bands is defined by the frontier orbitals of the valence and conduction bands, respectively named as the highest occupied molecular orbital (HOMO) and lowest unoccupied molecular orbital (LUMO). This energy gap, comparable with that of silicon or other inorganic materials, is the reason why organic conjugated materials were considered among the main substituent of their conventional inorganic counterparts.

Charge transport: bands regime and hopping regime comparison

The difference in energy between HOMO and HOMO-1 orbitals in isolated pentacene is 1.3 eV while the electronic coupling between the most strongly coupled molecules is 0.13 eV.[273] This confirms that when the conjugated molecules are organized in a crystalline structure, their molecular orbitals are only weakly perturbed by the neighboring

molecules. Hence, it is possible to consider only one HOMO or LUMO frontier molecular orbital depending on it considering electrons or holes transport.

By considering one-dimensional array of molecules with one state per molecule $|j\rangle$ corresponding to a frontier molecular orbital, each interacting with its nearest neighbors it is possible write the electronic Hamiltonian as:[274]

$$H_{\mathrm{el}} = \sum_{j} (\varepsilon |j\rangle\langle j| + \tau |j\rangle\langle j+1|)$$

where ε is the energy of the state and τ is the electronic coupling (also called hopping integral) between the localized molecular orbitals. This equation describes delocalized pure band states.

The dynamic of the charge transport is similar to the diffusion of a gas particle which periodically collides with other particles and is described by the semiclassical Boltzmann equation.[275] If the charge carriers in the band have effective mass of m^*, t_S is the average time between two collisions, and e is the electron charge, it is possible to define the μ mobility as:

$$\mu = e\, t_S / m^*$$

known as Drude model.[276]

Considering that the frequency of scattering increases with the temperature increase, the average time t_S decreases, and then also the mobility decreases with the temperature increase. This is considered the distinctive sign of band-like transport, in which the repulsive interaction between the carriers is ignored.

Unlike considered by Drude, the scattering centers are not the other electrons but are mainly constituted by phonons, i.e., lattice vibrations initiated by thermal excitations.

Polaron and polaronic band

Over the electronic coupling considered in the previous paragraph and described by the Hamiltonian H_{el}, it is necessary to consider other factors to deeply understand the charge transport in organic materials.

One of the factors to take into account is the nuclear motions, which can be described, considering just a single nuclear mode for simplicity, by the Hamiltonian:

$$H_{\text{nucl}} = \sum_j \frac{\hbar\omega}{2}(q_j^2 + p_j^2)$$

where q_j and p_j are the adimensional displacement and momentum on molecule j.

Since that if one adds or removes an electron, the equilibrium geometry of the molecule is modified, it is necessary to considerate the electron-nuclei interaction described by the Hamiltonian:

$$H_{\text{el-nucl}} = g\hbar\omega \sum_j q_j |j\rangle\langle j|$$

and also called *local electron-phonon* coupling, by virtue of that the generated deformation originated from the electron addition/remotion in the molecule is called *phonon*.

In the $H_{\text{el-nucl}}$ equation, the g term is a parameter that quantifies the strength of the electron-phonon coupling and its meaning is very simple and intuitive observing the oscillator model in Figure A4. When on j site there is not electron density, the oscillator q_j oscillates around the equilibrium position $q_j^{\text{eq}} = 0$. Conversely, if the electron density is all on site j, the oscillation moves from the equilibrium position to $q_i^{\text{eq}} = -g$, where the minimum of energy is reduced by $g^2\hbar\omega/2$, resulting in an extra stabilization due to the geometry relaxation because the site is charged.

At this point, is possible to describe the system in its entirety by the total Hamiltonian:

$$H = H_{\text{el}} + H_{\text{nucl}} + H_{\text{el-nucl}}$$

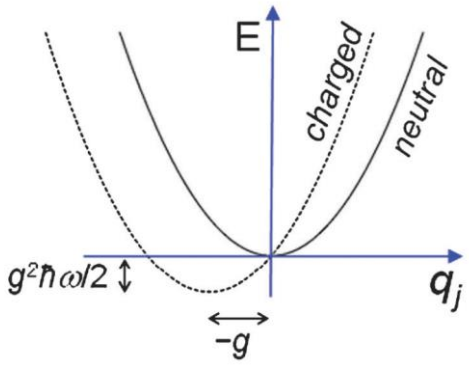

Figure A4. The addition/removal of an electron on molecule j changes the equilibrium geometry and energy. Here is represented a system with only one degree of freedom per molecule. Figure by A. Troisi, Chem. Soc. Rev., 2011, 40, 2347 is licensed under CC BY-NC-ND 4.0.

As discussed below, the charge modifications in a molecule determine a variation in its geometry (phonon). When a charge propagates through the lattice carry with itself the deformation of the surrounding molecules. This deformation is called *polaron*.
Since the polaron is delocalized and the system has translational symmetry, it is possible to describe the polaron states by a band and assume that their propagation is similar to the carrier propagation in a band (Figure A5).

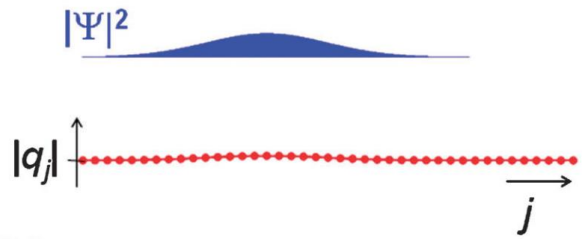

Figure A5. Polaronic band model. The carrier wavefunction is delocalized over many molecules and its propagation occurs together with a small deformation of the lattice. Figure by A. Troisi, Chem. Soc. Rev., 2011, 40, 2347 is licensed under CC BY-NC-ND 4.0.

Similar to the equation describing the electron states (Hel), the polaronic states can be described by the Hamiltonian:

$$H_{\text{polaron}} = \sum_j (\varepsilon' |j\rangle\langle j| + \tau' |j\rangle\langle j+1|)$$

where the states $|j\rangle$ in this equation also contain a part of the nuclear Hamiltonian and then describe the charge with the associated deformations. The transfer integral τ' is different from those of the simple electronic band because depends on the temperature:

$$\tau' = \tau e^{-\frac{1}{2}g^2(N_\omega + \frac{1}{2})}$$

with $N_\omega = [\exp(\hbar\omega/k_B T)-1]^{-1}$.
It is possible to see that at increasing temperatures the effective integral decreases and the effective mass increases correspondingly.

Small polaron hopping

Continued to temperature increasing, the transfer integral τ' tends to zero ($\tau' \rightarrow 0$), the polaronic band becomes of vanishing width and the effective mass becomes infinite.
This situation corresponds to molecules arranged in a lattice but not interacting from one another because of the huge mass. Hence, it is more convenient to describe the carrier

wavefunction as localized on a single molecule rather than use delocalized description. So, if is considered a system containing only two sites (1 and 2) with ε = 0, the charge carrier and its associated deformation can be described as:

$$H_{two-sites} = H_{nucl} + g\hbar\omega q_1|1\rangle\langle 1| + g\hbar\omega q_2|2\rangle\langle 2| + \tau(|1\rangle\langle 2| + |2\rangle\langle 1|)$$

The charge hopping from one site to another can be seen as a chemical reaction with characteristics reaction coordinate and rate constant k_{hop}.

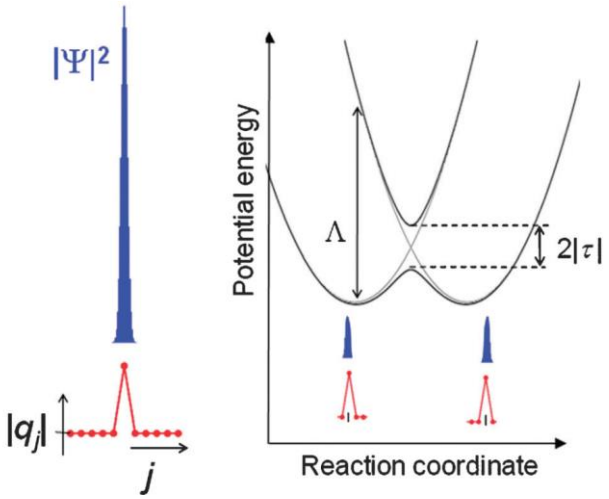

Figure A5. The potential energy curve for the hopping process between two molecular sites is determined by the parameters Λ and τ. Figure by A. Troisi, Chem. Soc. Rev., 2011, 40, 2347 is licensed under CC BY-NC-ND 4.0.

Looking at the Figure A4, is it possible assume that in the initial state the carrier is localized in the site 1 and the equilibrium positions of the oscillator are $q_1^{eq} = -g$ and $q_2^{eq} = 0$. When the carrier has hopped from site 1 to site 2, the equilibrium position of the oscillator will be inverted, $q_1^{eq} = 0$ and $q_2^{eq} = -g$.

Both curves are integrated in the Born-Oppenheimer (or adiabatic) potential energy curves in Figure A5. When the value of τ is sufficiently large the reaction proceeds *adiabatically* on the lowest potential energy curve. Conversely, if τ is small if enough to allow the transition, the transfer is called *non-adiabatic* and is described in the diabatic limit using a very simple expression valid in the high temperature:

$$k_{\mathrm{DIAB}} = \frac{\tau^2}{\hbar}\left(\frac{\pi}{k_{\mathrm{B}}T\Lambda}\right)^{1/2} e^{-\Lambda/4k_{\mathrm{B}}T}$$

where $\Lambda = 2g^2\hbar\omega$ is the reorganization energy which represents the energy released upon geometric changes in the two molecules after the electron transfer (electron-vibration coupling).

The obtained equation is identical to the Marcus[277] equation for the energy transfer and confirms that if the small polaron is formed, the transport is thermally activated. So, in the small polaron theory the mobility increases with the increasing temperature, contrary to the polaronic band theory.

Quantum corrections, dynamic disorder and molecular defects

Since the polaronic band model is valid at low temperatures and the small polaron model is valid at high temperatures ($k_BT \gg \hbar\omega$), there is a range of temperatures where a transition between those two regimes takes place.

The molecular vibrations are treated classically, but the involved degrees of freedom are mainly composed of bond stretching motions, then is necessary to add the quantum mechanical treatment.

The in-depth analysis of the quantum mechanical treatment will not be examined in this thesis for the sake of brevity but it is possible to summarize some crucial points about that: (i) while in the harmonic approximation the zero-point energy corresponds to $\frac{1}{2}\hbar\omega$ to the energy of the ground, with the quantum mechanical treatment the zero-point energy can be larger than the reaction barrier which also would make the hopping rate undefine; (ii) the small polaron is not formed if the reorganization energy is smaller than twice the intermolecular coupling; (iii) also when the small polaron is formed, the hopping between sites is still in adiabatic regime because of the intermolecular coupling is often too strong to use a non-adiabatic expression like the Marcus one.

Further, the models examine perfect crystals and do not take into account several phenomena linked to the molecular order and defects within them contained that change the charge transport behavior.

In particular, the molecular dynamic approach asserts that the electronic Hamiltonian of a molecular crystal at room temperature is disordered: each molecule has a different coupling with its neighbor and the lattice periodicity is completely lost. In those systems, the wavefunction is localized because of the thermal motion together with the non-local electron-phonon coupling of low-frequency modes.

As a matter of fact, the coexistence of states localized by dynamic disorder and band states was observed.[278] The model illustrates how the charge transport mechanism in high-mobility organic semiconductors evolves from polaronic band transport to a regime where the mean free path is very short (mobility saturation) but there is no formation of a small polaron. This observation suggests a possible crossover region, governed by the dynamic disorder model, between the polaronic band transport and the localized transport.

In this context, there are experimental evidences of localized charge carrier states in pentacene,[279] probably ascribable to the presence of defects such as chemical contaminants from the synthesis and vacancies.

Overall, defects act as charge traps if electronic levels are within the band gap. On the contrary, they will simply act as scattering centers for the delocalized carriers. Then, trap states are localized states which are described by small polaron model. The macroscopic electrical characteristics of real molecular semiconductors (containing defects) can be described in terms of mobility edge models, where carriers below a certain energy threshold do not contribute to transport and above that energy threshold they behave as in the ultrapure material.[280]

The studies of the points of defects are particularly useful to understand the behavior of the charge carrier in real systems such as the transistor devices herein presented, where is crucial to understand the behavior of charge carriers at the defects between grain boundaries of polycrystalline samples or between the organic materials and the dielectric gate.[281]

Bibliography

[1] Y. Zhu, X. Wu, *Prog. Mater. Sci.* **2023**, *131*, 101019.

[2] S. Suresh, *Science (80-.).* **2001**, *292*, 2447.

[3] A. Miserez, T. Schneberk, C. Sun, F. W. Zok, J. H. Waite, *Science (80-.).* **2008**, *319*, 1816.

[4] H. D. Espinosa, J. E. Rim, F. Barthelat, M. J. Buehler, H. D. Espinosa, *Prog. Mater. Sci.* **2009**, *54*, 1059.

[5] K. F. Chung, W. K. Yu, *Eng. Struct.* **2002**, *24*, 429.

[6] A. Dasgupta, X. Yang, J. Gao, *npj 2D Mater. Appl.* **2021**, *5*, DOI 10.1038/s41699-021-00271-8.

[7] K. S. Novoselov, A. K. Geim, S. V. Morozov, D. Jiang, Y. Zhang, S. V. Dubonos, I. V. Grigorieva, A. A. Firsov, *Science (80-.).* **2004**, *306*, 666.

[8] A. K. Geim, K. S. Novoselov, *Nat. Mater. 2007 63* **2007**, *6*, 183.

[9] A. A. Balandin, S. Ghosh, W. Bao, I. Calizo, D. Teweldebrhan, F. Miao, C. N. Lau, *Nano Lett.* **2008**, *8*, 902.

[10] M. D. Stoller, S. Park, Z. Yanwu, J. An, R. S. Ruoff, *Nano Lett.* **2008**, *8*, 3498.

[11] R. R. Nair, P. Blake, A. N. Grigorenko, K. S. Novoselov, T. J. Booth, T. Stauber, N. M. R. Peres, A. K. Geim, *Science (80-.).* **2008**, *320*, 1308.

[12] J. Zhang, Y. Chen, X. Wang, *Energy Environ. Sci.* **2015**, *8*, 3092.

[13] W. J. Ong, L. L. Tan, Y. H. Ng, S. T. Yong, S. P. Chai, *Chem. Rev.* **2016**, *116*, 7159.

[14] C. Zhi, Y. Bando, C. Tang, H. Kuwahara, D. Golberg, *Adv. Mater.* **2009**, *21*, 2889.

[15] Y. Lin, T. V. Williams, J. W. Connell, *J. Phys. Chem. Lett.* **2010**, *1*, 277.

[16] Q. Weng, X. Wang, X. Wang, Y. Bando, D. Golberg, *Chem. Soc. Rev.* **2016**, *45*, 3989.

[17] L. H. Li, Y. Chen, *Adv. Funct. Mater.* **2016**, *26*, 2594.

[18] C. Tan, H. Zhang, *Chem. Soc. Rev.* **2015**, *44*, 2713.

[19] M. Chhowalla, H. S. Shin, G. Eda, L. J. Li, K. P. Loh, H. Zhang, *Nat. Chem. 2013 54* **2013**, *5*, 263.

[20] X. Huang, Z. Zeng, H. Zhang, *Chem. Soc. Rev.* **2013**, *42*, 1934.

[21] R. Lv, J. A. Robinson, R. E. Schaak, D. Sun, Y. Sun, T. E. Mallouk, M. Terrones, *Acc. Chem. Res.* **2015**, *48*, 56.

[22] M. Osada, T. Sasaki, *J. Mater. Chem.* **2009**, *19*, 2503.

[23] R. Ma, T. Sasaki, *Acc. Chem. Res.* **2015**, *48*, 136.

[24] M. Naguib, V. N. Mochalin, M. W. Barsoum, Y. Gogotsi, *Adv. Mater.* **2014**, *26*, 992.

[25] J. W. Colson, A. R. Woll, A. Mukherjee, M. P. Levendorf, E. L. Spitler, V. B. Shields, M. G. Spencer, J. Park, W. R. Dichtel, *Science (80-.).* **2011**, *332*, 228.

[26] Y. Peng, Y. Li, Y. Ban, H. Jin, W. Jiao, X. Liu, W. Yang, *Science (80-.).* **2014**, *346*, 1356.

[27] T. Rodenas, I. Luz, G. Prieto, B. Seoane, H. Miro, A. Corma, F. Kapteijn, F. X. Llabrés I Xamena, J. Gascon, *Nat. Mater.* **2015**, *14*, 48.

[28] Q. Lu, M. Zhao, J. Chen, B. Chen, C. Tan, X. Zhang, Y. Huang, J. Yang, F. Cao, Y. Yu, J. Ping, Z. Zhang, X. J. Wu, H. Zhang, *Small* **2016**, *12*, 4669.

[29] Z. Fan, X. Huang, C. Tan, H. Zhang, *Chem. Sci.* **2014**, *6*, 95.

[30] J. Niu, D. Wang, H. Qin, X. Xiong, P. Tan, Y. Li, R. Liu, X. Lu, J. Wu, T. Zhang, W. Ni, J. Jin, *Nat. Commun. 2014 51* **2014**, *5*, 1.

[31] X. Huang, S. Tang, X. Mu, Y. Dai, G. Chen, Z. Zhou, F. Ruan, Z. Yang, N. Zheng, *Nat. Nanotechnol.* **2011**, *6*, 28.

[32] H. Duan, N. Yan, R. Yu, C. R. Chang, G. Zhou, H. S. Hu, H. Rong, Z. Niu, J. Mao, H. Asakura, T. Tanaka, P. J. Dyson, J. Li, Y. Li, *Nat. Commun. 2014 51* **2014**, *5*, 1.

[33] P. Kissel, D. J. Murray, W. J. Wulftange, V. J. Catalano, B. T. King, *Nat. Chem.* **2014**, *6*, 774.

[34] M. J. Kory, M. Wörle, T. Weber, P. Payamyar, S. W. Van De Poll, J. Dshemuchadse, N. Trapp, A. D. Schlüter, *Nat. Chem.* **2014**, *6*, 779.

[35] C. Tan, X. Qi, X. Huang, J. Yang, B. Zheng, Z. An, R. Chen, J. Wei, B. Z. Tang, W. Huang, H. Zhang, *Adv. Mater.* **2014**, *26*, 1735.

[36] S.-L. Cai, W.-G. Zhang, R. N. Zuckermann, Z.-T. Li, X. Zhao, Y. Liu, S.-L. Cai, R. N. Zuckermann, Y. Liu, S.-L. W. Cai, G. Zhang, Z.-T. Li, X. Zhao, **2015**, DOI 10.1002/adma.201500124.

[37] J. Shamsi, Z. Dang, P. Bianchini, C. Canale, F. Di Stasio, R. Brescia, M. Prato, L. Manna, *J. Am. Chem. Soc.* **2016**, *138*, 7240.

[38] J. Song, L. Xu, J. Li, J. Xue, Y. Dong, X. Li, H. Zeng, *Adv. Mater.* **2016**, *28*, 4861.

[39] L. Dou, A. B. Wong, Y. Yu, M. Lai, N. Kornienko, S. W. Eaton, A. Fu, C. G.

Bischak, J. Ma, T. Ding, N. S. Ginsberg, L. W. Wang, A. P. Alivisatos, P. Yang, *Science* **2015**, *349*, 1518.

[40] J. Liu, Y. Xue, Z. Wang, Z. Q. Xu, C. Zheng, B. Weber, J. Song, Y. Wang, Y. Lu, Y. Zhang, Q. Bao, *ACS Nano* **2016**, *10*, 3536.

[41] A. D. Franklin, *Science (80-.).* **2015**, *349*, DOI 10.1126/science.aab2750.

[42] M. Qiu, A. Singh, D. Wang, J. Qu, M. Swihart, H. Zhang, P. N. Prasad, *Nano Today* **2019**, *25*, 135.

[43] J. D. Cressler, *Silicon Heterostructure Handbook*, Boca Raton, **2005**.

[44] S. Thompson, N. Anand, M. Armstrong, C. Auth, B. Arcot, M. Alavi, P. Bai, J. Bielefeld, R. Bigwood, J. Brandenburg, M. Buehler, S. Cea, V. Chikarmane, C. Choi, R. Frankovic, T. Ghani, G. Glass, W. Han, T. Hoffmann, M. Hussein, P. Jacob, A. Jain, C. Jan, S. Joshi, C. Kenyon, J. Klaus, S. Klopcic, J. Luce, Z. Ma, B. McIntyre, K. Mistry, A. Murthy, P. Nguyen, H. Pearson, T. Sandford, R. Schweinfurth, R. Shaheed, S. Sivakumar, M. Taylor, B. Tufts, C. Wallace, P. Wang, C. Weber, M. Bohr, *Tech. Dig. - Int. Electron Devices Meet.* **2002**, 61.

[45] K. Petermann, A. Splett, B. Schüppert, H. Kibbel, H.-J. Herzog, E. Kasper, *Integr. Photonics Res. (1992), Pap. TuA4* **1992**, TuA4.

[46] M. Y. Liu, S. Y. Chou, S. Alexandrou, T. Y. Hsiang, *Ultrafast Electron. Optoelectron. (1993), Pap. A13* **1993**, A13.

[47] B. Jalali, L. Naval, A. F. J. Levi, P. G. Watson, *https://doi.org/10.1117/12.142080* **1993**, *1804*, 94.

[48] V. P. Kesan, P. G. May, E. Bassous, S. S. Iyer, *Tech. Dig. - Int. Electron Devices Meet.* **1990**, 637.

[49] D.-X. Xu, S. Janz, H. Lafontaine, M. R. T. Pearson, *https://doi.org/10.1117/12.342801* **1999**, *3630*, 50.

[50] S. K. Moore, *IEEE Spectr.* **2019**, *56*, 09.

[51] E. Mollick, *IEEE Ann. Hist. Comput.* **2006**, *28*, 62.

[52] S. T. Picraux, "Epitaxy," can be found under https://www.britannica.com/science/epitaxy, **2014**.

[53] H. Sirringhaus, *Adv. Mater.* **2014**, *26*, 1319.

[54] J. Zaumseil, *Adv. Funct. Mater.* **2020**, *30*, DOI 10.1002/adfm.201905269.

[55] M. Prosa, M. Bolognesi, L. Fornasari, G. Grasso, L. Lopez-Sanchez, F. Marabelli, S. Toffanin, *Nanostructured Organic/Hybrid Materials and Components in Miniaturized Optical and Chemical Sensors*, **2020**.

[56] Y. Huang, E. L. Hsiang, M. Y. Deng, S. T. Wu, *Light Sci. Appl. 2020 91* **2020**, *9*, 1.

[57] R. P. Xu, Y. Q. Li, J. X. Tang, *J. Mater. Chem. C* **2016**, *4*, 9116.

[58] A. Salehi, X. Fu, D. H. Shin, F. So, *Adv. Funct. Mater.* **2019**, *29*, 1808803.

[59] S. Takagi, T. Mizuno, T. Tezuka, N. Sugiyama, T. Numata, K. Usuda, Y. Moriyama, S. Nakaharai, J. Koga, A. Tanabe, N. Hirashita, T. Maeda, *Tech. Dig. - Int. Electron Devices Meet.* **2003**, 57.

[60] C. N. Chléirigh, N. D. Theodore, H. Fukuyama, S. Mure, H. U. Ehrke, A. Domenicucci, J. L. Hoyt, *IEEE Trans. Electron Devices* **2008**, *55*, 2687.

[61] M. Peruzzini, R. Bini, M. Bolognesi, M. Caporali, M. Ceppatelli, F. Cicogna, S. Coiai, S. Heun, A. Ienco, I. I. Benito, A. Kumar, G. Manca, E. Passaglia, D. Scelta, M. Serrano-Ruiz, F. Telesio, S. Toffanin, M. Vanni, *Eur. J. Inorg. Chem.* **2019**, *2019*, 1476.

[62] F. Xia, H. Wang, Y. Jia, *Nat. Commun.* **2014**, *5*, 1.

[63] S. Lee, F. Yang, J. Suh, S. Yang, Y. Lee, G. Li, H. S. Choe, A. Suslu, Y. Chen, C. Ko, J. Park, K. Liu, J. Li, K. Hippalgaonkar, J. J. Urban, S. Tongay, J. Wu, *Nat. Commun.* **2015**, *6*, 1.

[64] N. Hemsworth, V. Tayari, F. Telesio, S. Xiang, S. Roddaro, M. Caporali, A. Ienco, M. Serrano-Ruiz, M. Peruzzini, G. Gervais, T. Szkopek, S. Heun, *Phys. Rev. B* **2016**, *94*, 245404.

[65] L. Kou, C. Chen, S. C. Smith, *J. Phys. Chem. Lett.* **2015**, *6*, 2794.

[66] L. Li, Y. Yu, G. J. Ye, Q. Ge, X. Ou, H. Wu, D. Feng, X. H. Chen, Y. Zhang, *Nat. Nanotechnol.* **2014**, *9*, 372.

[67] H. Liu, A. T. Neal, Z. Zhu, Z. Luo, X. Xu, D. Tománek, P. D. Ye, *ACS Nano* **2014**, *8*, 4033.

[68] X. Wang, A. M. Jones, K. L. Seyler, V. Tran, Y. Jia, H. Zhao, H. Wang, L. Yang, X. Xu, F. Xia, *Nat. Nanotechnol.* **2015**, *10*, 517.

[69] X. Zhu, T. Zhang, Z. Sun, H. Chen, J. Guan, X. Chen, H. Ji, P. Du, S. Yang, *Adv. Mater.* **2017**, *29*, 1605776.

[70] A. Patra, *PEARSON* **2012**.

[71] M. Serrano-Ruiz, M. Caporali, A. Ienco, V. Piazza, S. Heun, M. Peruzzini, *Adv. Mater. Interfaces* **2016**, *3*, 2.

[72] J. Kang, J. D. Wood, S. A. Wells, J. H. Lee, X. Liu, K. S. Chen, M. C. Hersam, *ACS Nano* **2015**, *9*, 3596.

[73] P. Yasaei, B. Kumar, T. Foroozan, C. Wang, M. Asadi, D. Tuschel, J. E. Indacochea, R. F. Klie, A. Salehi-Khojin, *Adv. Mater.* **2015**, *27*, 1887.

[74] A. H. Woomer, T. W. Farnsworth, J. Hu, R. A. Wells, C. L. Donley, S. C. Warren, *ACS Nano* **2015**, *9*, 8869.

[75] Z. Guo, H. Zhang, S. Lu, Z. Wang, S. Tang, J. Shao, Z. Sun, H. Xie, H. Wang, X. F. Yu, P. K. Chu, *Adv. Funct. Mater.* **2015**, *25*, 6996.

[76] Z. Sun, H. Xie, S. Tang, X. F. Yu, Z. Guo, J. Shao, H. Zhang, H. Huang, H. Wang, P. K. Chu, *Angew. Chemie - Int. Ed.* **2015**, *54*, 11526.

[77] J. Guan, Z. Zhu, D. Tománek, *Phys. Rev. Lett.* **2014**, *113*, 226801.

[78] V. Tran, R. Soklaski, Y. Liang, L. Yang, *Phys. Rev. B - Condens. Matter Mater. Phys.* **2014**, *89*, 235319.

[79] V. Sresht, A. A. H. Pádua, D. Blankschtein, *ACS Nano* **2015**, *9*, 8255.

[80] W. Lu, H. Nan, J. Hong, Y. Chen, C. Zhu, Z. Liang, X. Ma, Z. Ni, C. Jin, Z. Zhang, *Nano Res.* **2014**, *7*, 853.

[81] V. Nicolosi, M. Chhowalla, M. G. Kanatzidis, M. S. Strano, J. N. Coleman, *Science (80-.).* **2013**, *340*, 1226419.

[82] M. Masjedi-Arani, D. Ghanbari, M. Salavati-Niasari, S. Bagheri, *J. Clust. Sci.* **2016**, *27*, 39.

[83] J. O. Island, G. A. Steele, H. S. J. Van Der Zant, A. Castellanos-Gomez, *2D Mater.* **2015**, *2*, 011002.

[84] J. Pei, X. Gai, J. Yang, X. Wang, Z. Yu, D. Y. Choi, B. Luther-Davies, Y. Lu, *Nat. Commun.* **2016**, *7*, 1.

[85] F. Telesio, E. Passaglia, F. Cicogna, F. Costantino, M. Serrano-Ruiz, M. Peruzzini, S. Heun, *Nanotechnology* **2018**, *29*, 295601.

[86] E. Passaglia, F. Cicogna, G. Lorenzetti, S. Legnaioli, M. Caporali, M. Serrano-Ruiz, A. Ienco, M. Peruzzini, *RSC Adv.* **2016**, *6*, 53777.

[87] J. D. Wood, S. A. Wells, D. Jariwala, K. S. Chen, E. Cho, V. K. Sangwan, X. Liu, L. J. Lauhon, T. J. Marks, M. C. Hersam, *Nano Lett.* **2014**, *14*, 6964.

[88] C. R. Ryder, J. D. Wood, S. A. Wells, Y. Yang, D. Jariwala, T. J. Marks, G. C. Schatz, M. C. Hersam, *Nat. Chem.* **2016**, *8*, 597.

[89] M. Bolognesi, M. Brucale, A. Lorenzoni, F. Prescimone, S. Moschetto, V. V. Korolkov, M. Baldoni, M. Serrano-Ruiz, M. Caporali, F. Mercuri, E. Besley, M. Muccini, M. Peruzzini, P. H. Beton, S. Toffanin, *Nanoscale* **2019**, *11*, 17252.

[90] A. Facchetti, T. J. Marks, *Sigma-Aldrich Mater. Matters* **2009**, *4*, 64.

[91] W. W. A. Koopman, S. Toffanin, M. Natali, S. Troisi, R. Capelli, V. Biondo, A. Stefani, M. Muccini, *Nano Lett.* **2014**, *14*, 1695.

[92] Z. Yatabe, J. T. Asubar, T. Hashizume, *J. Phys. D. Appl. Phys.* **2016**, *49*, 393001.

[93] T. H. Hung, M. Esposto, S. Rajan, *Appl. Phys. Lett.* **2011**, *99*, 162104.

[94] A. R. Gerson, S. C. Nyburg, *urn:issn:0108-7681* **1992**, *48*, 737.

[95] V. V. Korolkov, I. G. Timokhin, R. Haubrichs, E. F. Smith, L. Yang, S. Yang, N. R. Champness, M. Schröder, P. H. Beton, *Nat. Commun.* **2017**, *8*, 1.

[96] C. Wang, D. Niu, B. Liu, S. Wang, X. Wei, Y. Liu, H. Xie, Y. Gao, *J. Phys. Chem. C* **2017**, *121*, 18084.

[97] P. Vishnoi, S. Rajesh, S. Manjunatha, A. Bandyopadhyay, M. Barua, S. K. Pati, C. N. R. Rao, *ChemPhysChem* **2017**, *18*, 2985.

[98] C. D. Zhang, J. C. Lian, W. Yi, Y. H. Jiang, L. W. Liu, H. Hu, W. D. Xiao, S. X. Du, L. L. Sun, H. J. Gao, *J. Phys. Chem. C* **2009**, *113*, 18823.

[99] M. Bolognesi, S. Moschetto, M. Trapani, F. Prescimone, C. Ferroni, G. Manca, A. Ienco, S. Borsacchi, M. Caporali, M. Muccini, M. Peruzzini, M. Serrano-Ruiz, L. Calucci, M. A. Castriciano, S. Toffanin, *ACS Appl. Mater. Interfaces* **2019**, *11*, 22637.

[100] T. M. Figueira-Duarte, K. Müllen, *Chem. Rev.* **2011**, *111*, 7260.

[101] M. Singh, M. Holzinger, O. Biloivan, S. Cosnier, *Carbon N. Y.* **2013**, *61*, 349.

[102] B. B. Craig, J. Kirk, M. A. J. Rodgers, *Chem. Phys. Lett.* **1977**, *49*, 437.

[103] G. v. Bünau, *Berichte der Bunsengesellschaft für Phys. Chemie* **1970**, *74*, 1294.

[104] S. L. Murov, I. Carmichael, G. L. Hug, *Handbook of Photochemistry*, New York, **1993**.

[105] T. Wang, N. Zhang, K. Zhang, J. Dai, W. Bai, R. Bai, *Chem. Commun.* **2016**, *52*, 9679.

[106] G. Abellán, S. Wild, V. Lloret, N. Scheuschner, R. Gillen, U. Mundloch, J. Maultzsch, M. Varela, F. Hauke, A. Hirsch, *J. Am. Chem. Soc.* **2017**, *139*, 10432.

[107] S. Moschetto, A. Ienco, G. Manca, M. Serrano-Ruiz, M. Peruzzini, A. Mezzi, M. Brucale, M. Bolognesi, S. Toffanin, *Dalt. Trans.* **2021**, *50*, 11610.

[108] J. Plutnar, Z. Sofer, M. Pumera, *ACS Nano* **2018**, *12*, 8390.

[109] A. Yang, D. Wang, X. Wang, D. Zhang, N. Koratkar, M. Rong, *Nano Today* **2018**, *20*, 13.

[110] C. J. An, Y. H. Kang, C. Lee, S. Y. Cho, *Adv. Funct. Mater.* **2018**, *28*, 1800532.

[111] J. Hu, Z. Guo, P. E. McWilliams, J. E. Darges, D. L. Druffel, A. M. Moran, S. C.

Warren, *Nano Lett.* **2016**, *16*, 74.

[112] M. Caporali, M. Serrano-Ruiz, F. Telesio, S. Heun, G. Nicotra, C. Spinella, M. Peruzzini, *Chem. Commun.* **2017**, *53*, 10946.

[113] D. Zhang, X. Lin, S. Lan, H. Sun, X. Wang, X. Liu, Y. Zhang, Y. Zeng, *Part. Part. Syst. Charact.* **2018**, *35*, 1800010.

[114] D. Huang, Z. Zhuang, Z. Wang, S. Li, H. Zhong, Z. Liu, Z. Guo, W. Zhang, *Appl. Surf. Sci.* **2019**, *497*, 143825.

[115] J. Wang, H. Zhang, X. Xiao, D. Liang, X. Liang, L. Mi, J. Wang, J. Liu, *Acta Biomater.* **2020**, *107*, 260.

[116] T. H. Lee, S. Y. Kim, H. W. Jang, *Nanomater. 2016, Vol. 6, Page 194* **2016**, *6*, 194.

[117] Q. Wu, M. Liang, S. Zhang, X. Liu, F. Wang, *Nanoscale* **2018**, *10*, 10428.

[118] J. W. Lee, S.-R. Choi, J. H. Heo, *Cite This ACS Appl. Mater. Interfaces* **2021**, *13*, 42311.

[119] T. Zhang, Z. Cheng, Y. Wang, Z. Li, C. Wang, Y. Li, Y. Fang, *Nano Lett.* **2010**, *10*, 4738.

[120] A. Ciesielski, S. Haar, M. El Gemayel, H. Yang, J. Clough, G. Melinte, M. Gobbi, E. Orgiu, M. V. Nardi, G. Ligorio, V. Palermo, N. Koch, O. Ersen, C. Casiraghi, P. Samorì, *Angew. Chemie* **2014**, *126*, 10523.

[121] S. Liu, N. Huo, S. Gan, Y. Li, Z. Wei, B. Huang, J. Liu, J. Li, H. Chen, *J. Mater. Chem. C* **2015**, *3*, 10974.

[122] J. Lin, L. Liang, X. Ling, S. Zhang, N. Mao, N. Zhang, B. G. Sumpter, V. Meunier, L. Tong, J. Zhang, *J. Am. Chem. Soc.* **2015**, *137*, 15511.

[123] Y. Feng, J. Zhou, Y. Du, F. Miao, C. G. Duan, B. Wang, X. Wan, *J. Phys. Condens. Matter* **2015**, *27*, 185302.

[124] H. Wu, X. Huang, M. Gao, X. Liao, B. Shi, *Green Chem.* **2011**, *13*, 651.

[125] V. Amendola, *Phys. Chem. Chem. Phys.* **2016**, *18*, 2230.

[126] G. T. Forcherio, D. K. Roper, *Adv. Opt. Mater.* **2016**, *4*, 1288.

[127] W. Luo, D. Y. Zemlyanov, C. A. Milligan, Y. Du, L. Yang, Y. Wu, P. D. Ye, *Nanotechnology* **2016**, *27*, DOI 10.1088/0957-4484/27/43/434002.

[128] S. Peters, S. Peredkov, M. Neeb, W. Eberhardt, M. Al-Hada, *Surf. Sci.* **2013**, *608*, 129.

[129] S. Moschetto, M. Bolognesi, F. Prescimone, M. Brucale, A. Mezzi, L. Ortolani, M. Caporali, P. Pingue, M. Serrano-Ruiz, D. Pisignano, M. Peruzzini, L. Persano,

S. Toffanin, *ACS Appl. Nano Mater.* **2021**, *4*, 3476.

[130] D. R. Dreyer, S. Park, C. W. Bielawski, R. S. Ruoff, *Chem. Soc. Rev.* **2010**, *39*, 228.

[131] W. Yu, L. Sisi, Y. Haiyan, L. Jie, *RSC Adv.* **2020**, *10*, 15328.

[132] H. Yin, G. P. Zheng, J. Gao, Y. Wang, Y. Ma, *Phys. Chem. Chem. Phys.* **2017**, *19*, 27508.

[133] H. J. Xiang, J. Yang, J. G. Hou, Q. Zhu, *Appl. Phys. Lett.* **2006**, *89*, 223111.

[134] M. N. Blonsky, H. L. Zhuang, A. K. Singh, R. G. Hennig, *ACS Nano* **2015**, *9*, 9885.

[135] M. M. Alyörük, *Phys. status solidi* **2016**, *253*, 2534.

[136] H. Tang, C. Yang, Z. Lin, Q. Yang, F. Kang, C. P. Wong, *Nanoscale* **2015**, *7*, 9133.

[137] K. Mahmood, A. Khalid, S. W. Ahmad, H. G. Qutab, M. Hameed, R. Sharif, *Sol. Energy* **2020**, *203*, 32.

[138] L. Chen, G. Zhou, Z. Liu, X. Ma, J. Chen, Z. Zhang, X. Ma, F. Li, H. M. Cheng, W. Ren, *Adv. Mater.* **2016**, *28*, 510.

[139] Z. Yan, X. He, L. She, J. Sun, R. Jiang, H. Xu, F. Shi, Z. Lei, Z. H. Liu, *J. Mater.* **2018**, *4*, 129.

[140] G. Wang, R. Pandey, S. P. Karna, *Nanoscale* **2014**, *7*, 524.

[141] F. Liu, L. You, K. L. Seyler, X. Li, P. Yu, J. Lin, X. Wang, J. Zhou, H. Wang, H. He, S. T. Pantelides, W. Zhou, P. Sharma, X. Xu, P. M. Ajayan, J. Wang, Z. Liu, *Nat. Commun.* **2016**, *7*, DOI 10.1038/NCOMMS12357.

[142] F. Xue, J. Zhang, W. Hu, W. T. Hsu, A. Han, S. F. Leung, J. K. Huang, Y. Wan, S. Liu, J. Zhang, J. H. He, W. H. Chang, Z. L. Wang, X. Zhang, L. J. Li, *ACS Nano* **2018**, *12*, 4976.

[143] A. N. Morozovska, S. V. Svechnikov, E. A. Eliseev, S. V. Kalinin, *Phys. Rev. B - Condens. Matter Mater. Phys.* **2007**, *76*, 054123.

[144] A. N. Morozovska, E. A. Eliseev, S. V. Kalinin, *J. Appl. Phys.* **2007**, *102*, 074105.

[145] J. Xu, X. Qiao, Y. Wang, Q. Sheng, T. Yue, J. Zheng, M. Zhou, *Mikrochim. Acta* **2019**, *186*, DOI 10.1007/S00604-019-3339-3.

[146] H. Zhao, W. Zhang, Z. Liu, D. Huang, W. Zhang, B. Ye, G. Hu, H. Zhong, Z. Zhuang, Z. Guo, *Nanophotonics* **2018**, *7*, 1651.

[147] S. Moschetto, F. Prescimone, M. Bolognesi, S. Toffanin, *Adv. Mater. Interfaces*

2022, DOI 10.1002/admi.202102149.

[148] S. E. Thompson, M. Armstrong, C. Auth, S. Cea, R. Chau, G. Glass, T. Hoffman, J. Klaus, Z. Ma, B. Mcintyre, A. Murthy, B. Obradovic, L. Shifren, S. Sivakumar, S. Tyagi, T. Ghani, K. Mistry, M. Bohr, Y. El-Mansy, *IEEE Electron Device Lett.* **2004**, *25*, 191.

[149] T. Ghani, M. Armstrong, C. Auth, M. Bost, P. Charvat, G. Glass, T. Hoffmann, K. Johnson, C. Kenyon, J. Klaus, B. Mcintyre, K. Mistry, A. Murthy, J. Sandford, M. Silberstein, S. Sivakumar, P. Smith, K. Zawadzki, S. Thompson, M. Bohr, **n.d.**

[150] K. Vaeth, "OLED and LED Thechnology - What's the Difference?," can be found under https://www.oledworks.com/news/blog/oled-and-led-technology-whats-the-difference/, **2020**.

[151] F. F. Vidor, T. Meyers, U. Hilleringmann, *Electron. 2015, Vol. 4, Pages 480-506* **2015**, *4*, 480.

[152] S. R. Forrest, *Nature* **2004**, *428*, 911.

[153] S. Y. Kim, K. Y. Kim, Y. H. Tak, J. L. Lee, *Appl. Phys. Lett.* **2006**, *89*, 132108.

[154] M. Schaer, F. Nüesch, D. Berner, W. Leo, L. Zuppiroli, *Adv. Funtional Mater.* **2001**, *11*, 116.

[155] P. E. Burrows, V. Bulovic, S. R. Forrest, L. S. Sapochak, D. M. McCarty, M. E. Thompson, *Appl. Phys. Lett.* **1998**, *65*, 2922.

[156] G. Gelinck, P. Heremans, K. Nomoto, T. D. Anthopoulos, *Adv. Mater.* **2010**, *22*, 3778.

[157] C. W. Tang, S. A. Vanslyke, *Appl. Phys. Lett.* **1998**, *51*, 913.

[158] N. M. Rada, G. E. Triplett, *Solid. State. Electron.* **2010**, *54*, 378.

[159] C. W. Tang, *Appl. Phys. Lett.* **1998**, *48*, 183.

[160] B. H. Lessard, *ACS Appl. Mater. Interfaces* **2021**, *13*, 31321.

[161] M. Muccini, S. Toffanin, *Organic Light-Emitting Transistors: Towards the Next Generation Display*, Wiley, New Jersey, **2016**.

[162] M. Muccini, S. Toffanin, *Org. Light. Transistors Towar. Next Gener. Disp. Technol.* **2016**, 1.

[163] M. Muccini, *Nat. Mater. 2006 58* **2006**, *5*, 605.

[164] R. Capelli, S. Toffanin, G. Generali, H. Usta, A. Facchetti, M. Muccini, *Nat. Mater.* **2010**, *9*, 496.

[165] W. Stampor, J. Kalinowski, P. Di Marco, V. Fattori, *Appl. Phys. Lett.* **1998**, *70*,

1935.

[166] J. Kalinowski, J. Męyk, F. Meinardi, R. Tubino, M. Cocchi, D. Virgili, *J. Chem. Phys.* **2008**, *128*, DOI 10.1063/1.2841458.

[167] V. Gulbinas, R. Karpicz, I. Muzikante, L. Valkunas, *Thin Solid Films* **2010**, *518*, 3299.

[168] N. Pfeffer, D. Neher, M. Remmers, C. Poga, M. Hopmeier, R. Mahrt, *Chem. Phys.* **1998**, *227*, 167.

[169] G. Horowitz, *J. Mater. Res.* **2004**, *19*, 1946.

[170] J. Zaumseil, C. L. Donley, J. S. Kim, R. H. Friend, H. Sirringhaus, *Adv. Mater.* **2006**, *18*, 2708.

[171] H. Yamamoto, T. Oyamada, H. Sasabe, C. Adachi, *Appl. Phys. Lett.* **2004**, *84*, 1401.

[172] M. A. Baldo, R. J. Holmes, S. R. Forrest, *Phys. Rev. B* **2002**, *66*, 035321.

[173] E. J. W. List, C. H. Kim, A. K. Naik, U. Scherf, G. Leising, W. Graupner, J. Shinar, *Phys. Rev. B* **2001**, *64*, 155204.

[174] J. Staudigel, M. Stößel, F. Steuber, J. Simmerer, *J. Appl. Phys.* **1999**, *86*, 3895.

[175] T. Sakanoue, M. Yahiro, C. Adachi, J. H. Burroughes, Y. Oku, N. Shimoji, T. Takahashi, A. Toshimitsu, *Appl. Phys. Lett.* **2008**, *92*, 053505.

[176] M. Ullah, R. Wawrzinek, R. C. R. Nagiri, S. C. Lo, E. B. Namdas, *Adv. Opt. Mater.* **2017**, *5*, DOI 10.1002/adom.201600973.

[177] B. B. Y. Hsu, C. Duan, E. B. Namdas, A. Gutacker, J. D. Yuen, F. Huang, Y. Cao, G. C. Bazan, I. D. W. Samuel, A. J. Heeger, *Adv. Mater.* **2012**, *24*, 1171.

[178] J. H. Lee, T. H. Ke, J. Genoe, P. Heremans, C. Rolin, *Adv. Electron. Mater.* **2019**, *5*, DOI 10.1002/aelm.201800437.

[179] T. Zhu, M. N. Chong, *Nano Energy* **2015**, *12*, 347.

[180] C. H. Lin, C. W. Liu, *Sensors 2010, Vol. 10, Pages 8797-8826* **2010**, *10*, 8797.

[181] V. Coropceanu, J. Cornil, D. A. da Silva Filho, Y. Olivier, R. Silbey, J. L. Brédas, *Chem. Rev.* **2007**, *107*, 926.

[182] A. Kahn, *Mater. Horizons* **2015**, *3*, 7.

[183] D. J. Frank, R. H. Dennard, E. Nowak, P. M. Solomon, Y. Taur, H. S. P. Wong, *Proc. IEEE* **2001**, *89*, 259.

[184] G. S. Tulevski, C. Nuckolls, A. Afzali, T. O. Graham, C. R. Kagan, *Appl. Phys. Lett.* **2006**, *89*, 183101.

[185] J. N. Haddock, X. Zhang, S. Zheng, Q. Zhang, S. R. Marder, B. Kippelen, *Org.*

Electron. **2006**, *7*, 45.

[186] M. Pope, H. P. Kallmann, P. Magnante, *J. Chem. Phys.* **2004**, *38*, 2042.

[187] W. Helfrich, W. G. Schneider, *Phys. Rev. Lett.* **1965**, *14*, 229.

[188] A. Sacco, *Fondamenti Di Chimica*, **1996**.

[189] V. Balzani, P. Ceroni, A. Juris, *Photochemistry and Photophysics: Concepts, Research, Applications*, **2014**.

[190] R. H. Friend, R. W. Gymer, A. B. Holmes, J. H. Burroughes, R. N. Marks, C. Taliani, D. D. C. Bradley, D. A. Dos Santos, J. L. Brédas, M. Lögdlund, W. R. Salaneck, *Nature* **1999**, *397*, 121.

[191] C. Wang, H. Dong, W. Hu, Y. Liu, D. Zhu, *Chem. Rev.* **2012**, *112*, 2208.

[192] A. Facchetti, *Mater. Today* **2007**, *10*, 28.

[193] E. F. Valeev, V. Coropceanu, D. A. Da Silva Filho, S. Salman, J. L. Brédas, *J. Am. Chem. Soc.* **2006**, *128*, 9882.

[194] J. L. Brédas, J. P. Calbert, D. A. Da Silva Filho, J. Cornil, *Proc. Natl. Acad. Sci. U. S. A.* **2002**, *99*, 5804.

[195] A. Dieckmann, H. Bässler, P. M. Borsenberger, *J. Chem. Phys.* **1998**, *99*, 8136.

[196] C. D. Dimitrakopoulos, S. Purushothaman, J. Kymissis, A. Callegari, J. M. Shaw, *Science* **1999**, *283*, 822.

[197] N. Karl, K.-H. Kraft, J. Marktanner, M. Münch, F. Schatz, R. Stehle, H.-M. Uhde, *J. Vac. Sci. Technol. A Vacuum, Surfaces, Film.* **1999**, *17*, 2318.

[198] F. Meinardi, M. Cerminara, A. Sassella, A. Borghesi, P. Spearman, G. Bongiovanni, A. Mura, R. Tubino, *Phys. Rev. Lett.* **2002**, *89*, 157403/1.

[199] S. R. Forrest, *Chem. Rev.* **1997**, *97*, 1793.

[200] E. Da Como, M. A. Loi, M. Murgia, R. Zamboni, M. Muccini, *J. Am. Chem. Soc.* **2006**, *128*, 4277.

[201] E. Lunedei, PhD Thesis, Stuttgart, **2003**.

[202] F. Todescato, R. Capelli, F. Dinelli, M. Murgia, N. Camaioni, M. Yang, R. Bozio, M. Muccini, *J. Phys. Chem. B* **2008**, *112*, 10130.

[203] W. H. Lee, J. H. Cho, K. Cho, *J. Mater. Chem.* **2010**, *20*, 2549.

[204] R. P. Ortiz, A. Facchetti, T. J. Marks, *Chem. Rev.* **2010**, *110*, 205.

[205] B. Wang, W. Huang, L. Chi, M. Al-Hashimi, T. J. Marks, A. Facchetti, *Chem. Rev.* **2018**, *118*, 5690.

[206] C. Soldano, R. D'Alpaos, G. Generali, *ACS Photonics* **2017**, *4*, 800.

[207] M. H. Yoon, C. Kim, A. Facchetti, T. J. Marks, *J. Am. Chem. Soc.* **2006**, *128*,

12851.

[208] J. Veres, S. Ogier, G. Lloyd, D. De Leeuw, *Chem. Mater.* **2004**, *16*, 4543.

[209] A. Facchetti, M. H. Yoon, T. J. Marks, *Adv. Mater.* **2005**, *17*, 1705.

[210] K. Zhou, H. Dong, H. li Zhang, W. Hu, *Phys. Chem. Chem. Phys.* **2014**, *16*, 22448.

[211] J. T. E. Quinn, J. Zhu, X. Li, J. Wang, Y. Li, *J. Mater. Chem. C* **2017**, *5*, 8654.

[212] J. L. Brédas, D. Beljonne, V. Coropceanu, J. Cornil, *Chem. Rev.* **2004**, *104*, 4971.

[213] X. Yang, G. Zhou, W. Y. Wong, *Chem. Soc. Rev.* **2015**, *44*, 8484.

[214] A. J. Huckaba, M. K. Nazeeruddin, *http://dx.doi.org/10.1080/02603594.2016.1207064* **2016**, *37*, 117.

[215] W. S. Jeon, T. J. Park, S. Y. Kim, R. Pode, J. Jang, J. H. Kwon, *Org. Electron.* **2009**, *10*, 240.

[216] Q. Wei, N. Fei, A. Islam, T. Lei, L. Hong, R. Peng, X. Fan, L. Chen, P. Gao, Z. Ge, *Adv. Opt. Mater.* **2018**, *6*, 1800512.

[217] J. Zaumseil, J. Zaumseil, *Adv. Funct. Mater.* **2020**, *30*, 1905269.

[218] C. Zhang, P. Chen, W. Hu, *Small* **2016**, *12*, 1252.

[219] C. F. Liu, X. Liu, W. Y. Lai, W. Huang, *Adv. Mater.* **2018**, *30*, 1802466.

[220] L. Bürgi, T. J. Richards, R. H. Friend, H. Sirringhaus, *J. Appl. Phys.* **2003**, *94*, 6129.

[221] M. A. Abkowitz, H. A. Mizes, J. S. Facci, *Appl. Phys. Lett.* **1998**, *66*, 1288.

[222] R. Schmechel, M. Ahles, H. Von Seggern, *J. Appl. Phys.* **2005**, *98*, 084511.

[223] P. Mei, M. Murgia, C. Taliani, E. Lunedei, M. Muccini, *J. Appl. Phys.* **2000**, *88*, 5158.

[224] C. L. Donley, J. Zaumseil, J. W. Andreasen, M. M. Nielsen, H. Sirringhaus, R. H. Friend, J. S. Kim, *J. Am. Chem. Soc.* **2005**, *127*, 12890.

[225] F. Dinelli, R. Capelli, M. A. Loi, M. Murgia, M. Muccini, A. Facchetti, T. J. Marks, *Adv. Mater.* **2006**, *18*, 1416.

[226] M. Zambianchi, E. Benvenuti, C. Bettini, C. Zanardi, R. Seeber, D. Gentili, M. Cavallini, M. Muccini, V. Biondo, C. Soldano, G. Generali, S. Toffanin, M. Melucci, *J. Mater. Chem. C* **2016**, *4*, 9411.

[227] M. Prosa, E. Benvenuti, M. Pasini, U. Giovanella, M. Bolognesi, L. Meazza, F. Galeotti, M. Muccini, S. Toffanin, *ACS Appl. Mater. Interfaces* **2018**, *10*, 25580.

[228] D. Gedefaw, M. Prosa, M. Bolognesi, M. Seri, M. R. Andersson, *Adv. Energy Mater.* **2017**, *7*, 1700575.

[229] D. Gedefaw, M. Tessarolo, M. Bolognesi, M. Prosa, R. Kroon, W. Zhuang, P. Henriksson, K. Bini, E. Wang, M. Muccini, M. Seri, M. R. Andersson, *Beilstein J. Org. Chem.* **2016**, *12*, 1629.

[230] Z. Li, X. Xu, W. Zhang, Z. Genene, W. Mammo, A. Yartsev, M. R. Andersson, R. A. J. Janssen, E. Wang, *J. Mater. Chem. A* **2017**, *5*, 11693.

[231] M. Seri, D. Gedefaw, M. Prosa, M. Tessarolo, M. Bolognesi, M. Muccini, M. R. Andersson, *J. Polym. Sci. Part A Polym. Chem.* **2017**, *55*, 234.

[232] A. Riaño, P. Mayorga Burrezo, M. J. Mancheño, A. Timalsina, J. Smith, A. Facchetti, T. J. Marks, J. T. López Navarrete, J. L. Segura, J. Casado, R. Ponce Ortiz, *J. Mater. Chem. C* **2014**, *2*, 6376.

[233] X. Chen, G. Zhang, H. Luo, Y. Li, Z. Liu, D. Zhang, *J. Mater. Chem. C* **2014**, *2*, 2869.

[234] S. Bonetti, M. Prosa, A. Pistone, L. Favaretto, A. Sagnella, I. Grisin, M. Zambianchi, S. Karges, A. Lorenzoni, T. Posati, R. Zamboni, N. Camaioni, F. Mercuri, M. Muccini, M. Melucci, V. Benfenati, *J. Mater. Chem. B* **2016**, *4*, 2921.

[235] M. Melucci, M. Durso, C. Bettini, M. Gazzano, L. Maini, S. Toffanin, S. Cavallini, M. Cavallini, D. Gentili, V. Biondo, G. Generali, F. Gallino, R. Capelli, M. Muccini, *Structure-Property Relationships in Multifunctional Thieno(Bis)Imide-Based Semiconductors with Different Sized and Shaped N-Alkyl Ends*, **2014**.

[236] F. Garnier, R. Hajlaoui, A. El Kassmi, G. Horowitz, L. Laigre, W. Porzio, M. Armanini, F. Provasoli, *Chem. Mater.* **1998**, *10*, 3334.

[237] H. E. Katz, A. J. Lovinger, J. G. Laquindanum, *Chem. Mater.* **1998**, *10*, 457.

[238] R. Capelli, F. Dinelli, S. Toffanin, F. Todescato, M. Murgia, M. Muccini, A. Facchetti, T. J. Marks, *J. Phys. Chem. C* **2008**, *112*, 12993.

[239] M. Durso, D. Gentili, C. Bettini, A. Zanelli, M. Cavallini, F. De Angelis, M. Grazia Lobello, V. Biondo, M. Muccini, R. Capelli, M. Melucci, *Chem. Commun.* **2013**, *49*, 4298.

[240] D. Fichou, *Structural Order in Conjugated Oligothiophenes and Its Implications on Opto-Electronic Devices*, **2000**.

[241] E. Benvenuti, D. Gentili, F. Chiarella, A. Portone, M. Barra, M. Cecchini, C. Cappuccino, M. Zambianchi, S. G. Lopez, T. Salzillo, E. Venuti, A. Cassinese, D. Pisignano, L. Persano, M. Cavallini, L. Maini, M. Melucci, M. Muccini, S.

Toffanin, *J. Mater. Chem. C* **2018**, *6*, 5601.

[242] M. Zambianchi, L. Favaretto, M. Durso, C. Bettini, A. Zanelli, I. Manet, M. Gazzano, L. Maini, D. Gentili, S. Toffanin, F. Gallino, M. Muccini, M. Cavallini, M. Melucci, *J. Mater. Chem. C* **2015**, *3*, 121.

[243] S. Oku, K. Takamiya, D. Adachi, S. Ishikawa, S. Nagamatsu, W. Takashima, S. Hayase, K. Kaneto, *Chem. Lett.* **2010**, *39*, 1315.

[244] L. Maini, F. Gallino, M. Zambianchi, M. Durso, M. Gazzano, K. Rubini, D. Gentili, I. Manet, M. Muccini, S. Toffanin, M. Cavallini, M. Melucci, *Chem. Commun.* **2015**, *51*, 2033.

[245] M. Prosa, S. Moschetto, E. Benvenuti, M. Zambianchi, M. Muccini, M. Melucci, S. Toffanin, *J. Mater. Chem. C* **2020**, *8*, 15048.

[246] M. Melucci, L. Favaretto, M. Zambianchi, M. Durso, M. Gazzano, A. Zanelli, M. Monari, M. G. Lobello, F. De Angelis, V. Biondo, G. Generali, S. Troisi, W. Koopman, S. Toffanin, R. Capelli, M. Muccini, *Molecular Tailoring of New Thieno(Bis)Imide-Based Semiconductors for Single Layer Ambipolar Light Emitting Transistors*, **2013**.

[247] C. Cappuccino, P. P. Mazzeo, T. Salzillo, E. Venuti, A. Giunchi, R. G. Della Valle, A. Brillante, C. Bettini, M. Melucci, L. Maini, *Phys. Chem. Chem. Phys.* **2018**, *20*, 3630.

[248] S. Moschetto, E. Benvenuti, H. Usta, R. Ozdemir, A. Facchetti, M. Muccini, M. Prosa, S. Toffanin, *Adv. Mater. Interfaces* **2022**, *9*, 1.

[249] D. Yuan, M. A. Awais, V. Sharapov, X. Liu, A. Neshchadin, W. Chen, M. Bera, L. Yu, *Chem. Sci.* **2020**, *11*, 11315.

[250] M. Ullah, K. Tandy, S. D. Yambem, M. Aljada, P. L. Burn, P. Meredith, E. B. Namdas, *Adv. Mater.* **2013**, *25*, 6213.

[251] Y. Yuan, G. Giri, A. L. Ayzner, A. P. Zoombelt, S. C. B. Mannsfeld, J. Chen, D. Nordlund, M. F. Toney, J. Huang, Z. Bao, *Nat. Commun.* **2014**, *5*, DOI 10.1038/NCOMMS4005.

[252] C. Luo, A. K. K. Kyaw, L. A. Perez, S. Patel, M. Wang, B. Grimm, G. C. Bazan, E. J. Kramer, A. J. Heeger, *Nano Lett.* **2014**, *14*, 2764.

[253] C. R. Newman, C. D. Frisbie, D. A. Da Silva Filho, J. L. Brédas, P. C. Ewbank, K. R. Mann, *Chem. Mater.* **2004**, *16*, 4436.

[254] X. Gao, Y. Hu, *J. Mater. Chem. C* **2014**, *2*, 3099.

[255] X. Zhao, X. Zhan, *Chem. Soc. Rev.* **2011**, *40*, 3728.

[256] Y. Zhao, Y. Guo, Y. Liu, *Adv. Mater.* **2013**, *25*, 5372.

[257] J. E. Anthony, A. Facchetti, M. Heeney, S. R. Marder, X. Zhan, *Adv. Mater.* **2010**, *22*, 3876.

[258] J. Zaumseil, H. Sirringhaus, *Chem. Rev.* **2007**, *107*, 1296.

[259] L. Song, Y. Hu, D. Li, H. Chen, X. Liu, *J. Phys. Chem. C* **2015**, *119*, 20237.

[260] C. Borek, K. Hanson, P. I. Djurovich, M. E. Thompson, K. Aznavour, R. Bau, Y. Sun, S. R. Forrest, J. Brooks, L. Michalski, J. Brown, *Angew. Chemie - Int. Ed.* **2007**, *46*, 1109.

[261] M. Natali, M. Prosa, A. Longo, M. Brucale, F. Mercuri, M. Buonomo, N. Lago, E. Benvenuti, F. Prescimone, C. Bettini, A. Cester, M. Melucci, M. Muccini, S. Toffanin, *On the Nature of Charge-Injecting Contacts in Organic Field-Effect Transistors*, American Chemical Society (ACS), **2020**.

[262] H. Usta, C. Risko, Z. Wang, H. Huang, M. K. Deliomeroglu, A. Zhukhovitskiy, A. Facchetti, T. J. Marks, *J. Am. Chem. Soc.* **2009**, *131*, 5586.

[263] G. Generali, C. Soldano, A. Facchetti, M. Muccini, *Dig. Tech. Pap. - SID Int. Symp.* **2016**, *47*, 1779.

[264] G. Generali, F. Dinelli, R. Capelli, S. Toffanin, M. Muccini, *J. Phys. D. Appl. Phys.* **2011**, *44*, DOI 10.1088/0022-3727/44/22/224018.

[265] V. Ahmad, J. Sobus, F. Bencheikh, M. Mamada, C. Adachi, S. C. Lo, E. B. Namdas, *Adv. Opt. Mater.* **2020**, *8*, 2000554.

[266] J. G. Jang, H. J. Ji, H. S. Kim, J. C. Jeong, *Curr. Appl. Phys.* **2011**, *11*, S251.

[267] G. Paasch, T. Lindner, C. Rost-Bietsch, S. Karg, W. Riess, S. Scheinert, *J. Appl. Phys.* **2005**, *98*, DOI 10.1063/1.2085314.

[268] J. Voas, N. Kshetri, J. F. Defranco, *IT Prof.* **2021**, *23*, 78.

[269] M. Cloupeau, B. Prunet-Foch, *J. Aerosol Sci.* **1994**, *25*, 1021.

[270] R. G. Larson, T. J. Rehg, *Liq. Film Coat.* **1997**, 709.

[271] G. Generali, F. Dinelli, R. Capelli, S. Toffanin, F. Di Maria, M. Gazzano, G. Barbarella, M. Muccini, *J. Phys. Chem. C* **2011**, *115*, 23164.

[272] I. H. Campbell, D. L. Smith, *Solid State Phys. - Adv. Res. Appl.* **2001**, *55*, 1.

[273] A. Troisi, G. Orlandi, *J. Phys. Chem. B* **2005**, *109*, 1849.

[274] A. Troisi, *Chem. Soc. Rev* **2011**, *40*, 2347.

[275] N. W. Ashcroft, D. N. Mermin, *Solid State Physics*, Cengage Learning, **1976**.

[276] P. Drude, *Ann. Phys.* **1900**, *306*, 566.

[277] R. A. Marcus, *https://doi.org/10.1146/annurev.pc.15.100164.001103* **2003**, *15*,

155.

[278] S. Fratini, S. Ciuchi, *Phys. Rev. Lett.* **2009**, *103*, 266601.

[279] D. V. Lang, X. Chi, T. Siegrist, A. M. Sergent, A. P. Ramirez, *Phys. Rev. Lett.* **2004**, *93*, 086802.

[280] R. A. Street, J. E. Northrup, A. Salleo, *Phys. Rev. B - Condens. Matter Mater. Phys.* **2005**, *71*, 165202.

[281] K. Puntambekar, J. Dong, G. Haugstad, C. Daniel Frisbie, **2006**, DOI 10.1002/adfm.200500816.